Geometrical Multidisciplinary Design Analysis and Optimisation for Airborne Wind Energy Systems

Master of Science Thesis

Bart Johannes Kroese

Delft University of Technology

This page was intentionally left blank.

Geometrical Multidisciplinary Design Analysis and Optimisation for Airborne Wind Energy Systems

by

Bart Johannes Kroese

to obtain the degree of Master of Science

at the Delft University of Technology,

to be defended publicly on Friday, March 27th, 2026, at 14:00.

Student number:	4862279	
Project duration:	May 6, 2025 – March 27, 2026	
Thesis committee:	Dr. Ir. M.F.M. Hoogreef,	TU Delft, Committee chair
	Dr. Ir. F. de Prenter,	TU Delft, Independent examiner
	Dr.-Ing. R. Schmehl,	TU Delft, supervisor
	Ir. J.A.W. Poland,	TU Delft, supervisor
	Dr. C. Vergara,	Kitepower, supervisor
Faculty:	Faculty of Aerospace Engineering, Delft	

TU Delft

KITEPOWER

Preface

Kites have fascinated me for as long as I can remember, in fact, a long time before I knew about airborne wind energy (AWE). It began with a simple construction of two sticks, thin paper and a rope, combined with a childlike imagination and drive. Most people, like me, have at least once in their lives flown a kite, a thrilling experience that makes you feel like a pilot, filled with a sense of freedom, exhilaration, and wanderlust. Or so, at least, it felt for me. This is what truly fascinates me about the concept: it speaks to my imagination. Without imagination, the world would be a lot worse place.

I would like to start by thanking Dr.-Ing. Roland Schmehl, who introduced the concept of AWE to me in an elective course at the TU Delft as part of my master's programme. Next to the introduction to the concept, I also want to thank Roland for the great supervision and feedback on this thesis, and for the collaboration with Kitepower, which served as the host of this thesis.

Secondly, I want to thank all members of the AWE research group at TU Delft for inspiring me and providing valuable feedback. In particular, I want to thank Jelle Poland and Oriol Cayon for the great brainstorming sessions and contagious curiosity.

During my time at Kitepower, I have been inspired by many people there, who share a passion for this very niche technology and, more importantly, believe in it. Even more inspiring, as a startup, it can only come as far as its believers are willing to go. In particular, I want to thank Claudio Vergara for taking responsibility for supervising and providing many interesting insights. Also, I want to thank the Kitepower software team for providing guidance and teaching many valuable lessons. A special thanks also goes out to Tom Lollies, who inspires me with an incredible background in kite design. And, of course, I want to thank the other interns at Kitepower, Andrea, Daan, Daan, Orianne, Pim, and Theophile, who made my internship insightful and enjoyable in many other ways.

Figure 1: 6-year-old me, flying a kite on the beach of Schiermonnikoog.

I also want to thank my family: my father for fostering my passion for flying and engineering, my mother for being a source of unconditional help and support, and my sister for being a great listening ear. Not to forget, my dog, Djieuwke, who unfortunately passed away last May, but has been a great source of comfort during my whole academic journey.

Lastly, I want to thank my friends, who have supported me in many other ways and made me a better person. I consider myself lucky to be surrounded by so many wonderful people who inspire, motivate, and push me, and care for me with sincerity. These people helped me to become the person I am today.

Bart Johannes Kroese
Delft, March 2026

Abstract

The global transition to sustainable energy sources has accelerated the development of renewable energy technologies, with airborne wind energy (AWE) emerging as a promising innovation within the wind energy sector. AWE harnesses high-altitude winds using tethered kites, offering the potential to generate electricity with significantly lower material requirements compared to conventional wind turbines. Among AWE systems, leading-edge inflatable (LEI) kites operating in crosswind patterns have demonstrated substantial energy production capabilities. However, the design of such kites is inherently multidisciplinary, involving aerodynamic performance, structural behaviour, and operational constraints. Current design iterations rely heavily on expert knowledge and in-house experimental testing, resulting in slow, costly, and resource-intensive processes.

This thesis presents the development and assessment of a computational framework based on multidisciplinary analysis and optimisation (MDAO) for the geometric design of LEI kites, with a specific focus on the ground-generation crosswind system developed by Kitepower B.V. The framework enables systematic optimisation of the kite's wing geometry by parametrising its shape with five decoupled parameters, including aspect ratio, arc shape coefficients, and camber scaling. Aerodynamic and structural performance are evaluated using a combination of a regression model, vortex step method, and particle-based structural model, while energy production is assessed through flight trajectory and dynamic simulation models. A high-fidelity conceptual toolchain was developed, and a simplified framework was implemented without structural modelling and using a low-fidelity power model. The implemented framework was tested to compare the annual energy production (AEP) of kite geometric designs.

The TU Delft V3 kite was used to verify the implemented framework, which resulted in a 94% improvement in predicted AEP. Sensitivity analyses reveal that operational assumptions, such as fixed sideslip angles in turning flight, and environmental conditions, such as varying wind speeds, influence the optimal kite geometry and resulting energy output. The results highlight the framework's ability to capture critical design trade-offs and adapt to different operating conditions. The framework, however, was tested only in a highly simplified modelling environment, making the obtained results unsuitable for quantitative interpretation. Instead, the observed trends provide a qualitative indication of the potential of MDAO for AWE kite design, supporting further investigation using higher-fidelity implementations. Overall, this research demonstrates the potential of MDAO as a time- and cost-efficient approach for early-stage kite wing design in AWE applications.

Contents

Preface i

Abstract ii

Nomenclature ix

1 Introduction 1

2 Literature review 3
- 2.1 Airborne wind energy . . . 3
  - 2.1.1 The Kitepower system: ground-gen crosswind . . . 5
  - 2.1.2 AWES performance indicators . . . 7
- 2.2 Key geometric kite design parameters . . . 8
  - 2.2.1 Airfoil design parameters . . . 8
  - 2.2.2 Wing design parameters . . . 9
- 2.3 Kite analysis and modelling tools . . . 9
  - 2.3.1 Aerodynamic and structural modelling tools for kite wings . . . 10
  - 2.3.2 AWES simulation and performance estimation tools . . . 10
- 2.4 Multidisciplinary design analysis and optimisation . . . 11
  - 2.4.1 System architectures . . . 12
  - 2.4.2 Extended design structure matrix . . . 13
  - 2.4.3 Optimisation algorithms . . . 15
  - 2.4.4 Demonstration of MDO application on wing design. . . . 15
- 2.5 Discussion and research objectives . . . 16

3 Methodology 18
- 3.1 Research approach . . . 18
  - 3.1.1 Design-oriented and model-based research . . . 18
  - 3.1.2 Framework and workflow . . . 19
- 3.2 The need for a universal kite ontology . . . 19
- 3.3 Reference kite definition and parametrisation . . . 20
  - 3.3.1 The TU Delft V3 kite . . . 20
  - 3.3.2 Parametrisation of a LEI kite wing . . . 21
- 3.4 Detailed description of selected simulation tools . . . 24
  - 3.4.1 SurfPlan™ and SurfPlanAdapter . . . 24
  - 3.4.2 ASKITE . . . 25
  - 3.4.3 Luchsinger's model . . . 27
  - 3.4.4 AWETrim . . . 28
  - 3.4.5 Dynamic three-dimensional system model . . . 29
- 3.5 Objective function . . . 30

4 Kite parametrisation and reshaping 32
- 4.1 Aspect ratio parametrisation and scaling . . . 32
- 4.2 Arc parametrisation and reshaping . . . 33
- 4.3 Airfoil parametrisation and reshaping . . . 34

4.3.1 Camber scaling . . . 35
4.3.2 Leading-edge diameter scaling . . . 36
4.4 Geometric reshaping example . . . 36

5 Simulation framework **40**
5.1 Conceptual design framework . . . 40
5.1.1 Intended discipline coupling . . . 40
5.1.2 Extensions for conceptual framework . . . 42
5.2 Implemented toolchain . . . 42
5.3 Operational conditions . . . 45
5.3.1 Trim state computation . . . 45
5.3.2 Turning radius . . . 46
5.3.3 Average elevation and azimuth angle . . . 50
5.4 Optimisation algorithms . . . 52
5.4.1 Hooke and Jeeves pattern search . . . 53
5.4.2 CMA-ES optimisation . . . 53
5.4.3 PySwarms particle swarm optimisation . . . 53
5.4.4 Algorithm selection and integration . . . 53

6 Results **55**
6.1 Geometric planform reshaping . . . 55
6.2 Aerodynamic analysis . . . 58
6.3 Operational analysis . . . 59
6.4 Performance of the TU Delft V3 kite . . . 61
6.5 Design space exploration . . . 63
6.6 Optimisation of the TU Delft V3 Kite . . . 65
6.7 Sensitivity analysis . . . 67
6.7.1 Fixed sideslip angle β . . . 68
6.7.2 Environmental conditions . . . 69

7 Conclusion **72**

8 Recommendations **74**
8.1 Extension of the geometric parametrisation . . . 74
8.2 Validation of operational constraints . . . 74
8.3 Structural design integration . . . 74
8.4 Useful extension of the framework . . . 75
8.5 Experimental validation . . . 75

References **76**

A Kite Reshaping Work Flow **80**

B Conceptual Toolchain XDSM **81**

C Luchsinger Model Simulation Settings **83**

D Optimisation Dashboard **84**

List of Figures

1 6-year-old me, flying a kite on the beach of Schiermonnikoog. i

2.1 AWE industry classification overview [46]. 4
2.2 Three most common AWES concepts: ground-gen cross-wind (a), ground-gen rotary (b), and fly-gen (c) [1]. 5
2.3 AWES configuration overview [54]. 6
2.4 Example of a pumping cycle flight trajectory with indicated flight phases [44]. . 7
2.5 General power curve for an AWES [46]. 8
2.6 LEI kite airfoil parametrisation by Masure [34]. 9
2.7 Arc width and height comparison. 9
2.8 Influence of MDAO on the engineering design process [33]. 12
2.9 Influence of interacting engineering disciplines on aircraft design; originally from [36], inspired by [43]. 13
2.10 Example of an MDF architecture represented using XDSM [24]. The blocks represent disciplines and other steps in the execution of the optimisation framework, and the black line indicates the execution order. 14
2.11 Data flow between execution blocks in an XDSM representation; optimisation (a), MDA (b), discipline (c), function (d). 14
2.12 Two optimised wing shapes found in wing design optimisation utilising MDO with random starting geometries [7]. 16

3.1 Front view (a) and side view (b) of the TU Delft V3 kite [38]. 20
3.2 Axes system orientation of the TU Delft V3 kite computational geometry [46]. . 21
3.3 TU Delft V3 kite structure with projected quarter-chord arc. 23
3.4 Front view of the quarter-chord arc of the TU Delft V3 kite with fitted Bézier curve and corresponding control points. 23
3.5 Replacement of a finite wing section with a horseshoe vortex [2]. 26
3.6 VSM results for the TU Delft V3 kite, including aerodynamic force vectors and wake geometry. 26
3.7 Particle-based structural representation of the TU Delft V3 kite [42]. 27
3.8 Side view of a measured kite flight path (blue) and the idealised flight path used in Luchsinger's model (dashed) [46]. 28
3.9 Schematic flight path options for QSM: radially expanding (a) and parallel (b). . 29
3.10 The four-point kite model defined by points A, B, C and D. 29
3.11 Energy log used for AEP calculation. The hourly nominal wind speed is given (orange), to which the instantaneous power production is determined (blue). . 31

4.1 Example of a segmented wing planform for dimensional reshaping. 33
4.2 Kite arc-shape parametrisation. 34
4.3 Effects on the span-normalised projected arc shape with scaled parameters Γ (left), cd (middle), and ab (right). 34
4.4 Camber height parameter κ along the flattened spanwise position of the TU Delft V3 kite. 35

4.5 Airfoil geometry with scaled camber parameter κ ($x_\kappa = 0.8$ (blue), $x_\kappa = 1.2$ (red), $x_\kappa = 1.0$ (black), with fixed profile parameters: $t = 0.08$, $\eta = 0.2$, $\delta = 0°$, $\lambda = 0.2$, $\phi = 0.65$. . . . 36
4.6 Scaling step 1: Definition of the reference kite geometry and baseline planform used for scaling. . . . 37
4.7 Scaling step 2: Identification of leading- and trailing-edge, and corresponding quarter-chord arc of the reference geometry. . . . 37
4.8 Scaling step 3: Construction of the scaled quarter-chord arc with updated curvature and span, while enforcing the reference tip z-coordinate. Additional effects of the arc-shape parametrisation are applied at this stage. . . . 37
4.9 Scaling step 4: Placement of the leading- and trailing-edges along the updated quarter-chord arc using the scaled chord lengths. . . . 38
4.10 Scaling step 5: Placement of the airfoil sections at the updated locations, with the camber parameter κ scaled accordingly. . . . 38
4.11 Effect of AR scaling on the bridle setup: nodes are translated from the tip z-coordinate (marked with the "+"). . . . 39

5.1 Flowchart of the conceptual GeKO framework. P1: [34], P2: [41], P3: [42], P4: [10], P5: [17] . . . 41
5.2 Flowchart of the implemented GeKO framework. P1: [34], P2: [41], P3: [46] . . . 43
5.3 XDSM of the implemented GeKO Toolchain. Blocks represent simulations, modelling, and objective disciplines, and the black line indicates the execution order. . . . 44
5.4 Trim angle computation logic: elongated depower line (left), shortened depower line (right), and trim state (middle). . . . 46
5.5 Side force reaction during sideslip. . . . 48
5.6 Moment of inertia approximation and induced moment. . . . 48
5.7 Ideal turn flight path. . . . 49
5.8 Ideal crosswind flight (horizontal) compared to a more realistic elevated flight. 51
5.9 Ground clearance at minimum tether length. . . . 52
5.10 Figure-eight flight trajectory used for average azimuth angle calculations. . . . 52

6.1 Kite isometric geometry with $AR = 3.0$ (blue), $AR = 15.0$ (red), and $AR = 5.0$ (black); fixed parameters $ab = 0.57$, $cd = 0.63$, $\Gamma = 0.60$. . . . 55
6.2 Kite isometric geometry with $ab = 0.0$ (blue), $ab = 1.0$ (red), and $ab = 0.57$ (black); fixed parameters $AR = 5.08$, $cd = 0.63$, $\Gamma = 0.60$. . . . 56
6.3 Kite isometric geometry with $cd = 0.0$ (blue), $cd = 1.0$ (red), and $cd = 0.63$ (black); fixed parameters $AR = 5.08$, $ab = 0.57$, $\Gamma = 0.60$. . . . 56
6.4 Kite isometric geometry with $\Gamma = 0.0$ (blue), $\Gamma = \frac{\pi}{3}$ (red), $\Gamma = 0.60$ (black); fixed parameters $AR = 5.08$, $ab = 0.57$, $cd = 0.63$. . . . 57
6.5 Projected area at variable ab. . . . 57
6.6 Projected area at variable cd. . . . 57
6.7 Projected area at variable AR. . . . 58
6.8 Projected area at variable Γ. . . . 58
6.9 Aerodynamic coefficients at variable ab; fixed parameters $AR = 5.0$, $cd = 0.6$, $\Gamma = 0.6$, $x_\kappa = 1.0$. . . . 58
6.10 Aerodynamic coefficients at variable cd; fixed parameters $AR = 5.0$, $ab = 0.6$, $\Gamma = 0.6$, $x_\kappa = 1.0$. . . . 58
6.11 Aerodynamic coefficients at variable AR; fixed parameters $ab = 0.6$, $cd = 0.6$, $\Gamma = 0.6$, $x_\kappa = 1.0$. . . . 59

6.12 Aerodynamic coefficients at variable Γ; fixed parameters $AR = 5.0$, $ab = 0.6$, $cd = 0.6$, $x_\kappa = 1.0$. 59
6.13 Aerodynamic coefficients at variable x_κ; fixed parameters $AR = 5.0$, $ab = 0.6$, $cd = 0.6$, $\Gamma = 0.6$. 59
6.14 The effect of the AR on the turning radius and operation angles; fixed parameters $ab = 5.0$, $cd = 0.6$, $\Gamma = 0.6$, $x_\kappa = 1.0$. 60
6.15 Average elevation and azimuth angle variation at variable ab; fixed parameters $AR = 5.0$, $cd = 0.6$, $\Gamma = 0.6$, $x_\kappa = 1.0$. 60
6.16 Average elevation and azimuth angle variation at variable cd; fixed parameters $AR = 5.0$, $ab = 0.6$, $\Gamma = 0.6$, $x_\kappa = 1.0$. 60
6.17 Average elevation and azimuth angle variation at variable AR; fixed parameters $ab = 0.6$, $cd = 0.6$, $\Gamma = 0.6$, $x_\kappa = 1.0$. 61
6.18 Average elevation and azimuth angle variation at variable Γ; fixed parameters $AR = 5.0$, $ab = 0.6$, $cd = 0.6$, $x_\kappa = 1.0$. 61
6.19 Smallest (blue) and largest (red) 8-figure flight paths within the feasible design space, at $\theta_{\text{av,min}}$ and $\phi_{\text{av,min}}$, and average $\theta_{\text{av,max}}$ and $\phi_{\text{av,max}}$ respectively. 61
6.20 Power curve of the TU Delft V3 kite. 62
6.21 Reeling factors and elevation angles of the TU Delft V3 kite. 62
6.22 AEP for varying AR, ab, and x_κ; fixed parameters $cd = 0.6$, $\Gamma = 0.6$. 63
6.23 AEP for varying AR, cd, and x_κ; fixed parameters $ab = 0.6$, $\Gamma = 0.6$. 64
6.24 AEP for varying AR, Γ, and x_κ; fixed parameters $ab = 0.6$, $cd = 0.6$. 64
6.25 AEP for varying arc-shape parameters ab, cd, and Γ; fixed parameters $AR = 5.0$, $x_\kappa = 1.0$. 65
6.26 Optimised kite geometry compared to TU Delft V3; $AR_{opt} = 17.63$, $ab_{opt} = 1.0$, $cd_{opt} = 0.2$, $\Gamma_{opt} = 0.88$, $x_{\kappa,opt} = 1.2$. 66
6.27 Fixed sideslip angle sensitivity trends to GeKO performance; design vector (left) and AEP (right). Normalisation was done using parameter bounds in Table 6.3. 68
6.28 AEP comparison between kites optimised for different wind speeds. 70

A.1 Flowchart of kite parametrisation and scaling. 80

D.1 Optimisation dashboard for TU Delft V3 kite. 84

List of Tables

3.1 Airfoil shape parameter ranges by Masure [34]. 25

5.1 Bridle line lengths of the TU Delft V3 Kite for different depower settings. 46

6.1 Design vector bounds for design space exploration. 63
6.2 Expected optimised design vector. 65
6.3 Design vector bounds for GeKO optimisation. 66
6.4 Simulation settings for the Hooke and Jeeves Pattern Search Algorithm. 66
6.5 Optimised design vector comparison to the reference TU Delft V3 kite. 66
6.6 Fixed sideslip angle sensitivity values to GeKO performance. 68
6.7 Design vector for different wind speed scaling factors. 70
6.8 AEP for optimised kite geometries simulated at the design and 1.0 wind scaling factor. 71

C.1 Simulation input parameters for environment, tether, and operational variables. 83

Nomenclature

Abbreviations

Abbreviation	Definition
AAO	All at once
AEP	Annual energy production
AR	Aspect ratio
AVL	Athena vortex lattice
AWE	Airborne wind energy
AWES	Airborne wind energy system
CAD	Computed aided design
CFD	Computation fluid dynamics
CMA-ES	Covariance matrix adaptation evolution strategy
FDS	Full dynamic simulation
FSM	Finite state machine
GeKO	Geometrical kite optimisation
GS	Ground station
IDF	Individual discipline feasible
KCU	Kite control unit
LE	Leading-edge
LEI	Leading-edge inflatable
LLM	Lifting line method
MDA	Multidisciplinary analysis
MDO	Multidisciplinary optimisation
MDAO	Multidisciplinary design analysis and optimisation
MDF	Multidisciplinary feasible
PSO	Particle swarm optimisation
QSM	Quasi-steady model
RQ	Research question
SAND	Simultaneous analysis and design
VLM	Vortex lattice method
XDSM	Extended design structure matrix

Symbols

Symbol	Definition	Unit
ab	Horizontal arc parametrisation distance	–
b	Wing span	m
c	Chord length	m
C_d	Airfoil drag coefficient	–
C_D	Wing drag coefficient	–
C_l	Airfoil lift coefficient	–
C_L	Wing lift coefficient	–
C_s	Wing side force coefficient	–
c_w	Wind scaling factor	–
$c_{w_{design}}$	Wind scaling factor used in design optimisation	–
cd	Vertical arc parametrisation distance	–
D	Drag force	N
$e_{y,k}$	Spanwise unit vector in the kite reference frame	–
f	Reeling factor	–
$F_{a,s}$	Aerodynamic side force	N
g	Gravitational acceleration	$\mathrm{m\,s^{-2}}$
GC	Ground clearance	m
I_{zz}	Moment of inertia about the z-axis	$\mathrm{kg\,m^2}$
L	Lift force	N
L_t	Tether length	m
M_{zz}	Moment about the z-axis	N m
m_k	Kite mass	kg
S_s	Side projected wing area	$\mathrm{m^2}$
t	Chord-normalised leading-edge tube diameter	-
$\mathcal{T}$	Torque	N m
TR	Kite turning radius	m
u_d	Depower setting	%
$v_{k,\tau}$	Tangential component of kite velocity	$\mathrm{m\,s^{-1}}$
v_t	Tether velocity	$\mathrm{m\,s^{-1}}$
v_w	Wind velocity	$\mathrm{m\,s^{-1}}$
x_κ	Camber scaling factor	–

Symbol	Definition	Unit
α	Angle of attack	$^\circ$
β	Angle of sideslip	$^\circ$
χ	Kite course angle	$^\circ$
Γ	Anhedral angle	$^\circ$
κ	Airfoil camber parametrisation factor	–
λ	Velocity ratio	–
ϕ	Azimuth angle	$^\circ$
ρ	Air density	$\mathrm{kg\,m^{-3}}$
θ	Elevation angle (measured from vertical reference frame)	$^\circ$
θ_{ground}	Elevation angle (measured from ground)	$^\circ$

Subscript	Definition
f	Flattened
i	Segment index
in	During reel-in
out	During reel-out
ref	Reference kite: in this thesis the TU Delft V3 kite

1 Introduction

The global urgency to transition to sustainable energy sources has never been greater, driving rapid development and innovation in the renewable energy sector [16]. The composition of the global energy mix shows a clear trend toward increased use of renewable energy sources, such as solar and wind. This and future growth include scale-ups and, of course, new innovations entering the industry. One promising innovation in the wind energy industry is airborne wind energy (AWE), which uses a kite to harvest wind energy and is built on the basis of three concepts:

- Solar and wind energy together are the only renewable energy sources that have the potential to meet humanity's energy needs [13].
- With the absence of the need for a high tower, replacing it with a tether, higher altitude winds can be leveraged for wind power [4].
- It can do this with only a fraction of the required materials to produce a system that is equivalent in power output to a wind turbine [56].

This thesis focuses on the implementation of Kitepower B.V., a spin-off company from the AWE research group at the Delft University of Technology, that uses a leading-edge inflatable (LEI) kite flying in cross-wind patterns to generate traction force on the tether. This tether is reeled out from a drum located on the ground, which is connected to a generator. Once fully reeled out, the kite can be reeled back in with lower energy consumption, resulting in a net energy production. Kitepower is in a development stage where kite requirements and, therefore, designs change rapidly. The current kite design iteration process is slow, expensive, and heavily reliant on expert knowledge, with new designs produced and tested through in-house experimental testing.

Kite design is inherently multidisciplinary, as it is governed by a wide range of physical phenomena, including aerodynamic and structural behaviour, as well as non-physical considerations such as cost. Multidisciplinary analysis and optimisation (MDAO) offers a structured approach to capturing the interactions among the disciplines governing kite design within a unified framework, thereby reducing the need for multiple isolated analyses and facilitating efficient optimisation of system performance under time and cost constraints.

As a start-up operating in the rapidly evolving AWE sector, Kitepower can benefit significantly from design methodologies that enable rapid and cost-effective iteration cycles. The objective of this thesis is therefore to develop a computational framework that reduces both the time

and cost associated with the kite design process, while systematically incorporating expert knowledge. To support this objective, the development of an integrated toolchain architecture that optimises the geometric shape of a kite by coupling the relevant disciplinary analyses within a MDAO framework is explored.

The rest of the thesis is structured as follows. Chapter 2 provides a literature review of the AWE industry and current kite design methods and tools, and outlines the research objective and corresponding research questions. Chapter 3 presents the methodology, and Chapter 4 and 5 provide detailed methodological explanations of reshaping and the simulation framework, respectively. Chapter 6 covers the results and discussions of this research, after which Chapter 7 concludes the work. Finally, Chapter 8 summarises the recommendations for future continuations of this work.

2

Literature review

This literature review examines the current state of the art in kite design methodologies for AWE and identifies knowledge gaps that stall future prospects of this technology. Since the technology has not been exploited in commercial applications, the design methods and tools have not been fully explored. Among the many tools available in engineering design, MDAO is considered a useful tool, and the extent of its implementation at AWE will be reviewed.

First, the concept of AWE is introduced in Section 2.1, followed by an analysis of the state-of-the-art design methods and objectives in kite design in Section 2.2. Known tools in this industry related to kite design are covered in Section 2.3, followed by an introduction to MDAO in Section 2.4. The findings of this literature review are then combined into a discussion and research objective in Section 2.5.

2.1. Airborne wind energy

The method of harvesting wind energy using a tethered airborne system is referred to as AWE [46]. Compared with conventional wind turbines, airborne wind energy systems (AWESs) offer several advantages. AWESs suspend a kite with a tether, which can be extended to altitudes significantly higher than those of the tallest wind turbines. Since wind speeds are generally higher at higher altitudes, the energy potential of the technology increases [6]. In addition, AWESs require substantially fewer resources than a conventional wind turbine with a comparable energy output [56].

From the original Laddermill concept [37], proposed by Wubbo Ockels (often regarded as the visionary founder of AWE [5]), several subsequent AWE concepts have emerged. The three most explored are fly-gen crosswind, ground-gen rotational and ground-gen crosswind applications. Active companies for each application concept are listed in Figure 2.1.

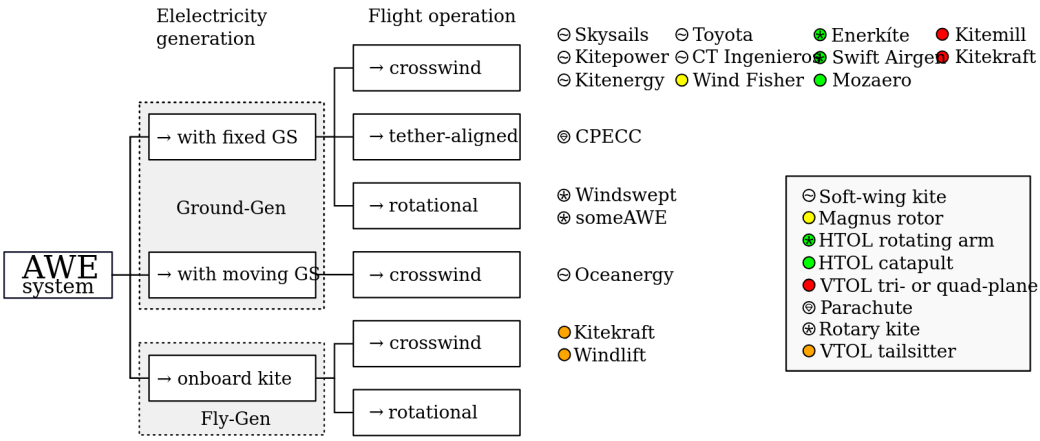

Figure 2.1: AWE industry classification overview [46].

The most mature and widely investigated AWE concept is the ground-generation crosswind configuration. In this approach, an airborne kite is connected via a tether to an electrical generator located on the ground, as illustrated in Figure 2.2a. Power is generated through a pumping cycle in which the kite is alternately reeled out and reeled in. During the reel-out phase, the kite operates at high crosswind speeds and generates a large tether force, whereas during the reel-in phase, it operates at reduced aerodynamic loading. The resulting difference in mechanical work between these phases yields a net positive energy output.

A second AWE concept that also employs a ground-based generator is the ground-generation rotary configuration. In this system, a primary kite supports and stabilises a rotating assembly of secondary kites arranged in a circular pattern. The aerodynamic forces acting on the rotating kites induce rotational motion in a cable structure, which is mechanically coupled to a ground-based generator, as shown in Figure 2.2b.

The third major AWE concept is based on airborne generation. Here, wind turbines mounted on the airborne platform directly convert aerodynamic power into electrical energy at altitude, where wind resources are generally stronger and more consistent. The generated electrical power is transmitted to the ground via a conductive tether. This system is schematically displayed in Figure 2.2c.

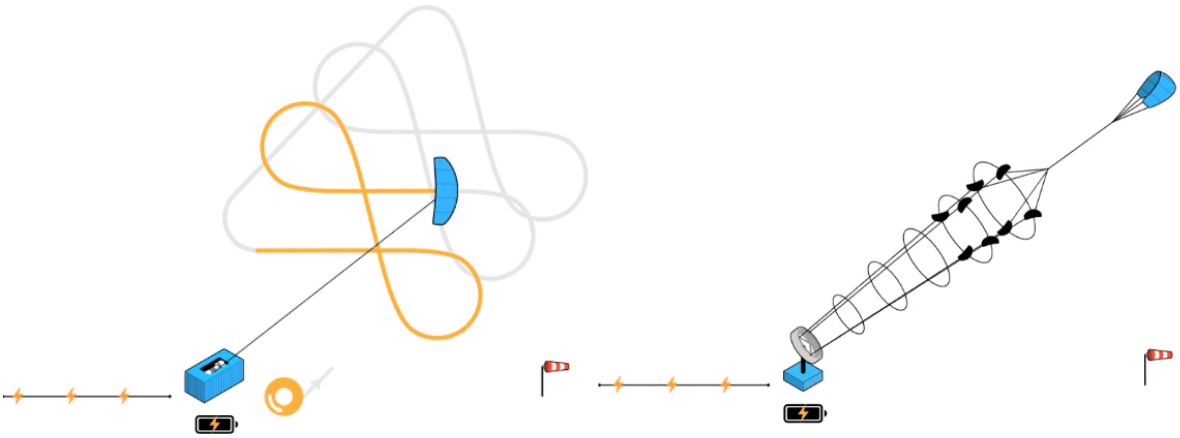

(a) Ground-gen cross wind.

(b) Ground-gen rotary.

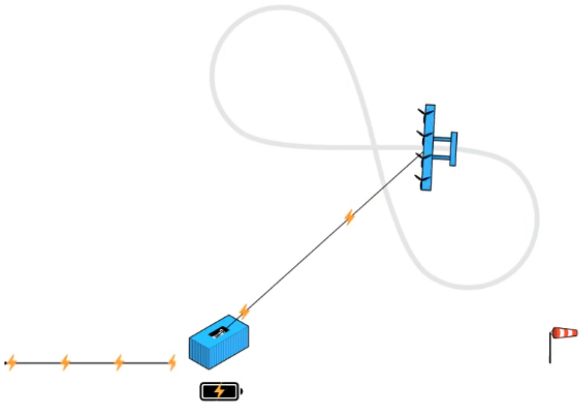

(c) Fly-gen.

Figure 2.2: Three most common AWES concepts: ground-gen cross-wind (a), ground-gen rotary (b), and fly-gen (c) [1].

A company focusing on developing a ground-gen crosswind AWES is Kitepower B.V., a spin-off of the AWE research group at Delft University of Technology, founded in January 2016. Kitepower's concept is described in more detail in Section 2.1.1. Next, the performance indicators used to evaluate AWESs are introduced in Section 2.1.2.

2.1.1. The Kitepower system: ground-gen crosswind

Kitepower is developing a commercial AWES that employs a LEI kite to harvest wind energy at high altitudes. The kite is connected via a bridle line system to an autonomous robotic unit, the kite control unit (KCU), which is responsible for flight control and actuation. The aerodynamic traction force generated by the kite is transmitted through a tether to a ground station (GS), where the tether is wound onto a drum mechanically coupled to an electrical generator. An overview of the system architecture and its main components is shown in Figure 2.3.

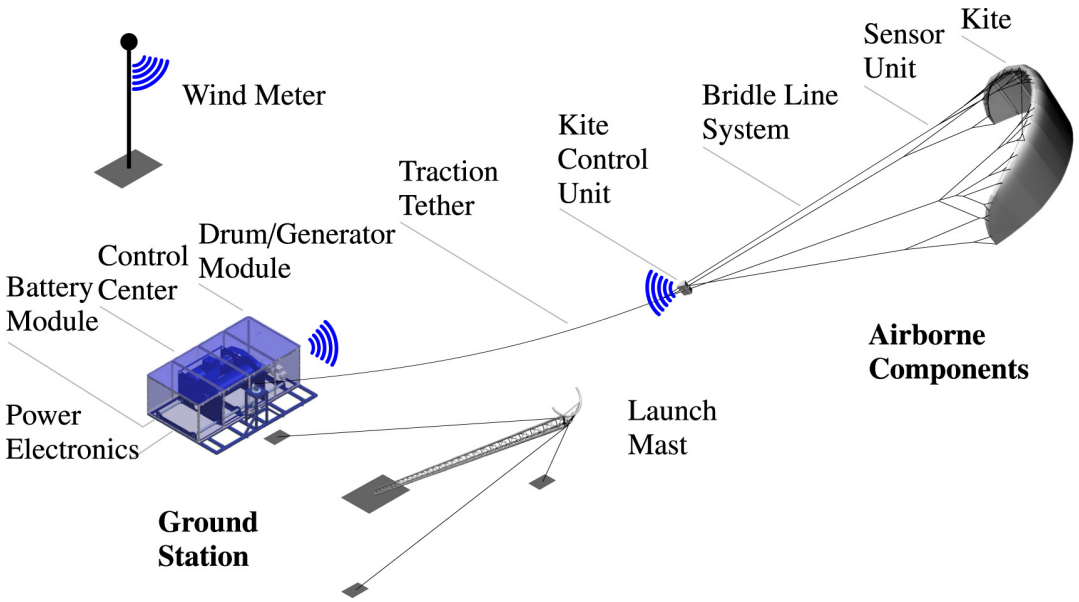

Figure 2.3: AWES configuration overview [54].

Electrical power generation is achieved through a cyclic pumping operation. During the reel-out phase, the kite is flown in cross-wind flight in order to maximise the apparent wind velocity experienced by the wing and, consequently, the generated lift force. This is typically realised by flying the kite along figure-eight or sometimes circular patterns. The resulting high tether tension unwinds the tether from the drum at the ground station, thereby driving the generator and converting mechanical energy into electrical energy.

Once the tether reaches its maximum length, the system enters the reel-in phase. During this stage, the kite is actively depowered by reducing its pitch angle and steering it toward the edge of the wind window, where aerodynamic forces are significantly reduced. As the tether is reeled back onto the drum, the system consumes energy; however, this consumption represents only a small portion of the energy produced during the reel-out phase. The repeated alternation between the powered reel-out phase and the depowered reel-in phase forms what is known as the pumping cycle, illustrated in Figure 2.4. The net electrical energy generated by the system is therefore determined by the balance between these two phases, making the pumping cycle a fundamental operating principle of Kitepower's AWES.

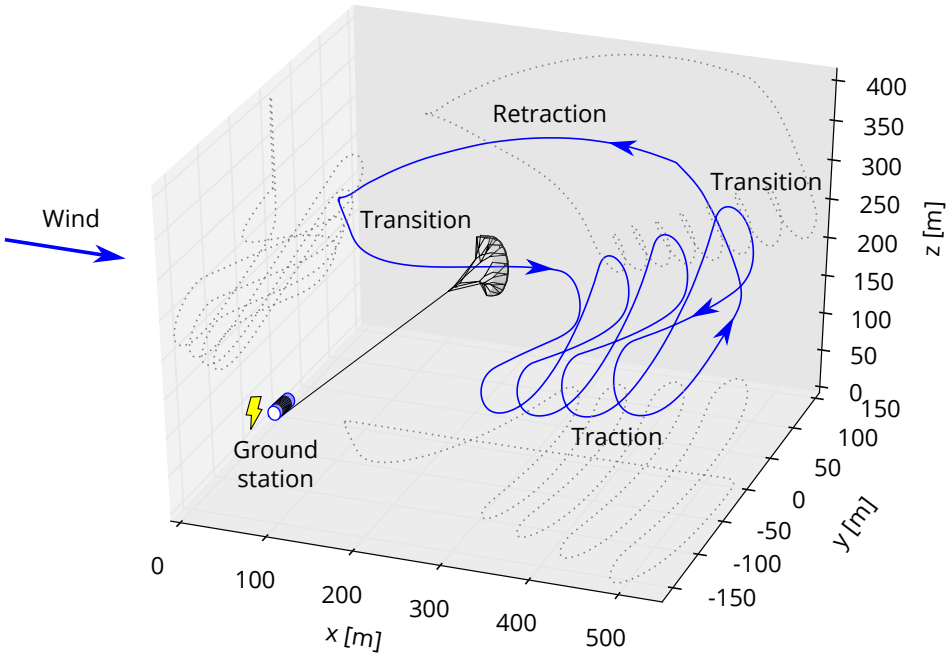

Figure 2.4: Example of a pumping cycle flight trajectory with indicated flight phases [44].

2.1.2. AWES performance indicators

In the assessment and design of AWESs, a range of performance indicators can be employed, each reflecting distinct aspects of system performance and highlighting the technology's interdisciplinary nature. These indicators include, among others, the power curve, annual energy production (AEP), sustainability, system redundancy, operational safety, and cost-effectiveness, which are listed below.

- For each AWES, the power curve indicates the amount of power the system can produce at specific wind speeds. In Figure 2.5, an example of such a power curve is given, with relevant wind speeds and powers indicated. Below the cut-in wind speed, the kite cannot generate enough lift. At the rated wind speed, the system-specific maximum power is obtained. Above this wind speed, the system must take safety precautions to prevent exceeding its maximum forces. At the cut-out wind speed, the system cannot fly reliably without risking component failure.
- AEP, typically measured in megawatt-hours per year (MWh/year), provides a direct quantification of the net electrical energy generated over an operational period. With the power curve, a density distribution of different wind speeds throughout the year, and operational limitations, the yearly output of an AWES can be determined. It provides a clear, quantifiable comparison between different AWESs.
- Sustainability as a performance metric addresses the system's environmental footprint, including material use, life-cycle emissions, land use, and recyclability. While essential for evaluating long-term ecological impact and regulatory compliance, sustainability assessments can be complex and data-intensive, often relying on assumptions about manufacturing processes, supply chains, and end-of-life scenarios that are difficult to model during early-stage design [22].
- System redundancy refers to a system's resilience and ability to maintain functionality despite faults or component failures. High redundancy can improve reliability and reduce downtime, which is critical for consistent energy delivery.

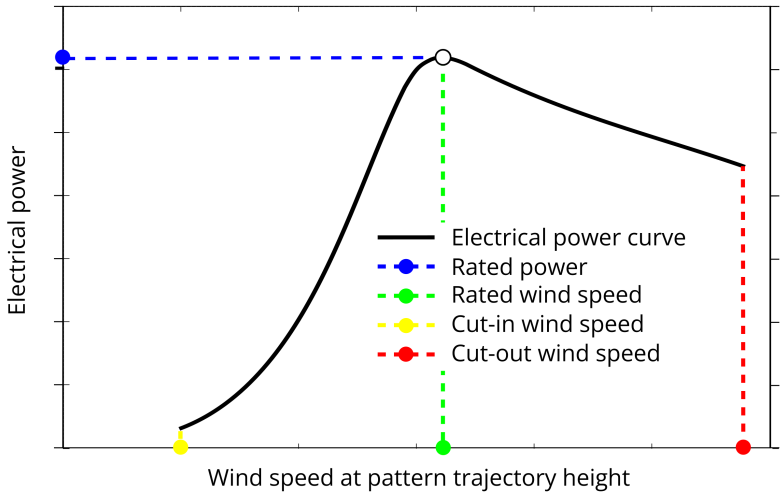

Figure 2.5: General power curve for an AWES [46].

- Operational safety combines the risks associated with system deployment, flight control, and failure modes, which are particularly important for systems operating in public airspace or near populated areas. While safety is non-negotiable in commercial applications, quantifying it as a performance metric can be difficult.
- A more quantifiable metric is the cost-effectiveness of a system, which integrates capital costs, operational expenditures, and expected energy output to assess its economic viability. This metric is especially important for the success of start-up companies like Kitepower.

Each of the mentioned performance indicators captures a different dimension of system success. Depending on the goals of a given study or design phase, the relative importance and applicability of these metrics may vary, and trade-offs between them are often inevitable.

2.2. Key geometric kite design parameters

The aerodynamic characteristics of a LEI kite are governed by both its airfoil shape and its global planform geometry. First, LEI-specific airfoil design parameters are given in Section 2.2.1, and the global planform parameters are given in Section 2.2.2.

2.2.1. Airfoil design parameters

Unlike conventional rigid wings, an LEI kite airfoil consists of a pressurised leading-edge (LE) tube combined with a single-skin canopy, resulting in a non-enclosed profile and a characteristic recirculation region directly downstream of the LE. This fundamental geometric difference limits the applicability of classical airfoil parametrisation methods, such as NACA series profiles.

Due to these differences, a dedicated parametrisation approach has been proposed for LEI kite profiles. Masure [34] describes the airfoil geometry using a small number of parameters that define the LE tube diameter and the canopy shape via Bézier curves. This formulation enables systematic geometric variation while remaining compatible with aerodynamic simulation tools. A schematic overview of this parametrisation is shown in Figure 2.6, where t denotes the LE tube thickness, η is the chordwise location of maximum camber, κ is the camber height, ϕ and λ are tension parameters for the front and rear splines, respectively, and δ is the reflex angle.

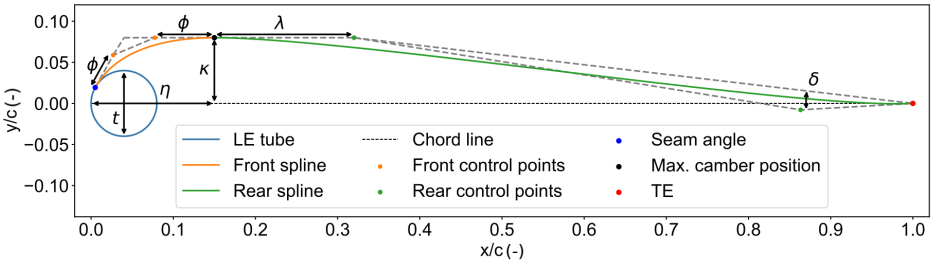

Figure 2.6: LEI kite airfoil parametrisation by Masure [34].

2.2.2. Wing design parameters

Beyond the local airfoil shape, several global geometric parameters have a first-order influence on the aerodynamic performance and controllability of LEI kites. The arc width determines the relationship between top- and side-projected areas, affecting stability and turning behaviour. A schematic illustration of narrow and wide arc geometries is shown in Figure 2.7. The arc's height is scaled accordingly. Also, sweep and aspect ratio (AR) influence aerodynamic efficiency and load distribution in a manner analogous to conventional wings, with higher ARs generally yielding improved lift-to-drag ratios.

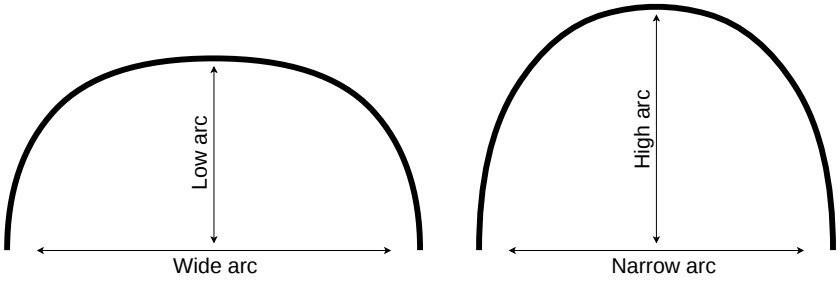

Figure 2.7: Arc width and height comparison.

Additional planform parameters such as taper ratio and twist distribution affect spanwise lift distribution, turning authority, and overall kite stability. Furthermore, the geometry and placement of bridle attachment points influence the effective angle of attack and load transfer between the kite and tether system.

2.3. Kite analysis and modelling tools

The design of AWESs is inherently multidisciplinary, requiring the integration of aerodynamics, structural mechanics, flight dynamics, and power performance analysis. Current design methodologies typically combine expert knowledge with experimental testing and numerical simulations. Over recent decades, a broad range of computational tools has been developed to support the analysis and design of kite wings and complete AWESs at varying levels of modelling fidelity.

This section provides an overview of computational and simulation tools commonly reported in the literature for analysing kite-based AWESs. The tools are categorised by primary purpose, ranging from aerodynamic modelling of kite wings to system-level performance evaluation. The three-dimensional design of a kite wing can be performed using various approaches, with most general-purpose computer-aided design (CAD) software offering substantial support. SurfPlan^{TM}, however, is a specialised tool dedicated to the three-dimensional geometric

definition of soft kite wings, enabling detailed modelling of canopy geometry, panel layout, bridle line configuration, and shape morphing capabilities [51]. The software is available in a professional version with extended functionality and a hobby version with limited features.

2.3.1. Aerodynamic and structural modelling tools for kite wings

A variety of computational tools is available for the two- and three-dimensional aerodynamic and structural analysis of flexible and semi-rigid wings, many of which are directly applicable to kite wing design. The most commonly used approaches are summarised below.

- **XFOIL [14]:** A two-dimensional viscous/inviscid airfoil analysis code that is widely used for preliminary airfoil design and the estimation of aerodynamic coefficients. Although it is limited to two-dimensional flow, XFOIL is frequently used for initial kite airfoil selection and performance screening.
- **Computational Fluid Dynamics (CFD):** CFD provides a high-fidelity approach to aerodynamic analysis by resolving the full flow field around a geometry within prescribed spatial and temporal resolution limits. Commercial software packages, such as Ansys [3], offer robust and validated solvers but are associated with high licensing costs. Open-source alternatives, including OpenFOAM [55, 39], are therefore widely used in academic research. To reduce computational expense, Masure developed a machine-learning-based regression model that predicts the two-dimensional aerodynamic characteristics of LEI kite airfoils based on the parameterisation shown in Figure 2.6 [34]. This approach provides a computationally efficient alternative to conventional CFD simulations while maintaining high accuracy.
- **Lifting line method (LLM) and vortex lattice method (VLM):** In the lifting line method, the three-dimensional circulation around a wing is represented by a bound vortex, typically located at the quarter-chord position [27]. The VLM is a three-dimensional implementation of this concept, discretising the wing into a lattice of horseshoe vortices. VLM is therefore well-suited for estimating lift distribution and induced drag during early-stage kite wing design. A widely used implementation is the Athena vortex lattice (AVL) code [15, 9].
- **Vortex Step Method (VSM):** The VSM is an adaptation of the VLM in which the aerodynamic forces are evaluated at the three-quarter-chord location [11]. It enables fast aerodynamic simulations and, in contrast to classical VLM formulations, provides improved accuracy for low-AR and unconventional wing geometries.
- **ASKITE:** ASKITE is a dedicated modelling tool developed for the three-dimensional aero-structural analysis of kite wings in AWE applications [11]. It combines the aerodynamic models proposed by Masure [34] and the VSM [11] with a particle-based structural model, in which the kite structure is represented as a spring–damper system. As in-flight kite deformations have shown to significantly impact the shape of a kite, analysed by Haanen [21], it is important to include a modelling tool that is able to capture deformations.

2.3.2. AWES simulation and performance estimation tools

At the system level, a range of modelling tools has been developed to estimate the performance of AWESs. Many of these tools explicitly depend on wing geometry and aerodynamic characteristics and differ in terms of modelling fidelity and computational cost.

- **Luchsinger [32]:** A quasi-steady, massless performance model that computes the relative traction power during reel-out and reel-in phases along a straight flight path. Aerodynamic properties are represented using simplified powered and depowered operating

states.

- **van der Vlugt [54]:** A quasi-steady AWE model that includes kite mass and represents reel-out flight using Lissajous patterns. As in the Luchsinger model, aerodynamic coefficients are assumed constant within distinct power states.
- **AWETrim [10]:** A quasi-steady model (QSM) of the complete pumping cycle used to estimate power output based on aerodynamic coefficients and system geometry. The kite is modelled as a point mass, while inertial effects, including centrifugal and mass-related accelerations, are accounted for. A trim condition is assumed at each time step, and the flight trajectory is optimised within the simulation to maximise power output.
- **AWEbox [47]:** A modelling and optimisation framework for the control of AWESs comprising multiple kites. The framework primarily targets rigid-wing kite configurations and supports a wide range of system architectures, with a particular focus on multi-kite control strategies and dynamic simulation.
- **Full dynamic simulation [17]:** A high-fidelity dynamic simulation approach for pumping-cycle AWESs that resolves kite aerodynamics, tether dynamics, and ground station behaviour. While offering the highest level of modelling detail among the discussed approaches, such simulations also require significantly greater computational resources.

2.4. Multidisciplinary design analysis and optimisation

The design of complex engineering systems, such as aircraft or AWESs, involves multiple interacting physical phenomena that cannot be treated independently. Aerodynamic performance, structural integrity, control behaviour, and system-level performance metrics are strongly coupled, and decisions made within one discipline directly affect the others. Multidisciplinary design analysis and optimisation (MDAO) has emerged as a systematic approach to address this complexity by integrating multiple disciplinary models within a unified design framework.

MDAO can be defined as an assemblage of methods and procedures aimed at identifying optimal designs for complex systems governed by coupled physical disciplines, evaluated against a set of specified performance criteria [50]. Rather than relying on sequential or discipline-isolated design processes, MDAO enables the simultaneous consideration of multiple interacting models, allowing design trade-offs to be explored more consistently and efficiently. The impact of adopting MDAO-based design approaches on system performance, cost, reliability, and development time is illustrated in Figure 2.8. Martins found that MDAO generally increases a system's performance, reduces total cost, and reduces uncertainties, all within a reduced time scope.

Within an MDAO framework, each engineering discipline is represented by a dedicated analysis model, such as aerodynamics, structures, controls, or performance. These models exchange information through defined coupling variables, forming a multidisciplinary analysis (MDA). When an optimisation algorithm is added to this analysis loop, the framework becomes a multidisciplinary design optimisation (MDO) problem. The objective of the optimisation is typically expressed as a scalar objective function, which may represent system performance, efficiency, cost, or robustness, depending on the design goals.

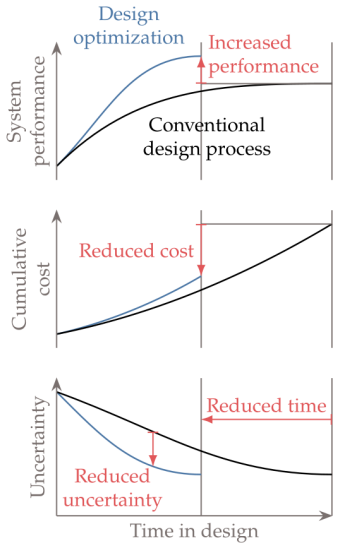

Figure 2.8: Influence of MDAO on the engineering design process [33].

In a general form, an MDO problem can be expressed as [30]:

$$\begin{aligned} \text{minimise} \quad & F(x, y) \\ \text{with respect to} \quad & x \in \mathbb{R}^n \\ \text{subject to} \quad & y_i = E_i(x, y), \quad i = 1, \ldots, N, \\ & g_j(x, y) \leq 0, \quad j = 1, \ldots, p, \\ & h_k(x, y) = 0, \quad k = 1, \ldots, q, \end{aligned} \tag{2.1}$$

where x denotes the design variables, y the coupling variables between disciplines, E_i the disciplinary analysis models, and g_j and h_k the inequality and equality constraints, respectively.

To obtain physically meaningful and feasible designs, all relevant disciplines must either be explicitly included in the MDAO framework or be represented through appropriate constraints. Neglecting key disciplines may lead to infeasible or unrealistic solutions. For example, optimising a wing purely for aerodynamic efficiency, without structural constraints, could result in a slender configuration unable to sustain operational loads. The interdependence of engineering disciplines and their influence on system design is illustrated in Figure 2.9.

2.4.1. System architectures

The manner in which disciplinary analyses are coupled and coordinated within an MDAO framework is defined by the chosen architecture. Several standard architectures have been identified in literature, including all-at-once (AAO), simultaneous analysis and design (SAND), individual discipline feasible (IDF), and multidisciplinary feasible (MDF) architectures [33]. Among these, IDF and MDF are most commonly applied in practical engineering studies.

In the IDF architecture, disciplines are executed independently, and coupling consistency is enforced through additional constraints within the optimisation loop. This decoupling allows the disciplinary analyses to be evaluated in parallel, potentially reducing computational cost, but it introduces additional consistency constraints that must be satisfied for convergence [24]. In contrast, the MDF architecture explicitly couples the disciplines through an iterative multidisciplinary analysis, ensuring that all coupling variables are consistent at each optimisation iteration. While this approach simplifies constraint handling, it generally increases

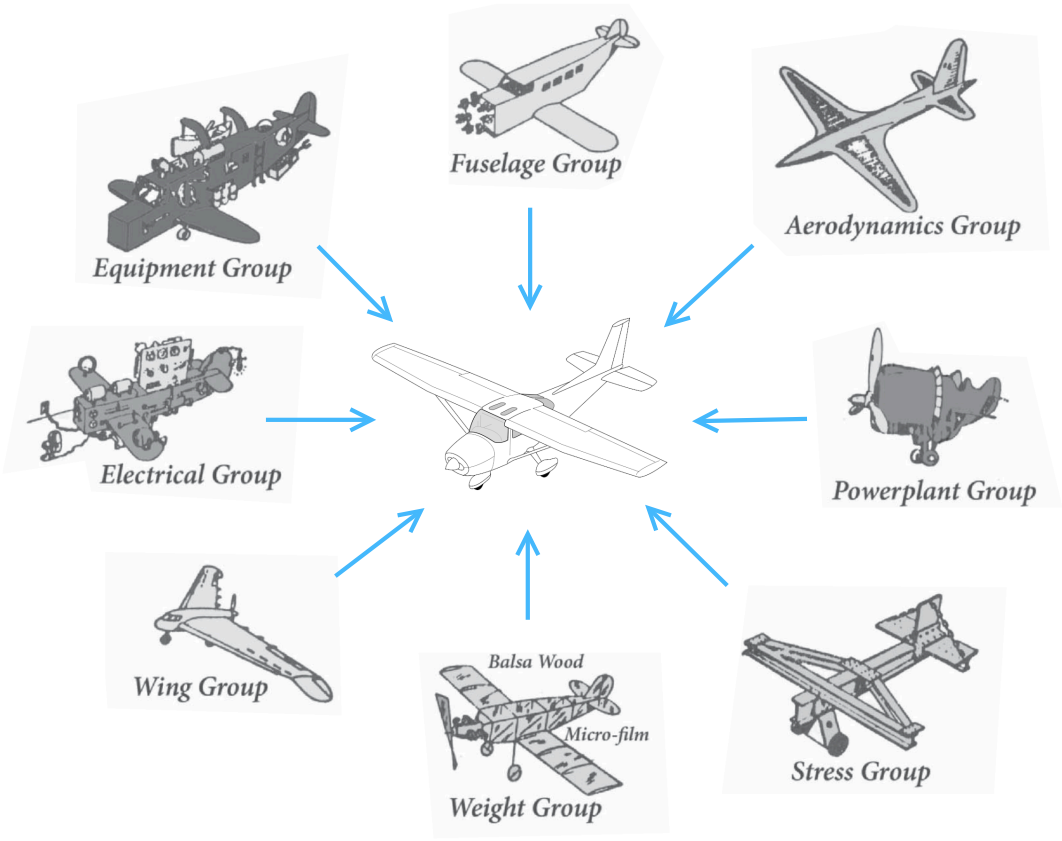

Figure 2.9: Influence of interacting engineering disciplines on aircraft design; originally from [36], inspired by [43].

computational cost due to the nested iteration required to achieve convergence.

The choice of MDAO architecture involves a trade-off between implementation complexity, computational efficiency, and numerical robustness. This trade-off is particularly relevant for early-stage design studies, where simplified models and modular toolchains are often preferred. A complex engineering design problem can also result in hybrid architectures that implement features from the aforementioned architectures.

2.4.2. Extended design structure matrix

The extended design structure matrix (XDSM) is a widely used graphical representation for visualising MDAO architectures and data flow within multidisciplinary frameworks. XDSM diagrams explicitly show the involved disciplines, their inputs and outputs, the optimisation process, and the sequence of information exchange, making them well-suited for describing complex coupled systems.

An example of an MDF architecture represented using XDSM is shown in Figure 2.10. The diagram illustrates the interaction between the optimisation block, the multidisciplinary analysis block, individual disciplinary analyses, and the objective and constraint evaluation. Here, the primary data flow is indicated by the black line, and the numbers assigned to each component indicate the execution order.

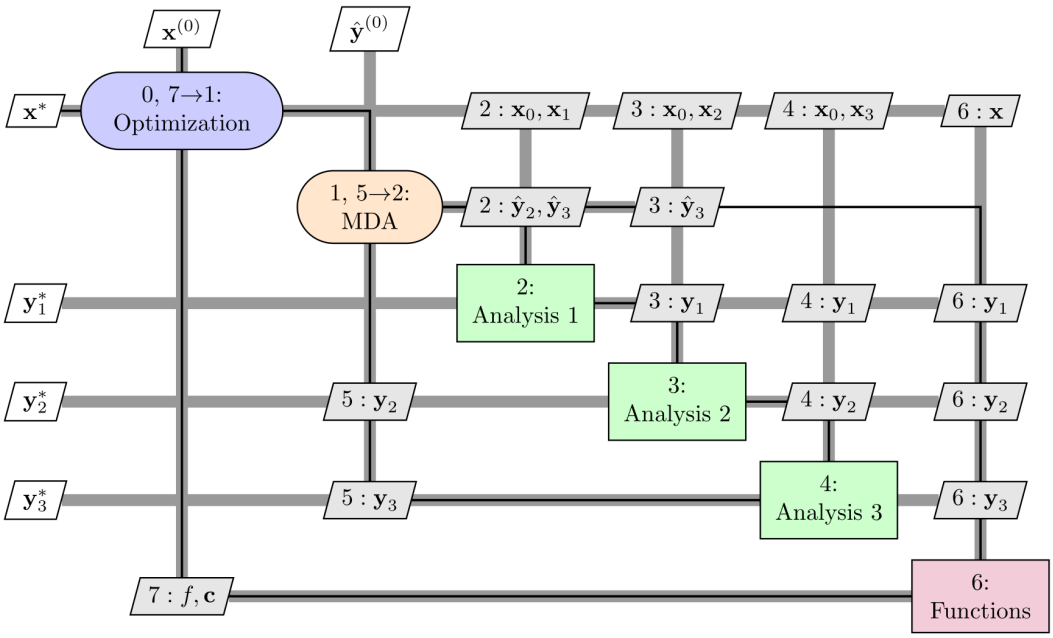

Figure 2.10: Example of an MDF architecture represented using XDSM [24]. The blocks represent disciplines and other steps in the execution of the optimisation framework, and the black line indicates the execution order.

Within an XDSM representation, the optimisation block provides design variables to the multidisciplinary analysis, which coordinates the execution of the disciplinary models. The disciplinary analyses exchange coupling variables through the MDA until consistency is achieved. The resulting outputs are then passed to the function block, where objective functions and constraints are evaluated and returned to the optimiser. The data flow for each of these components is illustrated in Figure 2.11.

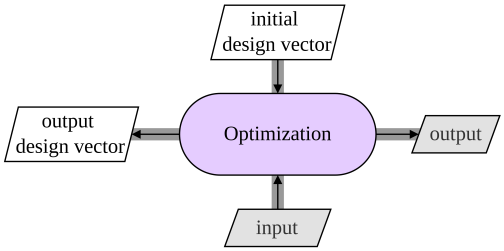

(a) Optimisation block.

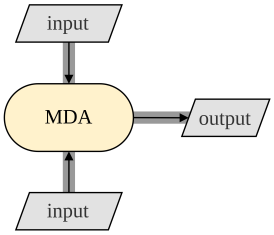

(b) Multidisciplinary analysis block.

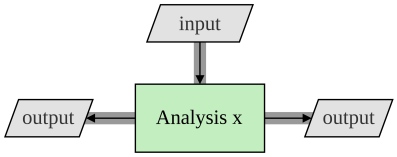

(c) Disciplinary analysis block.

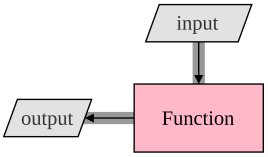

(d) Function evaluation block.

Figure 2.11: Data flow between execution blocks in an XDSM representation; optimisation (a), MDA (b), discipline (c), function (d).

In conclusion, an XDSM provides a comprehensive and detailed way to represent multidisciplinary frameworks, such as those used in MDAO. It clearly illustrates the information flow, execution sequence, and functions of the different disciplines within a single structured format, making it a valuable tool in engineering practice.

2.4.3. Optimisation algorithms

The optimisation component of an MDAO framework relies on numerical algorithms to systematically explore the design space and identify improved or optimal solutions. These optimisation algorithms can broadly be classified into gradient-based and gradient-free methods, each with distinct advantages and limitations depending on the characteristics of the design problem [33].

Gradient-based optimisation algorithms utilise derivative information of the objective function and constraints with respect to the design variables [33]. When accurate gradient information is available, these methods are generally computationally efficient and exhibit rapid convergence, particularly for smooth and well-behaved problems. As a result, gradient-based methods are commonly applied to large-scale engineering optimisation problems in which the design space is continuous, and the governing models are differentiable. However, their performance can degrade when gradients are noisy, discontinuous, or unavailable, which is often the case when using complex simulations or black-box models.

Gradient-free optimisation algorithms, also known as derivative-free methods, do not require gradients and instead rely on function evaluations to guide the search [33]. Examples include evolutionary algorithms, pattern search methods, and surrogate-based optimisation. These approaches are generally more robust to non-smooth, multi-modal, or noisy objective functions, but this robustness typically comes at the cost of increased computational effort due to a larger number of function evaluations.

Selecting an appropriate optimisation algorithm is therefore not straightforward and strongly depends on the nature of the engineering problem, the fidelity of the underlying models, and the available computational resources [33]. No single algorithm is universally optimal, and different problems may benefit from different optimisation strategies. Consequently, optimisation algorithm selection is often problem-specific and may require empirical evaluation or adaptation to achieve satisfactory performance within a given MDAO framework.

2.4.4. Demonstration of MDO application on wing design.

In the search for novel wing concepts, Bons *et al.* applied an MDAO approach to aerodynamic wing design [7]. The objective of the study was to minimise aerodynamic drag by varying geometric design parameters, including twist, chord length, dihedral, span, sweep, and airfoil shape. The analysis was performed using a coupled aero-structural model that integrates aerodynamic and structural disciplines to account for their mutual interactions.

A gradient-based optimisation algorithm was employed to identify optimal solutions. To investigate the sensitivity of the optimisation process to initial conditions, multiple optimisation runs were conducted with varying initial conditions. The resulting design outcomes, illustrated in Figure 2.12, revealed multiple locally optimal solutions. This result highlights the multimodal nature of complex wing design problems and demonstrates that such design spaces may not exhibit a single globally optimal solution. Therefore, the choice of optimisation algorithm and problem formulation plays a critical role in effectively exploring and exploiting the design space.

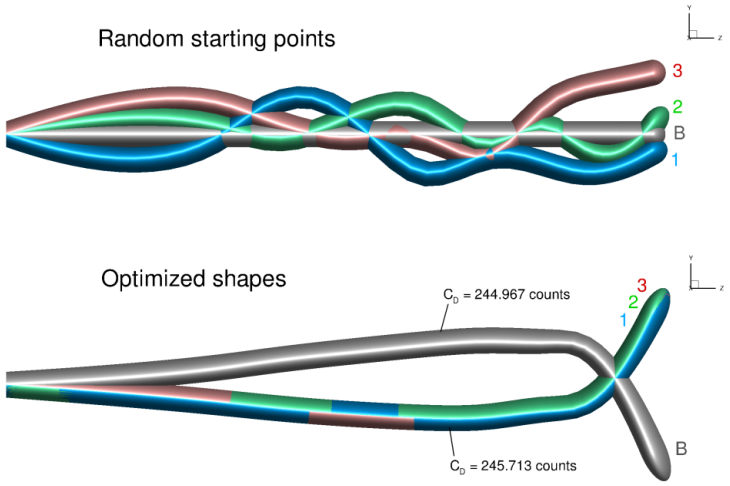

Figure 2.12: Two optimised wing shapes found in wing design optimisation utilising MDO with random starting geometries [7].

2.5. Discussion and research objectives

The AWE industry is evolving rapidly, driven by the need for sustainable and scalable energy solutions. A key factor in this fast development is the ability to perform frequent design iterations, allowing systems to improve quickly without the long delays and high costs associated with traditional prototyping and testing. However, for AWE technologies to reach large-scale deployment, the performance of individual components, such as the kite system, must be further optimised. Achieving this requires a design approach that supports rapid, low-cost iteration without relying on extensive physical flight testing.

Kite design in AWESs is inherently multidisciplinary, involving many interactions between aerodynamics, structural mechanics, controls, and materials. Currently, no single design tool integrates all these aspects in a unified framework. To manage this complexity and accelerate the design process, MDAO emerges as a powerful methodology. Its integrative and iterative nature makes it well-suited for optimising complex engineering systems, such as LEI kites.

This research investigates the integration of MDAO into the geometric design process of LEI kites, aiming to address current limitations in design efficiency and performance prediction. To guide this investigation, the following research objective is posed:

How can a MDAO framework be applied to optimise the geometric design of LEI kites for AWESs, with the objective of increasing predicted power output, within the scope of a conceptual design study for systems such as Kitepower?

To fragmentise the work required to attain the research objective, the following research questions (RQs) are defined:

RQ-1 Which **geometric parameters** used in current kite design iterations have the greatest influence on the aerodynamic performance and power output of AWE LEI kites?

RQ-2 Which **disciplines** are used to design a kite geometry for AWESs?

RQ-3 To what extent can a LEI kite design be improved by implementing a **MDAO** framework?

RQ-4 To what extent do **environmental conditions** influence the optimised kite design for an AWES?

Research question 1 addresses which geometric parameters have the largest influence on the aerodynamic performance of AWE LEI kites. A wide range of parameters can alter kite geometry, each with a different impact on aerodynamic behaviour and power generation. However, the optimisation in this research will inevitably be constrained by computational cost and iteration time. Consequently, this process must focus on a limited subset of parameters expected to most strongly influence performance. The central aspect of answering Research question 1, therefore, lies in identifying the most influential geometric parameters. It is hypothesised that the arc shape and the AR have the greatest influence on the kite's performance and, consequently, on the power output of the AWES.

Research question 2 concerns the identification of the disciplines involved in kite geometry design. The tools discussed in Section 2.3 appear to collectively cover the primary design disciplines required for kite development. A key step in determining the appropriate toolchain is therefore to first analyse and document Kitepower's current design workflow. Based on this inventory, the selected tools can be integrated into a structured toolchain that reflects the existing design process while enabling automated iteration. The functionality of each component within this workflow must then be validated to ensure reliable operation. Given the current lack of a fully formalised design workflow, it is expected that intermediate post-processing steps will be required between several stages of the toolchain.

Research question 3 focuses on assessing the potential improvements that an MDAO toolchain can provide for LEI kite design. Although implementing a MDAO workflow is not the only approach to developing a design iterator, this research focuses on evaluating its potential for kite design. To evaluate the improvements, the current design iteration process must first be identified, as outlined in Research question 2. The performance of the proposed workflow should be compared with the current design method using both quantitative and qualitative measures. Quantitatively, a key indicator is the required iteration time, while qualitatively, the assessment considers whether the toolchain leads to substantial improvements in the physical system. Once the workflow has been validated, Research question 3 can be answered.

Finally, Research question 4 investigates the influence of environmental conditions on the optimised kite design. Environmental factors play a crucial role in AWES performance, with wind speed and the wind shear profile among the most influential parameters. By analysing a representative wind condition for a potential AWES deployment location, it is possible to determine the optimal flight altitude and other relevant operational parameters. Incorporating these environmental characteristics into the optimisation process allows the kite geometry to be tailored to the specific operational conditions. Such location-specific optimisation is expected to influence the resulting kite design and lead to notable improvements in the power output of an AWES.

In addition, appropriate validation procedures must be established to assess the reliability and quality of the generated designs. The existing approach for validating AWES performance should therefore be reviewed, its limitations identified, and potential improvements considered for the new workflow. One possible validation method is to construct a physical kite and evaluate its performance under real operational conditions. Although this approach provides valuable experimental data, it is both costly and time-consuming due to the production and testing requirements. Furthermore, this approach contradicts the main objective of this research, which is to simplify and accelerate the geometric design iteration process for AWE LEI kites. As an alternative, validation can be performed computationally by employing previously validated modelling tools. This approach enables rapid evaluation of multiple design iterations while maintaining a reasonable level of confidence in the predicted performance.

3

Methodology

A framework that assumes responsibility for designing a complex structure, such as a LEI kite wing shape, requires the correct implementation of all effects and therefore disciplines. In this section, the known disciplines are identified and summarised into an approach to the framework's functionality.

First, the general research approach is explained in Section 3.1. During initial design concept framing, the absence of a kite ontology was identified, which is further explained in Section 3.2. The reference kite for this toolchain is introduced in Section 3.3, along with the initial parametrisation steps.

3.1. Research approach

This research aims to develop a scalable and modular framework for the design and analysis of AWESs. Since the AWE industry is still primarily in the research and development phase, substantial changes in design methodologies and computational tools are to be expected. Consequently, it is essential to first map and understand the existing methods, including their underlying assumptions and limitations. Establishing an architectural foundation for an MDAO toolchain is an important step toward supporting future research, as it facilitates the faster, more efficient implementation of new models and methods. A modular toolchain enables a range of applications to be developed and integrated, thereby accelerating progress in the field.

3.1.1. Design-oriented and model-based research

Focusing the toolchain on kite design offers an opportunity to generate unique insights, as the kite-based AWES design workflow remains relatively underexplored. Although aerodynamic performance and operational behaviour strongly influence the potential power production of AWESs, their integration has received limited attention. This research, therefore, adopts a combined perspective that considers both operational requirements and the geometric design space of LEI kites.

Existing simulation tools typically address individual elements of this workflow, but a coherent architecture is required to link these tools into a consistent modelling chain. A chain is only as strong as its weakest link, and the same principle applies to this toolchain. As a result, careful consideration must be given to each model's assumptions and limitations. In a model-based research approach, the toolchain architecture is designed to be modular, allowing individual

models to be exchanged, updated, or extended. This modularity enables alignment between the required fidelity and the analysis's intended objectives. Future development can therefore proceed by incorporating new and improved models, such that the combined framework progressively approximates the physical system with increasing accuracy.

3.1.2. Framework and workflow

A modular framework requires ease of use and rapid integration of new models. The specific integration requirements depend on the simulation tools that are incorporated into the toolchain. To enable seamless integration, it is necessary to identify how kite geometry affects physical performance and to define the associated design dependencies.

To preserve the geometric integrity of the kite during reshaping, a tool that combines a well-defined representation of the kite geometry with the ability to modify its shape to specified design requirements is needed. Since no tool was found that combines these functionalities, a methodology has been developed. The three-dimensional geometric definition proposed for this purpose is described in Section 3.3. The first step in reshaping a complex geometry, like a kite wing, is to determine which parameters will be varied in the optimisation workflow. Since increasing the number of design variables also increases computational cost, parameter selection must be performed carefully. The process of parameter exploration and selection is discussed in Section 3.3.2.

3.2. The need for a universal kite ontology

When integrating multiple simulation tools into a computational design framework, a clear and consistent data exchange mechanism is essential. Without a shared data structure, each tool-to-tool interface requires custom data formatting. Such ad hoc solutions increase development effort, reduce transparency, and introduce errors that may propagate through the toolchain, significantly affecting simulation results. As the number of coupled models increases, this approach becomes increasingly unscalable.

To address similar challenges in wind energy research, initiatives within the International Energy Agency (IEA) wind programme have focused on developing harmonised, ontology-based data formats. In the wind turbine domain, this led to the creation of WindIO within IEA wind task 15, providing a tool-independent ontology for describing complete wind turbine systems [18]. Building on the philosophy established in the wind turbine domain, the work presented in this thesis introduced the development of a first version of an ontology for AWES, referred to as awesIO [20]. This effort was initiated as a collaborative initiative within the TU Delft AWE research group, with the aim of defining a consistent tool-independent data structure for kite-based systems. The initial development focused on establishing a practical ontology capable of supporting automated data exchange within a rapidly developing industry.

Following its initial development, awesIO was subsequently adopted within IEA Wind Task 48 as a basis for further community-wide standardisation and refinement [20]. Due to its multidisciplinary nature and reliance on automated data exchange between heterogeneous models, the developed toolchain forms a particularly suitable testing platform for the awesIO ontology. The adoption of a shared data structure has the potential to facilitate transparent exchange of data and simulation tools between research groups and companies worldwide, thereby accelerating technological advancement and enabling more independent validation by external parties.

3.3. Reference kite definition and parametrisation

Since kite designs are very complex, a proven design is taken as the reference kite. The TU Delft AWE research group developed a kite, called the V3, which has been extensively tested. In addition to flight data, the geometrical data of the kite and bridle system are also known, making it a good test candidate for the geometrical optimisation toolchain. This section covers the terminology for a LEI kite used in ground-gen crosswind AWESs. Also, the definition of this kite in computational space is explained. First, the kite is described in Section 3.3.1, after which the parameters used in kite design are identified and selected in Section 3.3.2.

3.3.1. The TU Delft V3 kite

A schematic drawing of the TU Delft V3 kite is given in Figure 3.1, indicating the components related to the kite control unit (KCU), bridle system and wing. The front bridle is directly attached to the tether, while the rear bridle is connected to the KCU. The KCU controls the kite's airborne controls, with two functions: steering and depowering. Steering is controlled by asymmetrical actuation in the steering lines, which induces a pulling force on the trailing edge of one side of the kite and releases the lines on the other side. The asymmetrical change of the kite's orientation induces a turning behaviour. Depowering is the act of extending the rear bridle lines, thereby reducing the angle of incidence relative to the KCU orientation. The steering and depower tapes connect the bridle lines to the actuators in the KCU that control the line lengths.

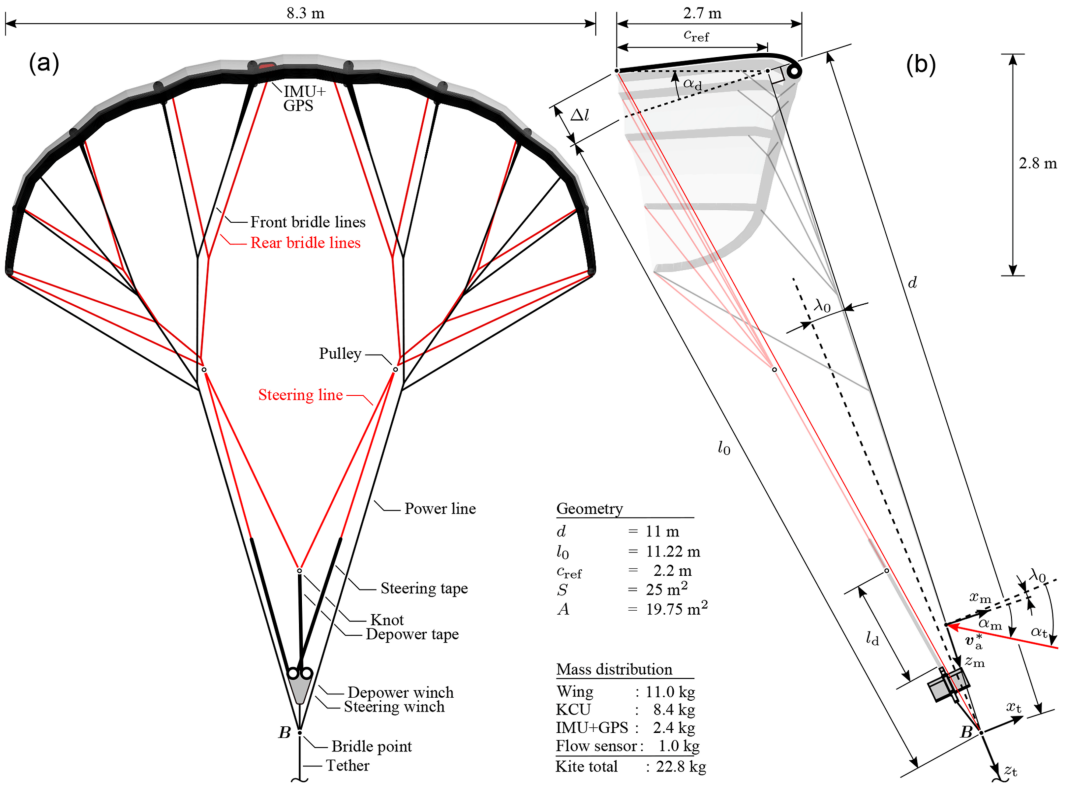

Figure 3.1: Front view (a) and side view (b) of the TU Delft V3 kite [38].

The V3, like most kites, has a CAD representation of its geometry in SurfPlan [51]. Also, the V3 kite has a geometric definition in SurfPlan, which is used as the baseline geometric definition of an LEI AWE kite. In SurfPlan, the real-life kite is discretised into a 3D-coordinate space, for

which the orientation of the axis system is given in Figure 3.2. The discretised definition is built up from sliced wing data and bridle coordinates. The wing is sliced into 36 parts, each containing positional, orientational, and airfoil data. Next to this, information on the location and diameter of the inflated structure of the kite is included, consisting of the LE tube and chord-wise struts. SurfPlanAdapter, developed by Poland [40], can translate SurfPlan data into a format used by an aerodynamic analysis tool.

(a) Side view orientation. **(b)** Top view orientation.

Figure 3.2: Axes system orientation of the TU Delft V3 kite computational geometry [46].

3.3.2. Parametrisation of a LEI kite wing

When omitting the bridle design, assuming it can be designed to the desired functionality, the kite design can be approached similarly to a conventional wing design. Approaching wing design from an initial design phase, the following design parameters are considered important:

- Area S (m^2)
- Span b (m)
- Taper ratio λ (-)
- Sweep Λ (°)
- Dihedral Γ (°)
- Airfoil shape
- Standard mean chord SMC (m)
- Twist (°)

Computational power and time increase significantly with the number of parameters that will be optimised. Therefore, it is important to reduce the scope of this toolchain as much as possible, without removing important design parameters. First, the possible relations between design parameters are explored, and then a selection is made.

The first parameter, area S, is of great essence, since surface area is directly correlated to the lift force a wing is able to produce, see the lift equation:

$$L = \frac{1}{2}\rho v^2 S C_L, \tag{3.1}$$

where L is the lift force, v the wind velocity, S the surface area of the wing, and C_L the wing lift coefficient [2]. The lift force significantly impacts a kite's pulling capability and its performance as an AWES. Since the purpose of this toolchain is to compare kite designs, not to scale a system, it is chosen that the wing area remains constant throughout the optimisation.

Secondly, the wing span b, which is closely linked to the surface area by definition:

$$AR = \frac{b^2}{S}, \tag{3.2}$$

where AR is the aspect ratio, also referred to as the slenderness of the wing. Rewriting to a function for the span resolves to:

$$b = \sqrt{AR \cdot S}. \tag{3.3}$$

Since area is a geometrical property following $S = b \cdot SMC$, where SMC is the standard mean chord length, the AR can be written as a function of SMC:

$$AR = \frac{b^2}{b \cdot SMC} = \frac{b}{SMC}. \tag{3.4}$$

SMC can be defined by the sum of the chord lengths of a discretised wing from:

$$SMC = \int_0^b c \, \frac{b}{\delta b} = \frac{\sum_o^i c_i}{i}, \tag{3.5}$$

where c_i is the chord length of the discretised wing section. This close connection of surface area, span, and chord length is the reason why AR will be used as one of the design parameters in the optimisation of a kite wing. The taper ratio in a wing is often used for structural considerations, with less impact on the direct aerodynamics. Sweep is primarily implemented to negate compressibility effects on aircraft wings, whereas the designed subsonic kite system does not.

Dihedral, or in the case of a LEI kite, anhedral, translates to the curvature of the kite's arc. The arc shape relates the kite's projected top area to its projected side area. This ratio balances the pulling force of a kite and steering behaviour and stability, and is therefore of great importance. Also, structural integrity is dependent on the arc shape, since a flatter wing is more prone to collapsing due to the sideways force component of the bridle system.

The airfoil shape is what mainly differentiates a LEI kite shape from conventional aircraft wings. Since the structural stability is obtained from an inflated tube at the LE, a cross-section of the wing has unique features, as can be seen in Figure 2.6. To optimise the airfoil shape, all parameters as defined by Masure can be adjusted within predefined bounds.

Also, twist is a factor used in kite wing design, and has a great impact on the stability of the kite. Since stability requirements are not included in the current optimisation toolchain, this factor will be considered less important than the aforementioned parameters.

The design parameters of a kite can be extended to levels of detail that would resemble a true representation of the physical kite. Since computational time for optimisation scales with the number of design parameters, the number should be reduced as much as possible. Given its significant influence on the kite wing's geometry, AR is treated as a separate parameter. Also, the airfoil shape will be optimised, but due to the limited number of parameters, only kappa (the thickness-to-chord ratio) will be optimised. The arc shape is the last design condition to be implemented in the optimisation. This, however, is due to the many wing sections (35) not being evident, as optimising 35 individual anhedral angles would greatly increase the number of design parameters. The first step is to use the quarter-chord arc as the reference arc for the chord placement and anhedral distribution. This is done to preserve the sweep angle during optimisation, which, aerodynamically, is defined relative to the quarter-chord location. In Figure 3.3, the computational structure of the V3 kite is shown, with in purple the quarter-chord location indicated.

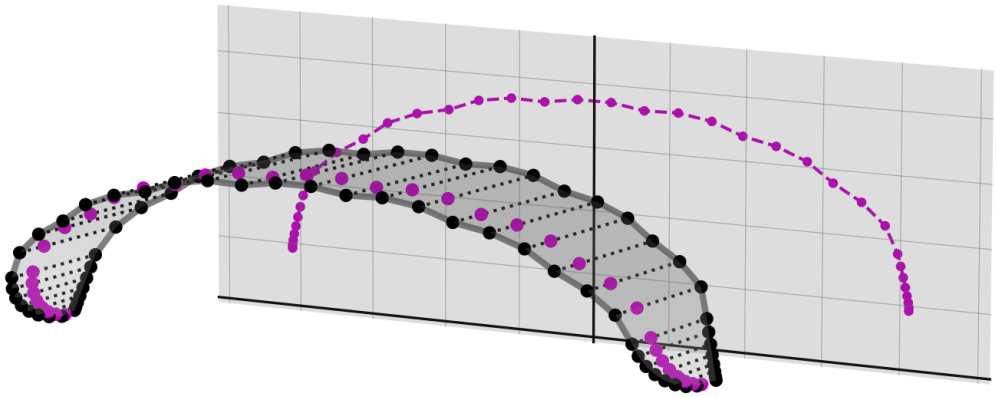

Figure 3.3: TU Delft V3 kite structure with projected quarter-chord arc.

Extracting this quarter-chord arc and plotting this in y-z coordinate space (front-view) retrieves the arc in Figure 3.4, where, due to symmetry, only half the arc is shown. As can be seen, the arc does not follow a smooth line; instead, it shows bumps. Struts are located at the lower points, such as at y = 0.75 m and y = 2 m. However, to simplify the reshaping process, the zigzag shape is omitted from the optimisation, and a simplified curve will be used to describe the kite. This curve can be constructed in various ways, such as splines, CST curves, catenaries, ellipses, and Bézier curves. Most of these options do require multiple parameters to construct an arc similar to a kite, with the flexibility needed for design optimisation.

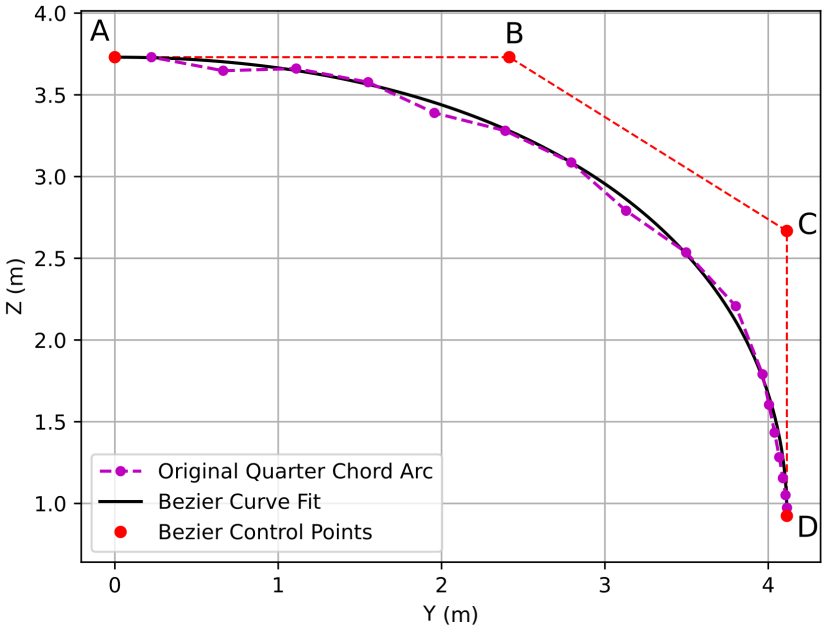

Figure 3.4: Front view of the quarter-chord arc of the TU Delft V3 kite with fitted Bézier curve and corresponding control points.

A Bézier curve, inspired by the airfoil parameterisation of Masure, has shown the greatest flexibility within a limited set of requirements. The curve as shown in Figure 3.4 was made

from four control points: the start and end of the curve, and two tension makers. The locations of the tension makers have been iterated to minimise the total distance from the original quarter-chord arc to the fitted Bézier curve. This is done using the minimisation algorithm in the Python-integrated package Scipy. Now, this curve is only determined using three parameters: the horizontal distance between the top two control points, the vertical distance between the two side control points, and the angle between the tip and the symmetry plane rib. Once the control points are found, the original LE coordinates are projected onto the Bézier curve, thereby translating the data back to the format used by simulation tools.

The kite design process currently applied at Kitepower, as introduced in Section 2.3, relies in part on expert knowledge. Building on this process and the kite parametrisation described above, an interview with a kite design expert was conducted to identify the design parameters with the largest influence on the performance of a LEI kite for AWESs. Based on the existing design process and the kite parametrisation described above, a reduced set of design variables was selected using expert input[1]. The resulting design vector is defined as

$$\mathbf{x}^{\mathrm{T}} = [AR,\ ab,\ cd,\ \Gamma,\ \kappa]\,. \tag{3.6}$$

The planform area is kept constant to enable a direct comparison of different geometrical configurations. The arc shape of the kite is parametrised using three variables: the horizontal distance between the control points A and B (ab); the vertical distance between the control points C and D (cd); and the anhedral angle Γ, defined as the angle between the symmetry chord and the wing tip (i.e. $\angle BAD$). The influence of these parameters on the arc geometry is described in detail in Section 4.2. Finally, including AR and κ are included as design variables. The procedure for incorporating the selected design parameters into the kite parametrisation and reshaping is presented in Chapter 4.

3.4. Detailed description of selected simulation tools

This section provides a concise description of the simulation tools used in the proposed toolchain. The tools are presented in the order in which they are applied, from geometric kite definition to aerodynamic, structural, and system-level performance analysis.

3.4.1. SurfPlan™ and SurfPlanAdapter

SurfPlan™ is a CAD tool developed for the geometric design of soft-wings, including surf kites, paragliders, and parachute canopies [51]. Within this work, SurfPlan is used to generate the three-dimensional geometry of the reference V3 kite. The software provides a consistent geometric description of the canopy and bridle layout and enables rapid future iteration of kite shapes.

The output of SurfPlan is processed using the SurfPlanAdapter, which converts the geometric data into a format suitable for aerodynamic and structural analysis in ASKITE. In addition, SurfPlanAdapter assigns two-dimensional aerodynamic characteristics to the spanwise airfoil sections of the kite. These aerodynamic polars can be obtained using different approaches, including empirical regression models, machine-learning-based surrogate models, precomputed CFD polars, or analytical inviscid theory.

Surrogate-based approaches include the regression model developed by Masure [34], which is trained on a large CFD-generated dataset of LEI kite airfoils, and the regression method proposed by Breukels [8]. Alternatively, NeuralFoil [49, 48] can be used to rapidly generate

[1]Tom Lollies (kite design expert for Kitepower B.V.), interview by author, May 22, 2025.

viscous airfoil polars using a machine-learning surrogate. For higher-fidelity input, externally generated CFD-based polars may be supplied directly. As a low-fidelity alternative, inviscid polars based on thin airfoil theory can be generated analytically [28].

Due to the short simulation time and CFD-based data, Masure's regression will be used to analyse the 2-dimensional aerodynamic performance of the airfoil shapes during optimisation. The airfoil shape parameters to define an LEI kite airfoil are flexible in application, but must adhere to the constraints given by Masure, listed in Table 3.1. In addition, the following criteria must be satisfied:

- The camber tension control point shall not be located too far aft: $\eta + \lambda < 0.8$.
- The camber height shall not be excessively large relative to the LE diameter: $\kappa \leq 2.5t$.
- When $\kappa < \frac{t}{2}$, the airfoil is considered flat.

Table 3.1: Airfoil shape parameter ranges by Masure [34].

Parameter	Range
t (−)	0.03 – 0.12
η (−)	0.08 – 0.40
κ (−)	0.04 – 0.16
δ (°)	-8 – 0
λ (−)	0.10 – 0.40
ϕ (−)	0.65 – 0.65
α (°)	-10 – 22
Re (−)	$1 \times 10^6 - 2 \times 10^7$

The resulting geometric and 2-dimensional aerodynamic data are stored in a structured format and passed to ASKITE for three-dimensional aero-structural analysis.

3.4.2. ASKITE

ASKITE is a simulation tool developed for the integrated aerodynamic and structural analysis of kite wings, with a specific focus on AWE applications [11]. Within the toolchain, ASKITE serves as the primary analysis tool for evaluating the three-dimensional aerodynamic performance and static aero-structural equilibrium of the scaled kite geometries.

The aerodynamic model implemented in ASKITE is based on the VSM. This method represents the aerodynamic effect of a finite wing using discrete bound vortices and trailing wake structures. The underlying concept of replacing a finite wing section by a horseshoe vortex is illustrated in Figure 3.5. Compared to classical lifting-line and vortex lattice formulations, the VSM implementation in ASKITE is tailored to handle the curved planforms and relatively low AR characteristic of LEI kites.

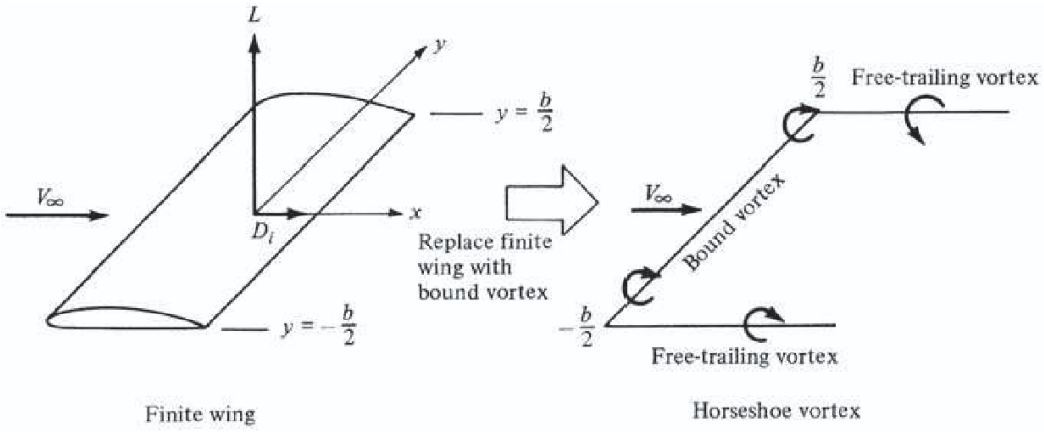

Figure 3.5: Replacement of a finite wing section with a horseshoe vortex [2].

The two-dimensional aerodynamic characteristics required by the VSM are provided as spanwise airfoil polars. These polars may originate from empirical regression models, machine-learning-based surrogate models, or externally generated CFD data, as described in the preceding section. Based on these inputs, ASKITE computes local aerodynamic forces and induced velocities along the kite span, resulting in a three-dimensional force distribution and wake geometry.

For each evaluated flight condition, the VSM provides the resulting aerodynamic coefficients, including the lift coefficient C_L, drag coefficient C_D, and side-force coefficient C_S, together with their spanwise distributions. In addition, the aerodynamic moment coefficients about the three body axes, $C_{m,x}$, $C_{m,y}$, and $C_{m,z}$, are obtained. These quantities are evaluated over a prescribed range of angles of attack and sideslip angles, enabling the construction of multidimensional aerodynamic polars for subsequent analysis and performance evaluation.

An example of the aerodynamic output of ASKITE is shown in Figure 3.6, where the aerodynamic force vectors and wake structure of the TU Delft V3 kite are visualised. Such results provide insight into lift distribution, induced effects, and overall aerodynamic loading, which are essential for comparative evaluation of kite geometries within the optimisation process.

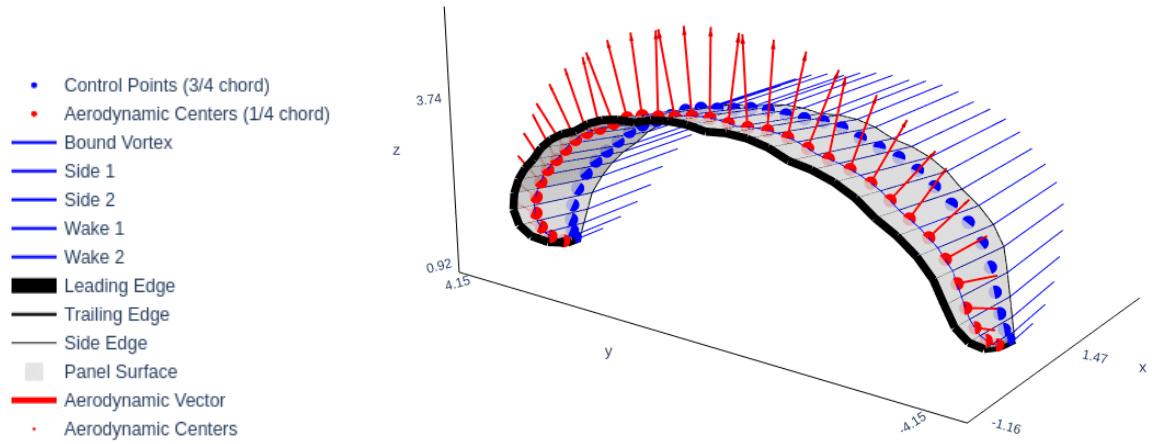

Figure 3.6: VSM results for the TU Delft V3 kite, including aerodynamic force vectors and wake geometry.

ASKITE couples the aerodynamic model to a particle-based structural representation of the kite. The canopy, bridle, and kite control unit are modelled as discrete points connected through spring-damper elements with prescribed stiffness values. This representation captures the dominant deformation modes of the flexible kite structure while remaining computationally efficient. The structural model used for the TU Delft V3 kite is shown in Figure 3.7.

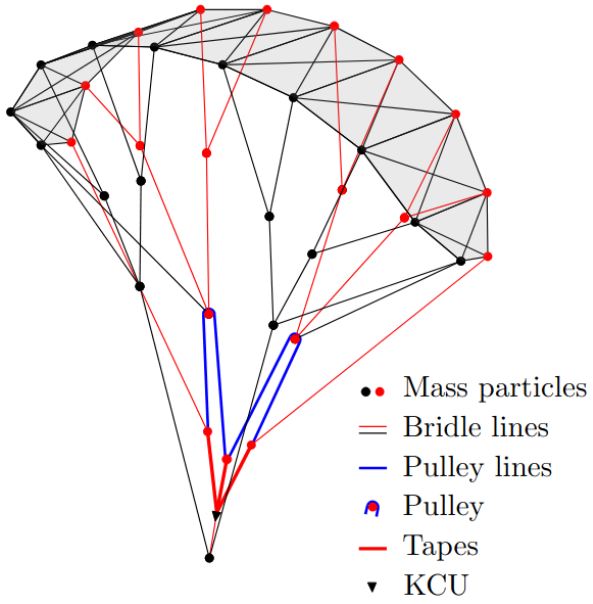

Figure 3.7: Particle-based structural representation of the TU Delft V3 kite [42].

Aerodynamic forces computed by the VSM are applied to the structural model, resulting in a deformed kite geometry. The updated geometry is subsequently re-evaluated aerodynamically, and the procedure is repeated until a trimmed, quasi-steady equilibrium state is reached. This aero-structural coupling captures first-order deformation effects and load redistribution under aerodynamic loading, which are relevant for a realistic assessment of kite performance.

Due to its quasi-steady formulation and inviscid aerodynamic assumptions, ASKITE is primarily suited for early-stage design studies and shape optimisation, rather than for high-fidelity prediction of unsteady or post-stall behaviour.

In the context of this thesis, ASKITE provides the essential link between parametric kite geometry generation and system-level performance evaluation. Its balance between physical modelling detail and computational efficiency enables repeated evaluation of candidate kite shapes within an optimisation-oriented toolchain.

3.4.3. Luchsinger's model

The AWES performance estimator proposed by Luchsinger is based on a simplified analytical model [32]. The model builds on the idealised crosswind power laws originally formulated by Loyd [31] and evaluates the performance of a kite with prescribed aerodynamic lift and drag coefficients during the reel-out (powered) and reel-in (depowered) phases of the pumping cycle. The output is, among other results, the power curve of an AWES.

In this formulation, the kite flight path is idealised as a straight trajectory during both reel-out and reel-in, as illustrated with the dashed line in Figure 3.8. The model assumes constant aerodynamic coefficients and represents the turning behaviour of the kite using average

azimuth and elevation angles, thereby reducing the flight dynamics to a steady crosswind representation. This level of abstraction enables rapid estimation of cycle-averaged power output while neglecting unsteady and dynamic effects.

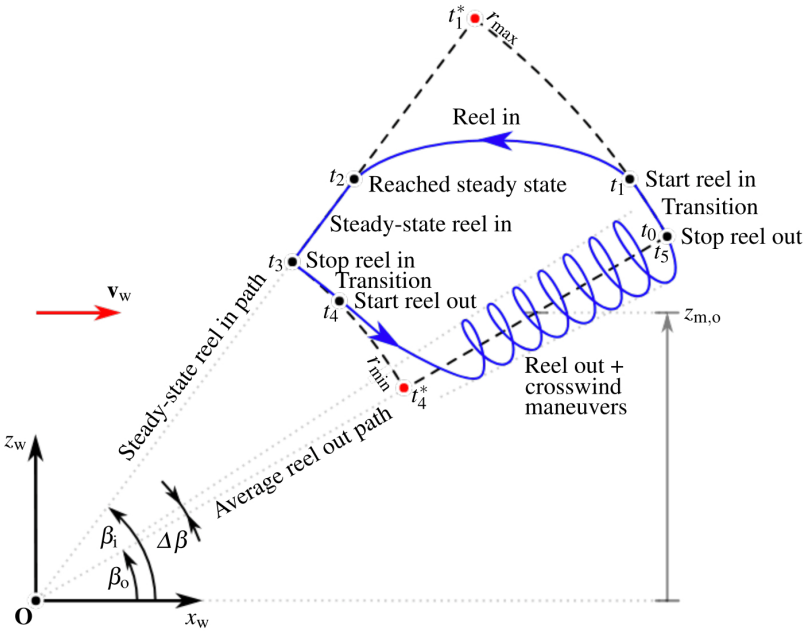

Figure 3.8: Side view of a measured kite flight path (blue) and the idealised flight path used in Luchsinger's model (dashed) [46].

The implementation used in this research is based on the initial numerical realisation developed by Corte Vargas et al. [53] under the supervision of Schmehl and subsequently adapted by Velasco. Additional constraints are described in Section 5.3.

3.4.4. AWETrim

AWETrim is a quasi-steady system-level simulation tool used to estimate the performance of pumping-cycle AWESs [10]. Here, quasi-steady refers to the computation of a trimmed state resulting from the balance of all forces and moments acting on the system. The kite is modelled as a point mass, while translational accelerations and inertial effects are included. At each time step, a trimmed flight state is determined from the kite's aerodynamic polar data.

The reel-out phase of the pumping cycle is optimised with respect to reel-out speed and flight-path parameters, including path width, height, and additional parameters that define the exact trajectory. Different flight path expansion strategies can be evaluated, such as radially expanding or parallel trajectories, as illustrated in Figure 3.9. Using a prescribed wind profile and hardware configuration, AWETrim computes the cycle-averaged power output, enabling consistent comparisons across different kite designs. This analysis can be performed for different wind speeds, which can then be collected into a power curve.

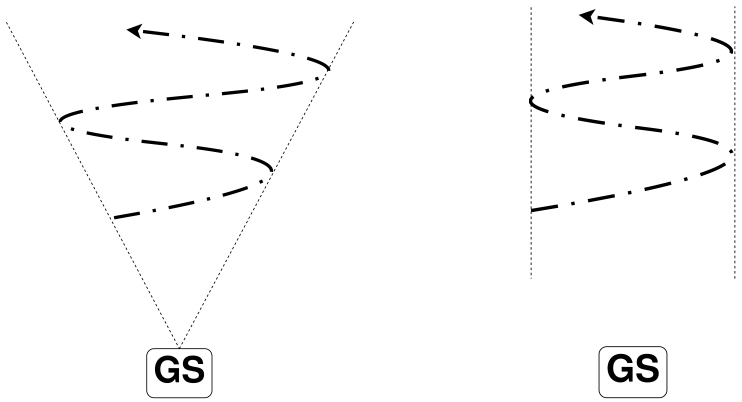

(a) Radially expanding flight path. **(b)** Parallel flight path.

Figure 3.9: Schematic flight path options for QSM: radially expanding (a) and parallel (b).

3.4.5. Dynamic three-dimensional system model

A high-fidelity dynamic simulation model developed by Fechner [17] serves as a reference for the full dynamic simulation (FDS). The model simulates a complete pumping-cycle operation of a ground-based AWES, including the kite, tether, winch, control system, and environmental conditions.

The kite is represented using a four-point particle model, as shown in Figure 3.10. This model is selected because it is the simplest way to represent a point-mass system with rotational inertia in all directions, thereby providing a realistic dynamic response and avoiding non-physical behaviour that can negatively affect controllability. The kite mass is distributed among four virtual points. The tether is modelled as a segmented tether, represented by a fixed number of lumped masses connected by spring-damper elements. This representation captures essential phenomena, such as tether drag and sag, required for accurate prediction of tether forces and for controller development. The full system dynamics are formulated as an implicit differential algebraic system.

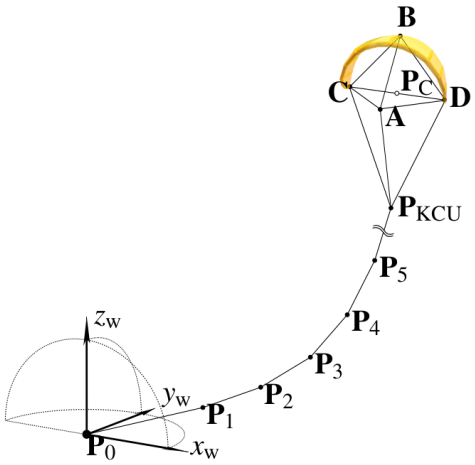

Figure 3.10: The four-point kite model defined by points A, B, C and D.

Aerodynamic forces (lift and drag) are calculated using lookup tables representative of the reference LEI kite. Steering is controlled by a turn-rate law, in which steering inputs are numerically matched to induce differential angles of attack on the kite surfaces, generating

the required turning moments. Environmental effects include wind shear and turbulent wind fields.

The dynamic model is governed by an advanced control architecture that enforces operational and structural constraints while maximising energy extraction. The physical and operational constraints applied in the simulations are summarised as follows:

- **Nominal generator power:** The model represents an up-scaled version of a demonstrator designed for a 20 kW nominal generator power.
- **Maximum tether force:** A hard structural limit for the tether force was set to 8000 N. The control system ensures this limit is not exceeded, particularly under turbulent conditions.
- **Operational envelope:** The maximum height allowed for power generation is constrained to 600 m.
- **Aerodynamic constraints:** The angle of attack is maintained between 0° and 20° to avoid aerodynamic buckling (below 0°) and stalling (above 20°).
- **Peak power limitation:** To protect the electrical system, peak mechanical power input to the generator is actively limited in the simulations, typically capped below 30 kW.

Although computationally expensive, this model provides a detailed benchmark for assessing the validity and limitations of the lower-fidelity tools used within the optimisation-oriented toolchain. Furthermore, the model can be used to generate a power curve that is specific to the considered AWES.

3.5. Objective function

The performance modelling described in the previous sections provides an instantaneous representation of the system's power output as a power curve. However, the optimal shape of this power curve is not immediately evident, as the overall performance of an AWES depends on the varying wind conditions encountered in real operating environments. Therefore, a performance metric is required that captures system behaviour across a range of wind speeds and reflects realistic operating conditions. For this purpose, the AEP is used, representing the total electrical energy generated by the system over a year at a specific location, accounting for the statistical distribution of wind speeds.

To translate the aerodynamic and structural performance of the AWES into AEP, a flight-scheduling algorithm is employed. The power curve obtained from the full dynamic simulation described in Section 3.4.5 is used as input, thereby incorporating realistic flight dynamics, control behaviour, and operational limits. By combining this power representation with time-resolved wind speed data, the scheduler simulates operational decisions over extended periods and enables the estimation of energy production under realistic conditions.

The scheduling logic is implemented as a finite-state machine (FSM) that evaluates system availability and environmental conditions hourly. The FSM cycles through six operational states: IDLE, ANALYZE, PLAN, WAIT_REFRESH, FLYING, and COOLDOWN. This structure enables the algorithm to capture temporal coupling between consecutive flights and enforce operational constraints, such as launch windows, minimum flight durations, and mandatory downtime. The following operational constraints are implemented in the FSM:

- **Wind envelope**: Flight is only permitted when $v_{\text{cut-in}} \leq v_w \leq v_{\text{cut-out}}$ (e.g., $5.5 \leq v_w \leq 15$ m/s).
- **Minimum flight duration**: $T_{\text{flight}} \geq T_{\text{min}}$.

- **Maximum flight duration**: $T_{\text{flight}} \leq T_{\max}$.
- **Launch window**: Launches are restricted to specified hours (e.g. 08:00–20:00).
- **No-fly window**: Flight is prohibited during specified hours (e.g. 00:00–06:00).
- **No-fly days**: Optional restriction on specific days of the week.
- **Downtime**: A mandatory turnaround time T_{down} is enforced between consecutive flights.

At each step, the algorithm looks ahead over a 72-hour forecast window. For each potential start hour i within this window, the maximum continuous flight duration L_i is determined as the longest sequence of consecutive hours for which all operational constraints are satisfied. The associated energy production for this specific flight is estimated using the power curve derived from the full dynamic simulation as

$$E_i = \sum_{k=i}^{i+L_i-1} P_{\text{AC}}(v_{w,k})\,\Delta t - E_{\text{packing}},$$

where $\Delta t = 1$ hour is the time step and E_{packing} represents the energy consumed during system setup and packing operations.

All flight candidates are ranked in descending order of estimated energy yield, with ties resolved by selecting the earliest feasible start time. The algorithm schedules the highest-ranking candidate as the primary flight and subsequently attempts to insert additional pre-flights, provided they are completed before the primary flight and satisfy the minimum downtime requirement between consecutive flights.

As a result of this flight-scheduling algorithm, the power produced at each hour is assessed over a specified period. Summing all hourly energy ratings yields the AEP, which the optimiser will use as the optimisation objective. An example of the hourly energy ratings for one month is given in Figure 3.11.

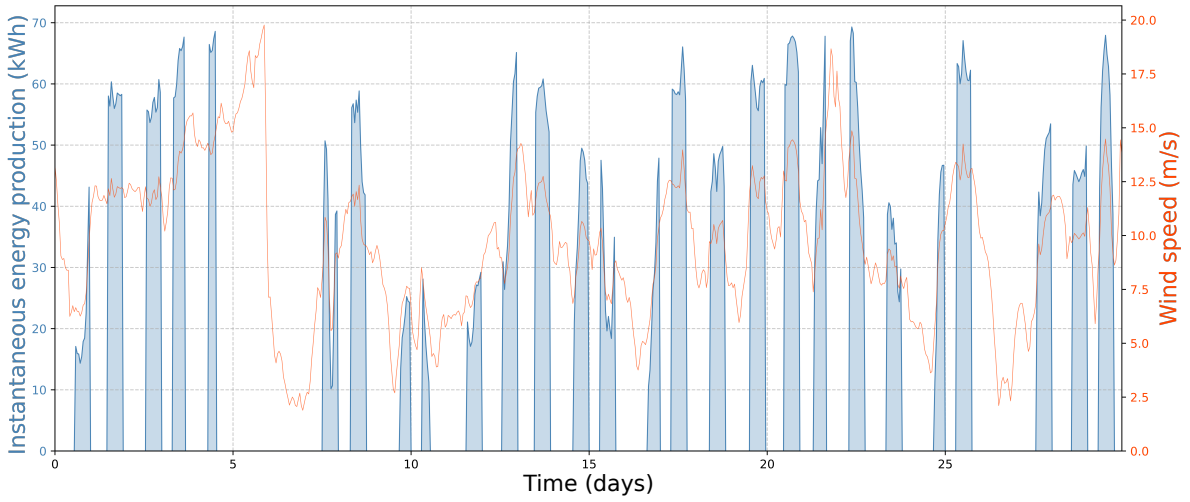

Figure 3.11: Energy log used for AEP calculation. The hourly nominal wind speed is given (orange), to which the instantaneous power production is determined (blue).

4

Kite parametrisation and reshaping

This chapter presents the methodology and corresponding calculations used to parametrise and reshape kite geometry. Each design parameter (AR, arc shape, and camber height) is addressed in a separate section. First, the parametrisation and scaling of the AR are presented in Section 4.1, followed by the method for reshaping the arc in Section 4.2. Subsequently, the airfoil reshaping procedure is described in Section 4.3. Finally, an illustrative example of the complete geometric reshaping process is provided in Section 4.4.

4.1. Aspect ratio parametrisation and scaling

The AR of the kite wing depends on both the wing span and the wing area. For a LEI kite, the span and area can be defined in two different ways: the *flattened* geometry and the *projected* geometry. The flattened geometry corresponds to the kite being deflated and fully stretched out, removing the wing's anhedral. The projected geometry, on the other hand, represents the visible planform area of the inflated kite in a top- or bottom-view. Since a flatter kite produces a larger projected area for the same flattened area, the ratio between the projected and flattened spans depends strongly on the arc shape. As the arc shape is treated as an independent design variable in this optimisation, all AR calculations are based on the flattened geometry. Flattened quantities are therefore indicated with the subscript f.

First, the reference kite surface area is obtained by discretising the wing into trapezoidal sections and summing their areas. An example of such a discretisation is shown in Figure 4.1. The surface area is computed as

$$S = \sum_{i=0}^{n} S_{\text{section},i} = \sum_{i=0}^{n} \frac{1}{2} \left(c_i + c_{i+1}\right) b_{i,i+1}, \tag{4.1}$$

where c_i is the chord length of the i-th rib section, $b_{i,i+1}$ is the spanwise distance between adjacent ribs, and n is the number of sections.

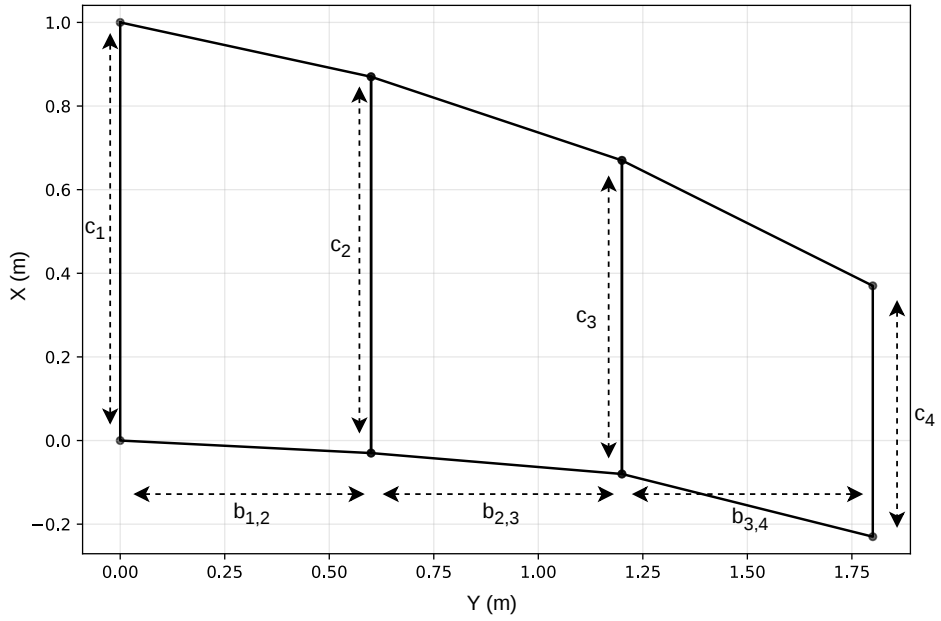

Figure 4.1: Example of a segmented wing planform for dimensional reshaping.

Once the reference span and surface area are determined, the reference AR can be calculated using Equation (3.2). In the optimisation, a new target AR ($AR_{f,\text{new}}$) is provided as an input. To obtain the corresponding flattened span, the relation between AR, span and area in Equation (3.2) is rewritten assuming constant wing area:

$$\frac{b_{f,\text{new}}}{b_{f,\text{old}}} = \sqrt{\frac{AR_{f,\text{new}}}{AR_{f,\text{old}}}}, \tag{4.2}$$

rewriting to:

$$b_{f,\text{new}} = b_{f,\text{old}} \sqrt{\frac{AR_{f,\text{new}}}{AR_{f,\text{old}}}}. \tag{4.3}$$

The chord lengths must then be scaled to preserve the wing area. Using Equation (3.4) and 4.3, the ratio between the new and reference SMC can be written as:

$$\frac{SMC_{\text{new}}}{SMC_{\text{old}}} = \frac{b_{f,\text{new}}}{b_{f,\text{old}}} \frac{AR_{\text{old}}}{AR_{\text{new}}}, \tag{4.4}$$

which is used as the scaling factor for the chord length of each rib.

4.2. Arc parametrisation and reshaping

The Bézier curve shown in Figure 3.4 provides a suitable starting point for the arc-shape parametrisation in this toolchain. To enable comparison between different kite geometries, the

arc shape is normalised with respect to the half-span. The normalised arc and the corresponding control point placement are illustrated in Figure 4.2.

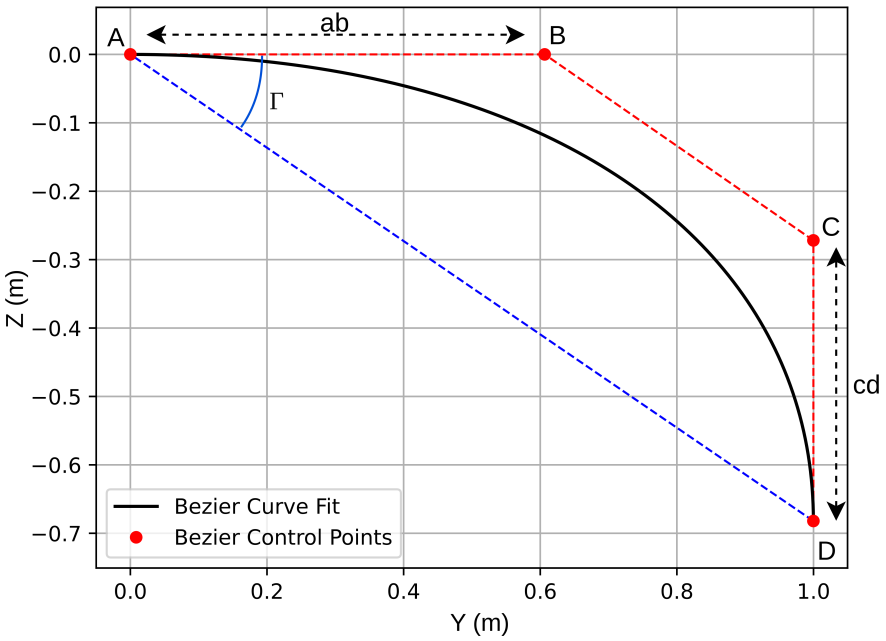

Figure 4.2: Kite arc-shape parametrisation.

With this parametrisation, the number of design variables is reduced to three: the lengths ab and cd, and the angle Γ. Given the flattened span (and thus the arc length), these three parameters are sufficient to fully define the arc. The individual influence of ab, cd and Γ on the arc shape is presented in Figure 4.3. Here, the effect of enforcing a constant arc length is clearly visible in the changes of cd and ab: the tip's y-coordinate decreases for a more curved arc (red) and increases for a flatter arc (blue).

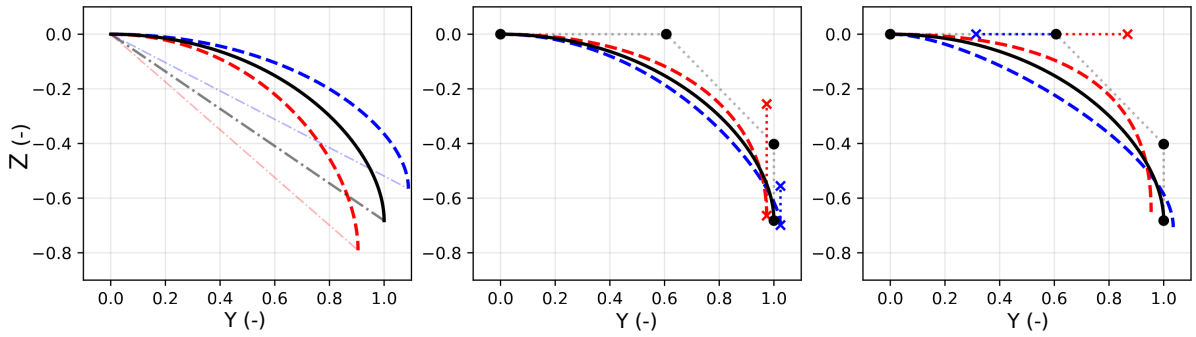

Figure 4.3: Effects on the span-normalised projected arc shape with scaled parameters Γ (left), cd (middle), and ab (right).

4.3. Airfoil parametrisation and reshaping

The airfoil geometry is defined by a set of parameters, including camber height and LE diameter, as introduced in Section 2.2. Since camber height is included in the optimisation design vector, the procedure for updating this parameter is described in Section 4.3.1.

All airfoil shape parameters are normalised with respect to the chord length. Because the AR and thus the chord length are varied during optimisation, the absolute LE thickness would also change. To maintain consistent structural integrity, the LE diameter is therefore kept constant. The applied scaling method is explained in Section 4.3.2.

4.3.1. Camber scaling

The camber of the kite is parametrised at the airfoil level. In the airfoil parametrisation presented in Section 2.2, the camber height is parametrised by κ. The camber distribution along the wingspan of the TU Delft V3 kite is shown in Figure 4.4.

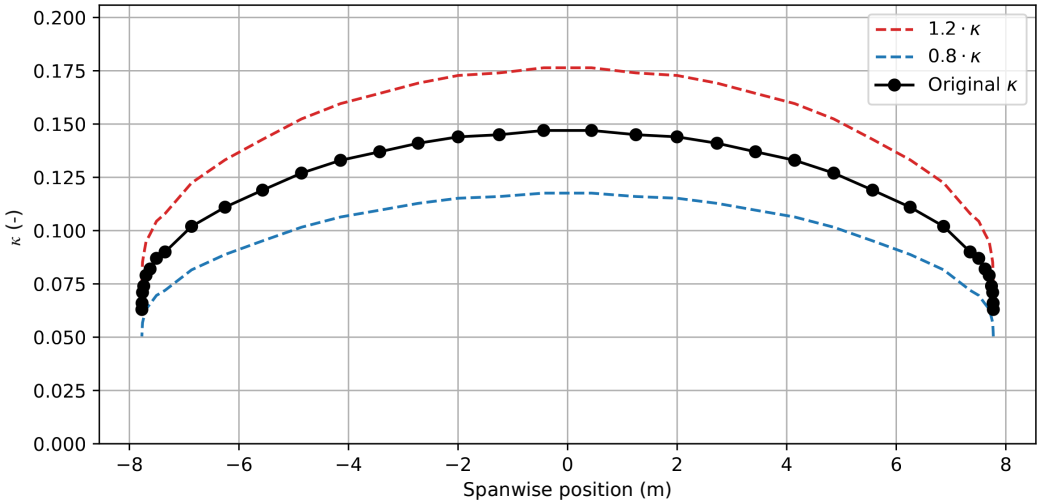

Figure 4.4: Camber height parameter κ along the flattened spanwise position of the TU Delft V3 kite.

A fully flexible parametrisation of the camber distribution could be defined using multiple variables, similar to the arc shape. However, this would increase the number of optimisation variables and could lead to unrealistic or unstable kite configurations. Therefore, the optimisation only scales the existing camber distribution while maintaining its relative shape. The camber height of each airfoil section is updated using a single scaling factor:

$$\kappa_{i,\text{new}} = x_\kappa \cdot \kappa_{i,\text{old}}, \tag{4.5}$$

where $\kappa_{i,\text{new}}$ is the updated camber height for airfoil section i, $\kappa_{i,\text{old}}$ is the corresponding value for the baseline kite, and x_{kappa} is the optimisation variable that scales the camber distribution. The effect of this scaling is illustrated in Figure 4.4 for scaling factors of 0.8 and 1.2. A cross-sectional view of a reference airfoil with scaled κ is shown in Figure 4.5.

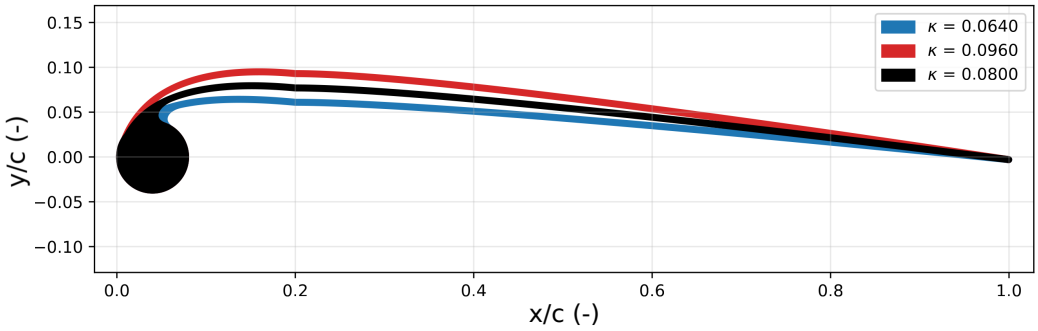

Figure 4.5: Airfoil geometry with scaled camber parameter κ ($x_\kappa = 0.8$ (blue), $x_\kappa = 1.2$ (red), $x_\kappa = 1.0$ (black), with fixed profile parameters: $t = 0.08$, $\eta = 0.2$, $\delta = 0°$, $\lambda = 0.2$, $\phi = 0.65$.

4.3.2. Leading-edge diameter scaling

Since the airfoil shape parameters are normalised with respect to the chord length, their absolute values change when the chord length is scaled, for example, when varying the AR. Increasing the AR results in a shorter chord length, which would consequently reduce the absolute LE diameter if the airfoil parameters were kept unchanged. From a structural perspective, however, the LE diameter should not decrease for higher-span wings associated with higher AR values.

To prevent this effect, the chord scaling factor is applied inversely to the LE thickness parameter t. In this way, the absolute LE diameter is preserved when the planform geometry is modified. The relationship between the scaled and reference airfoil thickness parameters is given by

$$t_{\text{new}} = t_{\text{ref}} \frac{c_{\text{ref}}}{c_{\text{new}}}, \tag{4.6}$$

where the subscript ref denotes the reference kite configuration and c represents the local chord length. A limitation of this scaling approach arises when the resulting t_{new} exceeds the admissible bounds for the airfoil shape parameters defined by Masure's parametrisation, as listed in Table 3.1. In such cases, the thickness parameter is limited to the nearest bound to ensure compliance with the validated airfoil design space.

4.4. Geometric reshaping example

This section presents an example of the geometric scaling procedure applied to the kite geometry. The scaling is performed after the pre-processing stage, i.e. when the kite has already been described in 3D coordinate space as in the standard toolchain. For demonstration purposes, the AR is increased from approximately 5 to 8.5, while all other design parameters are kept constant.

The scaling process is divided into five sequential steps, which are visualised in Figure 4.6 to 4.10. In each figure, the left panel shows an isometric view of the kite geometry in 3D space, while the right panel shows a centreline view. The quarter-chord arc is used to define the locations of the new airfoil sections, as described in Section 4.2. Consequently, the x-coordinate of the quarter-chord arc is copied from the reference kite, which is also visible in the centreline views.

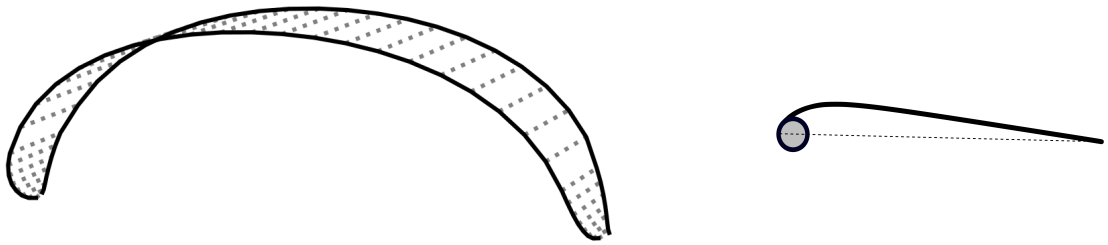

Figure 4.6: Scaling step 1: Definition of the reference kite geometry and baseline planform used for scaling.

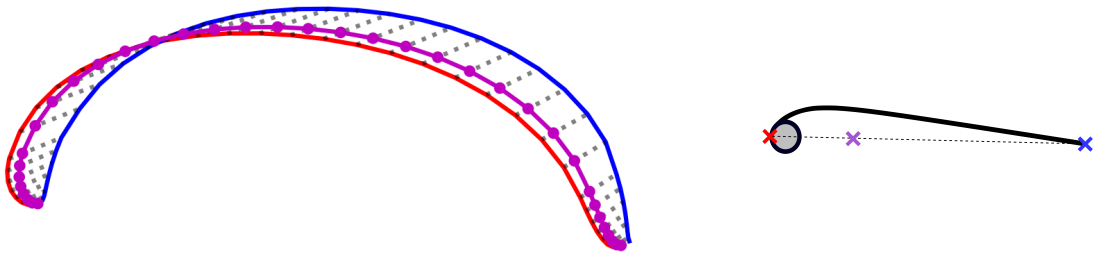

Figure 4.7: Scaling step 2: Identification of leading- and trailing-edge, and corresponding quarter-chord arc of the reference geometry.

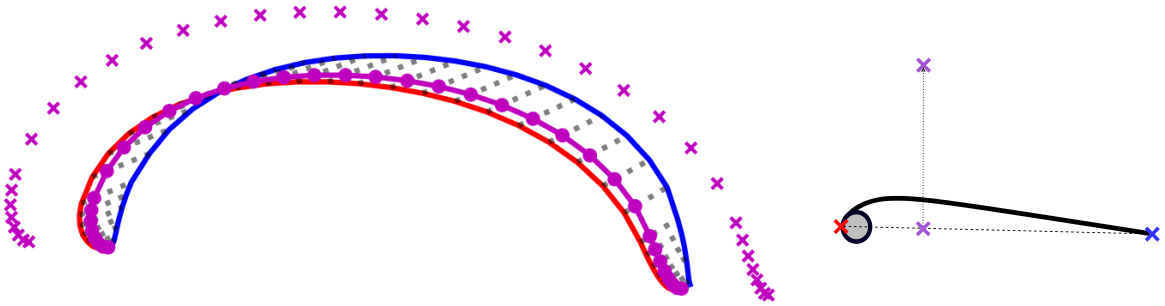

Figure 4.8: Scaling step 3: Construction of the scaled quarter-chord arc with updated curvature and span, while enforcing the reference tip z-coordinate. Additional effects of the arc-shape parametrisation are applied at this stage.

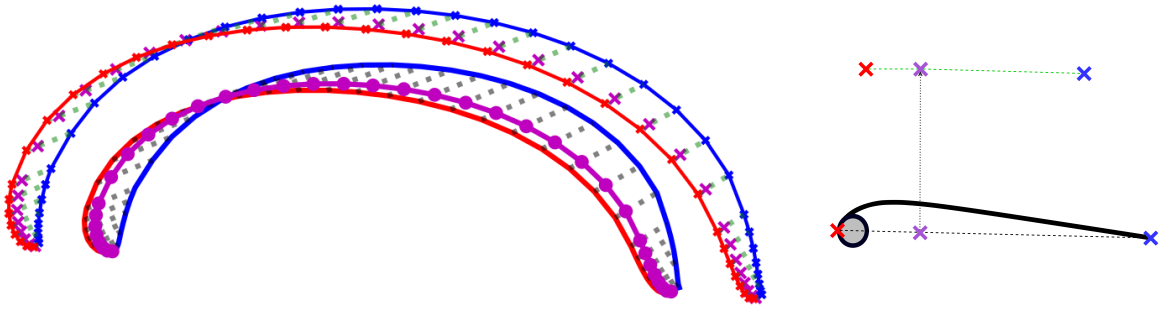

Figure 4.9: Scaling step 4: Placement of the leading- and trailing-edges along the updated quarter-chord arc using the scaled chord lengths.

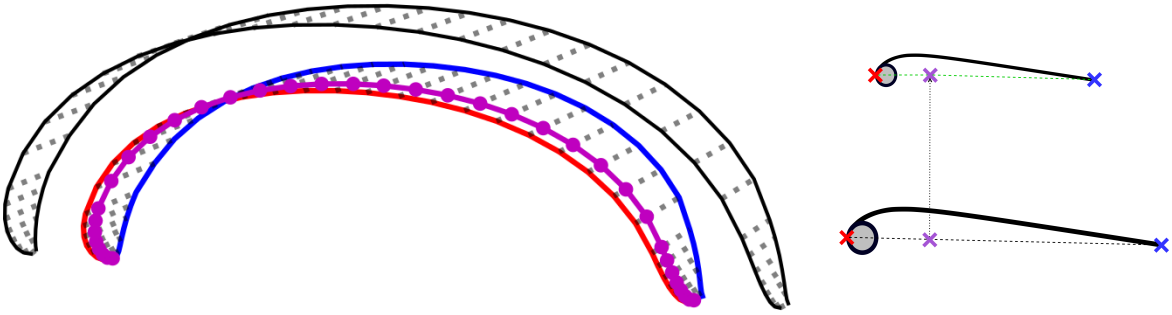

Figure 4.10: Scaling step 5: Placement of the airfoil sections at the updated locations, with the camber parameter κ scaled accordingly.

In addition to the wing geometry, the bridle line setup is updated to match the new spatial configuration and account for the resulting change in bridle drag. Since the tip z-coordinate is preserved throughout the geometrical optimisation, the bridle nodes (highlighted in red in Figure 4.11) are linearly scaled from this point. In Figure 4.11, this point is indicated with a "+" marker, and in the right figure, the new location of all bridle nodes and lines with respect to the original geometry is shown.

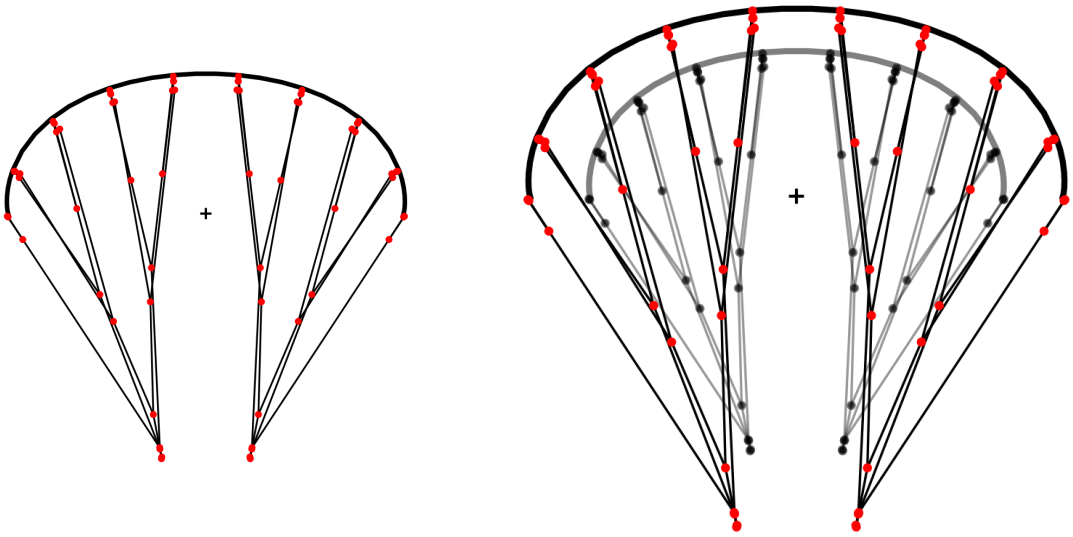

(a) Reference kite bridle setup.

(b) Scaled kite bridle setup.

Figure 4.11: Effect of AR scaling on the bridle setup: nodes are translated from the tip z-coordinate (marked with the "+").

5

Simulation framework

This chapter presents the multidisciplinary simulation framework developed for geometrical kite optimisation (GeKO) for AWESs. The chapter first introduces the conceptual design framework in Section 5.1, describing the intended coupling between the different disciplines and outlining potential extensions. The implemented toolchain is presented in Section 5.2, including the selected models, the data flow, and the key assumptions. For both the conceptual and implemented frameworks, flowcharts and XDSM diagrams are provided and discussed. In Section 5.3, operational constraints applied to the toolchain are discussed. Finally, candidate optimisation algorithms are proposed in Section 5.4.

5.1. Conceptual design framework

The primary objective of the proposed framework was to evaluate and optimise kite geometries based on their AEP. Starting from an initial geometric definition of the kite, a sequence of aerodynamic, structural, and performance analyses is required to assess power production under realistic wind conditions. By working backwards from this overall objective, the required intermediate quantities can be identified, allowing the individual models and tools to be arranged in a logical and consistent order within the framework.

5.1.1. Intended discipline coupling

The conceptual framework couples the key disciplines required for the design and optimisation of AWESs. A kite geometry serves as the primary design input and the baseline and objective for this toolchain. Structural modelling is required to assess feasibility and to provide mass and stiffness properties for the performance models. At the system level, performance is evaluated using power production models that account for operational constraints and environmental conditions. The overall sequence of analyses in the conceptual framework is illustrated in the flowchart shown in Figure 5.1. The corresponding XDSM representation is provided in Appendix B. The chosen system architecture for this XDSM is a hybrid between IDF and MDF, with consistency constraints included alongside the objective function (IDF) and execution-order dependence (MDF).

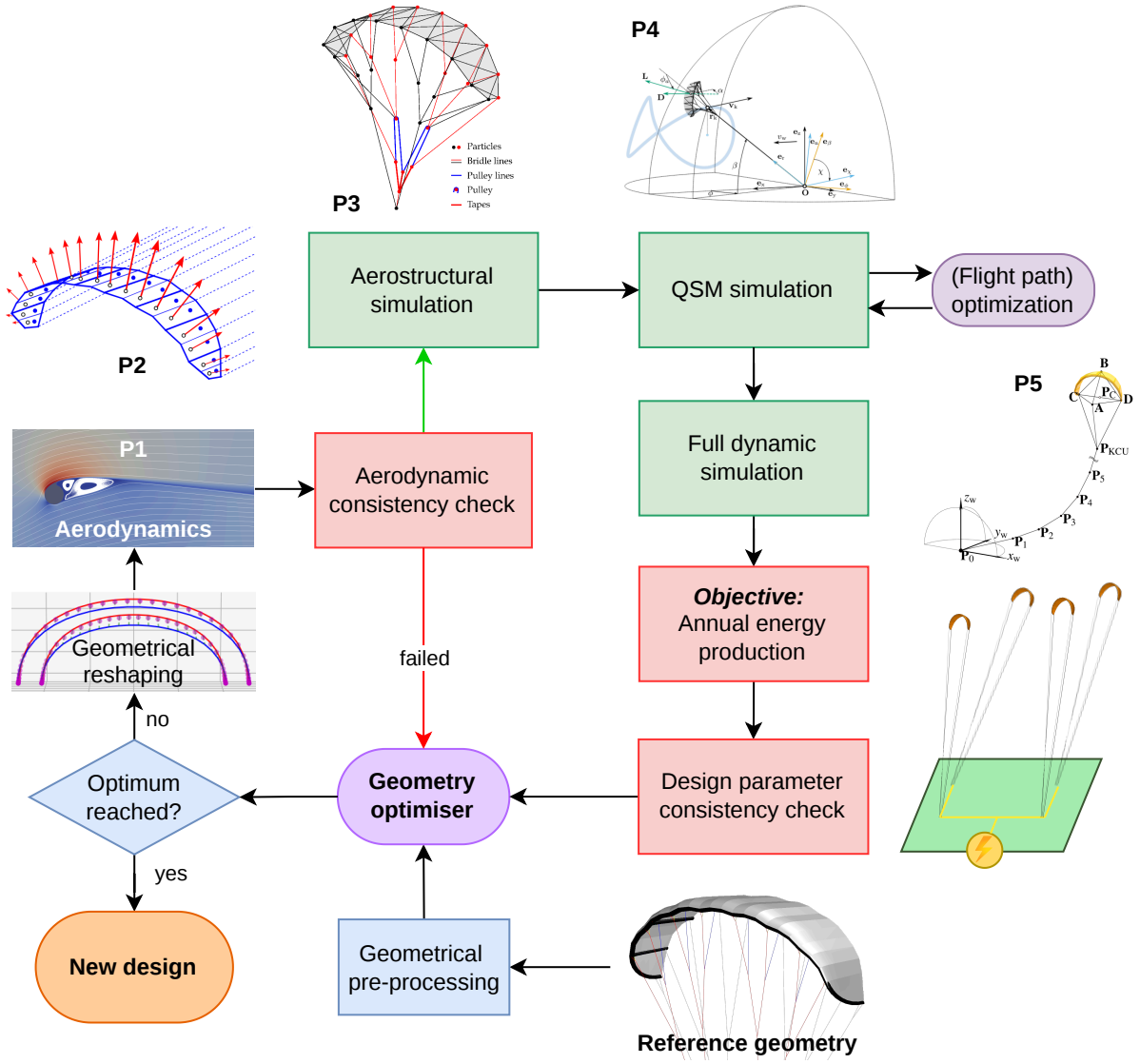

Figure 5.1: Flowchart of the conceptual GeKO framework.
P1: [34], P2: [41], P3: [42], P4: [10], P5: [17]

The toolchain takes a reference kite geometry as its initial input, which serves as the starting point for the optimisation. After the geometrical pre-processing described in Section 3.3.2, the kite geometry enters the optimisation loop as the initial design vector. Following parameter updates by the optimisation algorithm, the geometry is reshaped according to the procedures outlined in Chapter 4. An aerodynamic analysis is then performed at both the two- and three-dimensional levels using the VSM, as described in Section 3.4.2.

To limit computational cost, designs that are clearly infeasible are filtered out before executing the more expensive performance simulations. This is achieved through an aerodynamic consistency check, which evaluates several feasibility criteria. Examples include monitoring lift and drag coefficients, feasible angle of attack (AOA) and sideslip angle ranges, lift and mass balance conditions, stability requirements, or other physical constraints to prevent convergence toward numerically optimal but physically unrealistic solutions.

If the aerodynamic consistency check is satisfied, a structural analysis is carried out to compute kite deformations under representative operational conditions. The resulting deformed

geometry defines an updated aerodynamic shape, introducing a feedback loop between the aerodynamic and structural models. This coupled aero-structural analysis is performed using ASKITE, as described in Section 3.4.2. Once a consistent aerodynamic and structural representation of the kite is obtained, system-level performance calculations are conducted.

Performance modelling is performed in two stages: a QSM and a FDS. As the operational behaviour of a newly designed kite is generally unknown, AWETrim is used to optimise the operational parameters and determine a feasible flight trajectory, as described in Section 3.4.4. This trajectory serves as input for the full dynamic simulation, which provides a high-fidelity estimate of system performance at a given wind speed, as detailed in Section 3.4.5. By repeating the QSM and FDS analyses over a range of wind speeds, a complete power curve is obtained.

The power curve is a key performance metric for an AWES and is used to compute the AEP. A flight scheduling algorithm is applied using statistical wind data to represent the wind speed distribution at a specific geographic location over an entire year. Combining this wind data with the system power curve enables estimation of the AEP, as described in Section 3.5. This approach enables the optimisation of kite geometries for site-specific wind conditions and can be extended to account for multiple AWESs operating at the same location, subject to operational constraints.

5.1.2. Extensions for conceptual framework

Although the conceptual framework supports the inclusion of high-fidelity aerodynamic, structural, and dynamic models, their practical application is constrained by computational cost. Potential extensions include fully coupled aeroelastic simulations, higher-resolution atmospheric modelling, and advanced optimal control formulations.

In addition to performance-oriented extensions, the framework could be expanded to include a life-cycle analysis to assess the environmental impact of airborne wind energy systems. This analysis could either be incorporated directly into the optimisation as an additional objective or constraint, or applied as a post-processing step to evaluate the environmental performance of the optimised designs. Given the reduced material use and installation requirements of AWESs, substantial environmental benefits are expected compared to conventional wind turbines.

Furthermore, a cost-estimation model covering the development, production, and testing phases could be integrated into the framework to link technical performance to economic viability. For the commercial deployment of AWESs, a trade-off between AEP and overall system cost is essential, as designs with higher energy yield may not be economically justified if associated costs increase disproportionately. While integrating such a cost model would be of significant commercial relevance, its implementation would require further research and detailed cost data. For rigid-wing kites, a cost estimation tool has been developed by Joshi [26]. A similar approach would be required to develop a corresponding tool for soft-wing kites.

5.2. Implemented toolchain

Based on the conceptual framework, a practical and computationally feasible toolchain has been implemented. The primary objective of this implementation is to enable systematic evaluation of kite geometries while maintaining acceptable runtimes for iterative design optimisation. Several features of the conceptual framework fall outside the scope of this thesis; therefore, the implemented framework was developed as a minimum viable product that can be extended in future work. The toolchain evaluates kite geometries from their CAD-based definition through AEP, including geometry preprocessing, aerodynamic data generation, and performance modelling.

The implemented coupling strategy closely follows the conceptual discipline coupling described in Section 5.1.1. A simplified version of the toolchain is shown in Figure 5.2, with three key modifications relative to the conceptual framework. First, the number of internal consistency checks is reduced. Although design constraints remain enforced, the absence of early feasibility filters may increase runtime for certain design iterations. This increase, however, is expected to be partially offset by the omission of structural modelling and the reduced complexity of the performance modelling stage.

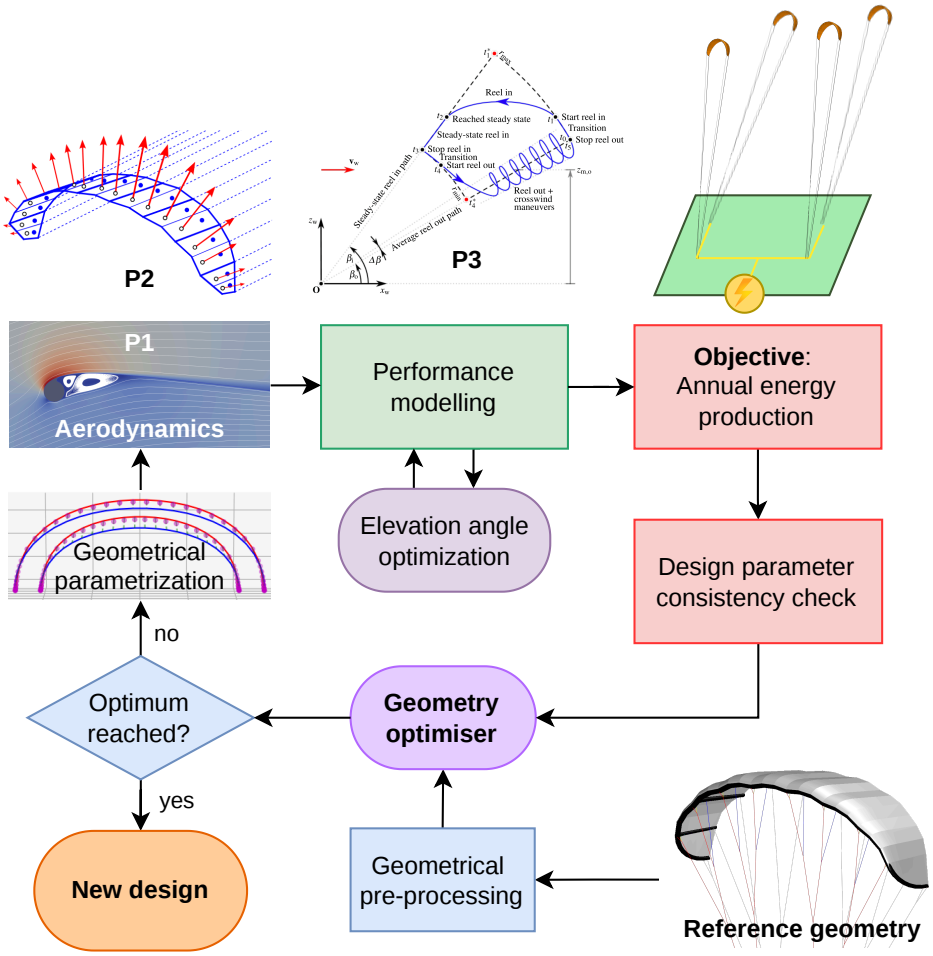

Figure 5.2: Flowchart of the implemented GeKO framework.
P1: [34], P2: [41], P3: [46]

All dependencies within the implemented toolchain are summarised in the XDSM shown in Figure 5.3. This diagram represents the actual data flow between the individual tools, distinguishing between primary analysis steps and validation or post-processing models. Two nested loops can be identified: an inner analysis loop that couples the simulation tools, and an outer optimisation loop that links the toolchain to the objective function and the design constraints. The system architecture for the implemented framework described in this XDSM is a hybrid between IDF and MDF, with design constraints imposed in addition to the objective function (IDF) and including execution-order dependence (MDF), as shown by the black line.

The data flow through the toolchain is predominantly sequential, with the V3 kite geometry serving as the initial input. Geometry pre-processing is performed using *SurfplanAdapter*, enabling consistent data handling throughout the framework, as described in Section 3.4.1.

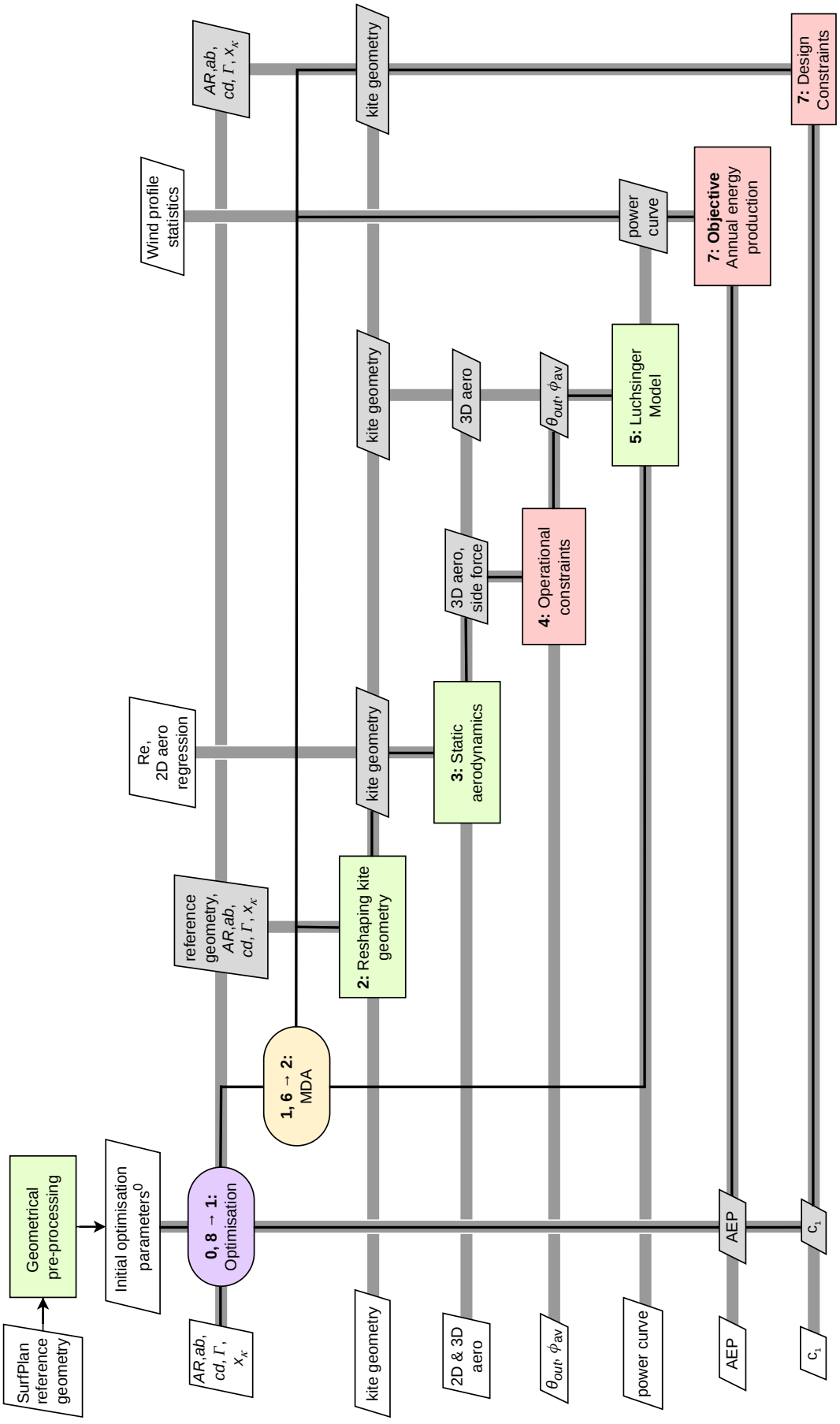

Figure 5.3: XDSM of the implemented GeKO Toolchain. Blocks represent simulations, modelling, and objective disciplines, and the black line indicates the execution order.

The geometric reshaping method, detailed in Chapter 4, requires only the reference geometry and the updated design vector as input and produces a reshaped kite geometry.

The reshaped geometry is subsequently used for aerodynamic analysis. First, a two-dimensional airfoil analysis is performed using Masure's regression model to generate sectional aerodynamic data. This is followed by a three-dimensional aerodynamic simulation using the VSM, after which finite-wing effects are incorporated into the resulting aerodynamic polars. Based on these polars and the associated turn rate, the reel-out elevation angle is determined as an operational constraint, as explained in Section 5.3.

Performance modelling is carried out using the Luchsinger model, described in Section 3.4.3, with modelling settings provided in Table C.1. The resulting power curve is then combined with site-specific wind statistics to compute the AEP, as described in Section 3.5.

5.3. Operational conditions

Within the implemented framework, several operational conditions must be specified to initialise the performance analysis and address limitations inherent to the simplified modelling approach. The optimisation relies on the Luchsinger model, which reduces the kite's aerodynamic behaviour to two states: a powered and a depowered configuration. To determine the aerodynamic performance for these states, the corresponding trim conditions are computed. This trim state defines the equilibrium flight condition and the associated aerodynamic coefficients used in the performance model, and is described in Section 5.3.1.

Furthermore, the reel-out phase in the Luchsinger model is represented as straight-line motion, thereby neglecting the kite's turning behaviour during crosswind flight. Without accounting for turning dynamics, the model tends to favour kite designs with excessively large projected areas, as these maximise tether force while disregarding manoeuvrability and flight feasibility. Since no structural model is included in the framework, such trends are not naturally penalised within the optimisation process.

To mitigate this limitation, additional geometry-dependent operational constraints are introduced by estimating the turning radius. The turning radius provides a simplified representation of the kite's manoeuvrability and is described in Section 5.3.2. This quantity is subsequently linked to the average elevation and azimuth angles of the flight trajectory, which define the kite's representative position within the wind window and are discussed in Section 5.3.3.

5.3.1. Trim state computation

Within the Luchsinger model, introduced in Section 3.4.3, the aerodynamic performance of the kite is represented by two characteristic operating conditions: a powered and a depowered state. For each of these states, the aerodynamic coefficients are determined from the trimmed flight condition corresponding to the respective depower setting u_d ($u_{d_{\text{in}}}$ and $u_{d_{\text{out}}}$ for the reel-in and reel-out phases, respectively). The depower setting is controlled through the depower line, which is connected to the rear bridle lines. Adjusting the length of this line modifies the relative length between the front and rear bridle lines. Increasing the depower line length results in a depowered configuration, whereas shortening it powers the kite.

The trim state is obtained by aligning the tether force vector with the aerodynamic force vector by adjusting the angle of attack. In equilibrium, this alignment occurs when the pitching moment about the body-fixed y-axis (spanwise) is zero, i.e. when the pitching moment coefficient C_{m_y} equals zero. This condition determines the trimmed angle of attack, α_{trim}, which is then used to evaluate the aerodynamic performance of the kite.

This principle is illustrated schematically in Figure 5.4. The central figure depicts the trimmed condition, in which the aerodynamic and tether forces are aligned. The figures on the left and right correspond to configurations with elongated and shortened depower lines, respectively, which result in untrimmed states due to a non-zero pitching moment.

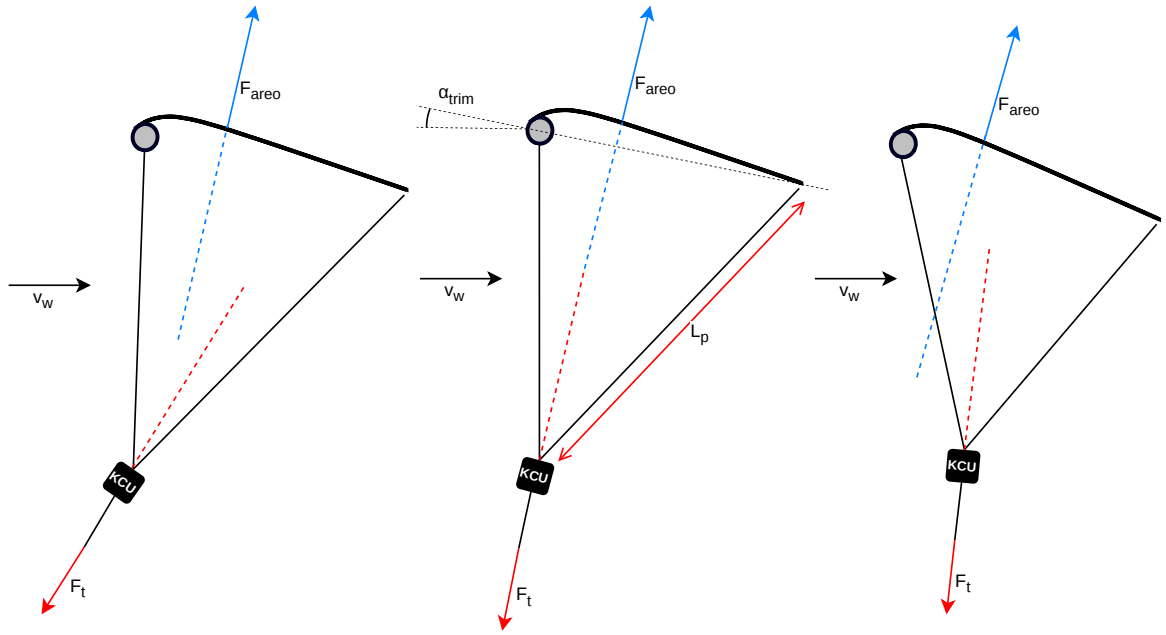

Figure 5.4: Trim angle computation logic: elongated depower line (left), shortened depower line (right), and trim state (middle).

For the reference TU Delft V3 kite, the powered and depowered trim states are defined based on target angles of attack of 8° and 1°, respectively [12]. The corresponding depower line settings are determined iteratively such that the trimmed equilibrium condition ($C_{m_y} = 0$) results in these target angles of attack. The reference bridle geometry and the corresponding depower settings are given in Table 5.1 as a percentage of the CAD indicated rear bridle length.

During optimisation, geometrical reshaping of the kite will also affect the bridle geometry, as described in Section 4.4. The relative depower settings listed in Table 5.1 are therefore maintained as percentages of the current rear bridle length. This approach allows the powered and depowered configurations to be consistently reconstructed for each candidate geometry, thereby enabling the computation of the corresponding trim states.

Table 5.1: Bridle line lengths of the TU Delft V3 Kite for different depower settings.

Bridle line	Length (m)	% of ref	u_d
Front	11.1	-	-
Back (CAD)	11.0654	*ref*	1.0
Back (reel-out)	11.1014	+0.33%	1.0033
Back (reel-in)	11.7254	+5.96%	1.0596

5.3.2. Turning radius

An important operational parameter of an AWE kite is its turning behaviour. A small turning radius allows it to fly closer to the ground and closer to the centre of the wind window, where

the potential wind power is higher. Two methods used for computing the turning radius are explained in this section, after which Section 5.3.3 expands on its influence on the average elevation and azimuth angle. The two complementary approaches used to evaluate the turning radius are a force equilibrium method and an inertia method.

Force equilibrium based turning radius

The force-based formulation, derived by Gaunaa et al. [19], equates the centrifugal force required for turning to the aerodynamic side force generated by the kite:

$$R = \frac{m_k v_{k,\tau}^2}{F_{a,s} + m_k \mathbf{g} \cdot \mathbf{e}_{y,k}}, \tag{5.1}$$

where R is the turning radius, m_k is the kite mass, $v_{k,\tau}$ is the tangential kite velocity, $F_{a,s}$ is the aerodynamic side force, $\mathbf{g}$ is the gravitational acceleration vector, and $\mathbf{e}_{y,k}$ is the spanwise unit vector of the kite reference frame. The tangential kite velocity is obtained from the tangential component of the apparent wind velocity [45]:

$$\lambda = \frac{v_{k,\tau}}{v_w}, \tag{5.2}$$

rewriting to:

$$v_{k,\tau} = \lambda v_w, \tag{5.3}$$

with the velocity ratio λ defined as:

$$\begin{aligned} \lambda &= a + \sqrt{a^2 + b^2 - 1 + \left(\frac{L}{D}\right)^2 (b - f)^2}, \\ a &= \cos\theta \cos\phi \cos\chi - \sin\phi \sin\chi, \\ b &= \sin\theta \cos\phi. \end{aligned} \tag{5.4}$$

and f is the reeling factor [45], given by

$$f = \frac{v_t}{v_w}, \qquad f_{opt} = \frac{1}{3}. \tag{5.5}$$

When considering the moment in the figure-eight turn where the kite flies downwards, the spanwise component of the kite's weight becomes negligible. Thus, Equation (5.1) can be simplified to:

$$TR = \frac{m_k v_{k,\tau}^2}{F_{a,s}}. \tag{5.6}$$

The side force $F_{a,s}$ can be obtained from a sideslip simulation using the VSM. For the reference TU Delft V3 kite, a sideslip angle of 5° was found at maximum turning input [12], which is fixed within this optimisation framework. From the VSM simulation, the sideslip force coefficient C_s is determined. The aerodynamic side force is then calculated, following the lift equation [2], as:

$$F_{a,s} = \frac{1}{2}\rho v_w^2 S_s C_s, \tag{5.7}$$

where S_s is the side-projected area.

Inertia-based turning radius

The second method for estimating the turning radius uses the kite's moment of inertia and the moment induced by the side force. The side force is assumed to act at the quarter-chord point of the tip airfoils, as illustrated in Figure 5.5. In addition, the kite is approximated as a thin rectangular plate with uniform mass distribution for the moment of inertia calculation, as shown in Figure 5.6.

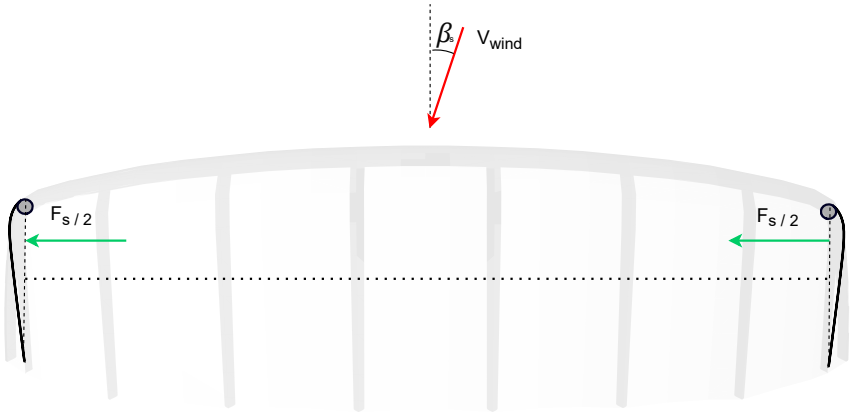

Figure 5.5: Side force reaction during sideslip.

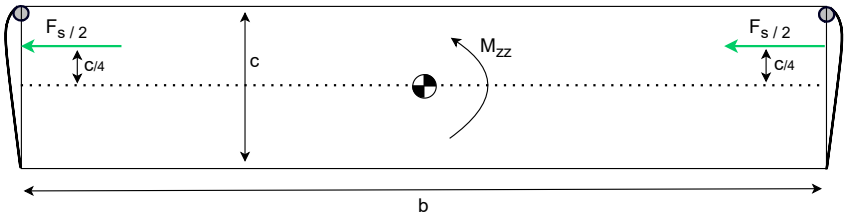

Figure 5.6: Moment of inertia approximation and induced moment.

The turning behaviour is linked to the side force through a moment balance. From the free-body diagram in Figure 5.6, the sum of moments about the yaw axis is:

$$\sum M_{zz} = \sum F \cdot d = \frac{F_s}{2} \cdot \frac{c_{tip}}{4} + \frac{F_s}{2} \cdot \frac{c_{tip}}{4} = \frac{F_s c_{tip}}{4}, \tag{5.8}$$

where c_{tip} is the chord length at the wing tips. This moment can also be expressed as the torque acting on the kite, related to angular acceleration in yaw and the moment of inertia:

$$\sum M_{zz} = \mathcal{T} = \ddot{\chi} I_{zz}, \tag{5.9}$$

where $\mathcal{T}$ is the applied torque and I_{zz} is the moment of inertia about the yaw axis. To determine the required angular acceleration, the turning motion is simplified as a half-circle, as shown in Figure 5.7. The angular velocity is assumed to reach its maximum at time t_2, corresponding to a downward flight. The time required to accelerate angular from t_1 to t_2 is given by:

$$t_2 = \frac{\pi}{2} \frac{TR}{v_{k,\tau}} \tag{5.10}$$

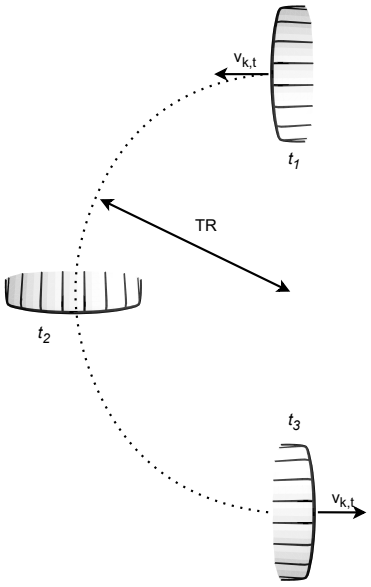

Figure 5.7: Ideal turn flight path.

The angular acceleration can be derived from the angular velocity and the time required to perform the turn. For a quarter-circle turn, the total change in course heading angle is

$$\Delta\chi = \frac{\pi}{2}. \tag{5.11}$$

Assuming a constant angular acceleration from rest ($t = t_1$), the angular velocity increases linearly with time:

$$\dot{\chi}(t) = \ddot{\chi}\, t. \tag{5.12}$$

At time t_2, the angular velocity reaches its maximum value corresponding to the half-circle turn. The total rotation is therefore

$$\chi(t_2) = \int_0^{t_2} \dot{\chi}(t)\, dt = \int_0^{t_2} \ddot{\chi}\, t\, dt = \frac{1}{2}\ddot{\chi} t_2^2. \tag{5.13}$$

Substituting $\chi(t_2) = \frac{\pi}{2}$ yields:

$$\frac{\pi}{2} = \frac{1}{2}\ddot{\chi}t_2^2, \tag{5.14}$$

rewriting to:

$$\ddot{\chi} = \frac{\pi}{t_2^2}. \tag{5.15}$$

Substituting (5.10) into Equation (5.15) gives:

$$\ddot{\chi} = \frac{\pi}{\left(\frac{\pi}{2}\frac{TR}{v_{k,\tau}}\right)^2} = \frac{4}{\pi}\frac{v_{k,\tau}^2}{TR^2}. \tag{5.16}$$

Substituting (5.16) into (5.9) results in:

$$\sum M_{zz} = \mathcal{T} = I_{zz}\ddot{\chi} = I_{zz}\frac{4}{\pi}\frac{v_{k,\tau}^2}{TR^2}. \tag{5.17}$$

Combining (5.8) and (5.17) yields:

$$\frac{F_s c_{tip}}{4} = I_{zz}\frac{4}{\pi}\frac{v_{k,\tau}^2}{TR^2}, \tag{5.18}$$

which can be rearranged to give the turning radius:

$$TR = \sqrt{\frac{16}{\pi}\frac{I_{zz}v_{k,\tau}^2}{F_s c_{tip}}}. \tag{5.19}$$

Using Equation (5.7), Equation (5.19) can be rewritten to be independent to $v_{k,\tau}$, resulting in:

$$TR = \sqrt{\frac{32}{\pi}\frac{I_{zz}}{\rho S_s C_s c_{tip}}}. \tag{5.20}$$

5.3.3. Average elevation and azimuth angle

Under ideal crosswind conditions, an airborne wind energy system operates most efficiently when the kite remains closely aligned with the wind direction, allowing it to extract the maximum aerodynamic power. Deviations from this ideal condition, such as increased elevation during reel-out, reduce the effective apparent wind component acting on the kite. The difference between ideal crosswind flight and elevated flight is illustrated in Figure 5.8. Consequently, the average elevation angle during reel-out is a critical operational parameter for optimising AWESs.

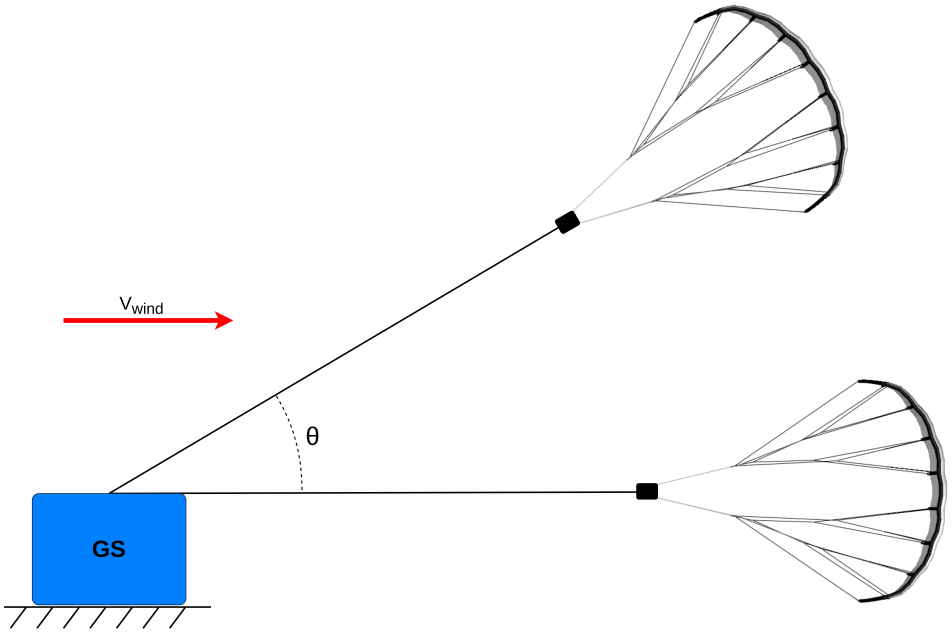

Figure 5.8: Ideal crosswind flight (horizontal) compared to a more realistic elevated flight.

From the minimum turning radius, the average elevation angle is determined by considering the kite in the highest risk scenario closest to the ground and shortest tether length, as illustrated in Figure 5.9. Using the turning radius obtained from Equation (5.20), the minimum average elevation angle is derived from the ground clearance of the reference kite at an average elevation angle of 25°. The ground clearance (GC) is calculated as:

$$GC = L_{\text{t,min}} \frac{\pi\, \theta_{\text{ref}}}{180} - TR, \tag{5.21}$$

where $L_{\text{t,min}} = 270\,\text{m}$ is the minimum tether length and $\theta_{\text{ref}} = 25°$ is the reference elevation angle. For the reference V3 kite, Equation (5.21) results in a minimum ground clearance of 97.6 m. Assuming the ground clearance remains constant during the optimisation, the reshaped kite with a different turning radius will fly at a different average elevation angle. The average elevation angle during the optimisation process is therefore calculated as:

$$\theta_{\text{average}} = 180 \frac{TR + GC}{\pi\, L_{\text{t,min}}}. \tag{5.22}$$

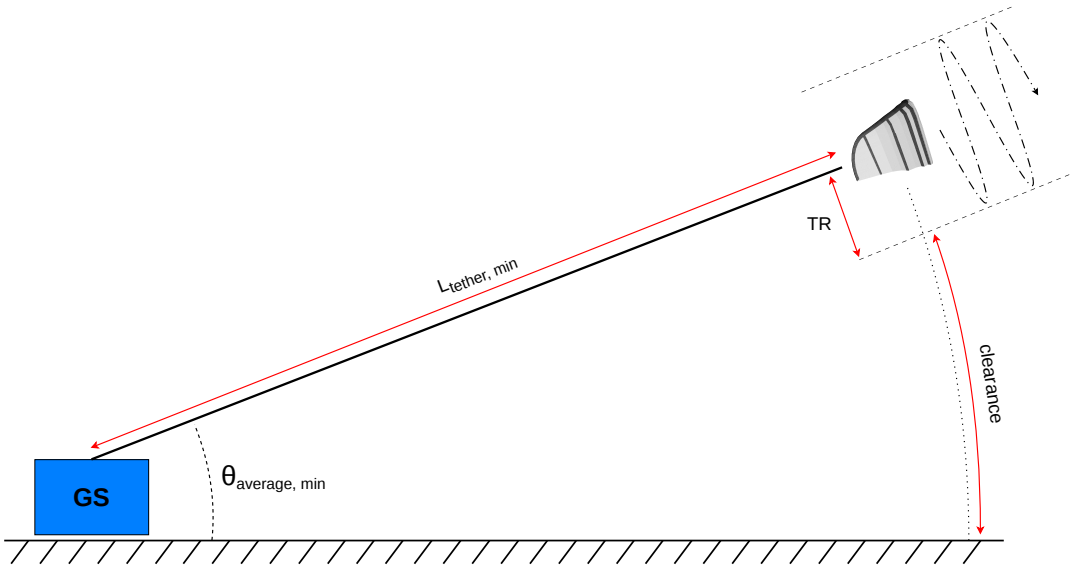

Figure 5.9: Ground clearance at minimum tether length.

For a comparable purpose, the average azimuth angle of the flight trajectory affects the power production potential of an AWES and is closely linked to the turning radius. Based on the simplified flight path shown in Figure 5.10, the trajectory was approximated as being two times wider than it is tall. From this geometry, the average azimuth angle ($\phi_{average}$) corresponds to a lateral offset equal to the turning radius from the pattern's centreline. This azimuth angle influences the kite's apparent wind speed and, consequently, the generated traction force. The azimuth and elevation angles are computed for each wind speed and provided as inputs to the Luchsinger model, which affects the predicted power output of the AWES.

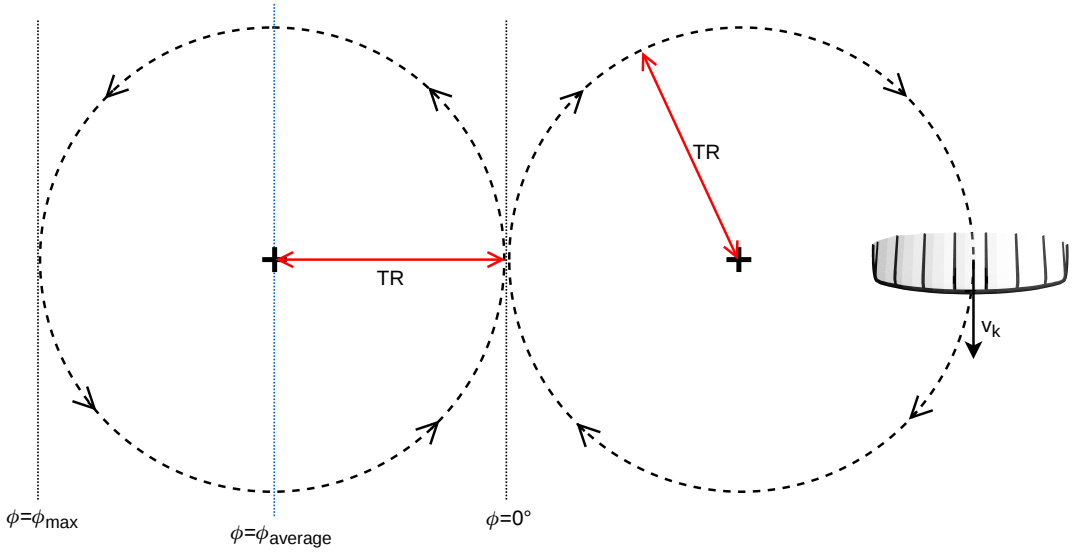

Figure 5.10: Figure-eight flight trajectory used for average azimuth angle calculations.

5.4. Optimisation algorithms

Optimising kite geometry in the GeKO framework requires an algorithm that efficiently explores a high-dimensional design space while handling non-linear, potentially non-smooth objective functions. Given the problem's multidisciplinary nature and the black-box-like

nature of the simulation tools, gradients are not always readily available. Therefore, gradient-free optimisation methods are considered most suitable for this work. In this section, three candidate optimisation algorithms are introduced: Hooke and Jeeves pattern search, covariance matrix adaptation Evolution Strategy (CMA-ES), and particle swarm optimisation (PSO) as implemented in PySwarms.

5.4.1. Hooke and Jeeves pattern search

The Hooke and Jeeves pattern search method is a classical derivative-free optimisation algorithm based on exploratory and pattern moves [25]. The algorithm iteratively explores the design space by evaluating the objective function along each coordinate direction. If an improvement is found, a pattern move is performed in the direction of the successful exploratory steps. The step size is reduced progressively to improve local convergence.

The key advantages of Hooke and Jeeves are its simplicity and low computational costs. However, the method can become inefficient in high-dimensional design spaces, and it is sensitive to the initial step size. Additionally, the algorithm may converge to local optima if present in the design space. For the GeKO framework, Hooke and Jeeves can serve as a useful baseline algorithm for quick initial exploration or for small-dimensional sub-problems.

5.4.2. CMA-ES optimisation

Covariance matrix adaptation evolution strategy (CMA-ES) is a stochastic, population-based optimisation method designed for non-linear, non-convex, and non-smooth problems [23]. The algorithm maintains a multivariate normal distribution over the design space, from which candidate solutions are sampled. The covariance matrix is iteratively updated using the best-performing samples, enabling the algorithm to learn correlations among design variables and adapt its search direction.

CMA-ES is well-suited for the kite geometry optimisation problem due to its robustness and ability to handle complex, multimodal objective functions. It is particularly effective when gradient information is unavailable or unreliable. The main drawback is its computational cost, as each iteration requires evaluating multiple candidate solutions. In the GeKO framework, CMA-ES is therefore best suited for high-fidelity optimisation runs or as a final refinement stage after a coarser search.

5.4.3. PySwarms particle swarm optimisation

Particle swarm optimisation (PSO) is a population-based algorithm inspired by the social behaviour of flocks and swarms [29]. Each particle represents a candidate solution and moves through the design space based on its own best-known position and the swarm's global best position. The algorithm balances exploration and exploitation through inertia, cognitive, and social coefficients.

PySwarms is an open-source Python implementation of PSO that provides flexible options for swarm configuration, boundary handling, and convergence criteria [35]. PSO is attractive for the GeKO framework because it is simple to implement, easily parallelisable, and capable of exploring large design spaces. However, PSO can suffer from premature convergence and may require careful hyperparameter tuning. In addition, the stochastic nature of the method may yield inconsistent results across runs.

5.4.4. Algorithm selection and integration

The selection of the optimisation algorithm depends on the computational budget, required robustness, and desired convergence properties. The Hooke and Jeeves pattern search algorithm

offers a lightweight approach suitable for initial design exploration or low-dimensional problems. CMA-ES provides strong global search capability and robustness for high-dimensional and non-smooth objectives, making it a suitable choice for final optimisation runs. PySwarms PSO offers a compromise between computational cost and exploration capability and can be used when parallel candidate evaluation is available.

Within the GeKO framework, a hybrid optimisation strategy can be considered in which a computationally efficient method, such as the Hooke–Jeeves algorithm, is first employed to obtain an initial feasible design. Subsequently, a global optimisation method, such as CMA-ES or PSO, can be applied to further explore the design space and refine the solution. Such an approach can reduce the overall computational cost while increasing the likelihood of identifying a near-optimal design.

In the implemented framework, the Hooke and Jeeves pattern search algorithm was selected to minimise optimisation time and enable initial exploration of the design space. The results obtained using this optimisation framework are discussed in Section 6.6.

6

Results

The methodologies described in Chapter 3, Chapter 4, and Chapter 5 are combined to verify tool functionality, explore the design space, and demonstrate optimisation. First, the functionality of the kite geometry parametrisation and reshaping method is evaluated in Section 6.1. Following, the aerodynamic results obtained with the VSM are analysed in Section 6.2. The resulting operational conditions, expressed in elevation and azimuth angles, are presented in Section 6.3. Next, in Section 6.4, the performance evaluation is checked with the power curve of the reference TU Delft V3 kite. The feasible design space is then explored and discussed in Section 6.6. Based on this exploration, the optimisation results and the resulting kite design are presented in Section 2.4.3. Finally, a sensitivity analysis of the optimisation framework is provided in Section 6.7.

6.1. Geometric planform reshaping

The geometric parameter scaling of the kite wing planform is split into the individual parameters AR, ab, cd, and Γ. For illustrative purposes, the kites in Figure 6.2a, 6.3a, and 6.4a are not aligned at tip height as in the reshaping methods, but rather aligned at the centre chord.

Effect of AR

In Figure 6.1a and 6.1b, it can be seen that scaling the AR does not influence the arc curve. This is because the control points are placed at locations determined as percentages of the kite's total height and width, as described in Section 4.2. Although it might seem that the high AR kite, or even the low AR kite, has a higher area, this remains constant in reshaping by chord scaling.

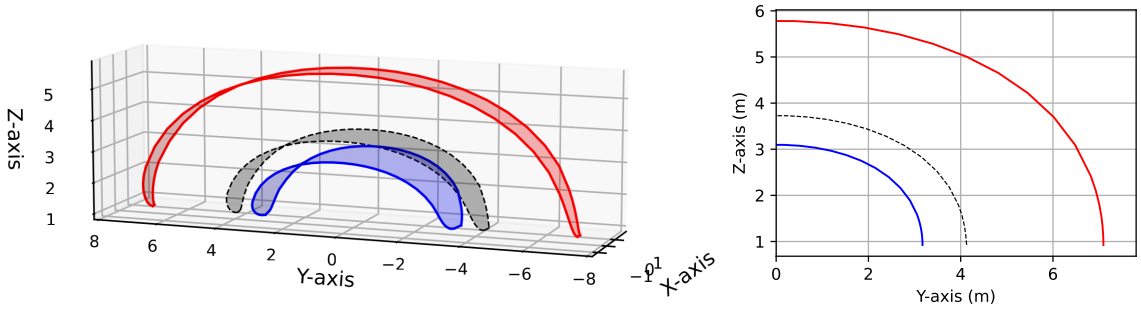

(a) Isometric geometry.

(b) Projected arc shape.

Figure 6.1: Kite isometric geometry with AR = 3.0 (blue), AR = 15.0 (red), and AR = 5.0 (black); fixed parameters ab = 0.57, cd = 0.63, Γ = 0.60.

Effect of ab

Changing the control point distance ab directly changes the arc shape. As already seen in Figure 6.2b for the arc shape, but in context for the entire kite geometry in Figure 6.2a, the kite adapts to a more pointy (blue) or rectangular (red) shape. As can be observed, very low values for ab create a very pointy kite. This, however, is not favourable and physically impossible from a structural perspective, since soft-wing kites should follow a smooth arc shape. This is why a lower bound of 0.2 will be added to the parameter in the following analyses.

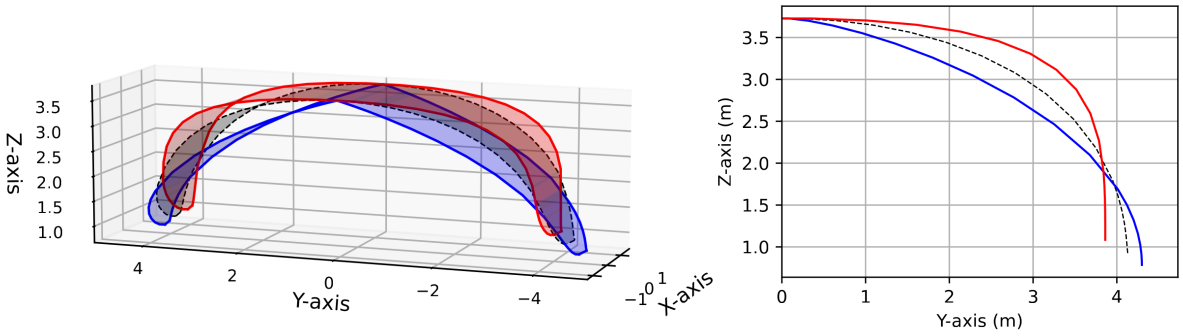

(a) Isometric geometry. **(b)** Projected arc shape.

Figure 6.2: Kite isometric geometry with $ab = 0.0$ (blue), $ab = 1.0$ (red), and $ab = 0.57$ (black); fixed parameters $AR = 5.08$, $cd = 0.63$, $\Gamma = 0.60$.

Effect of cd

Similarly to ab, the arc control point distance cd directly influences the arc shape. Lowering the value (blue) releases tension on the tips of the shape, resulting in a flatter design. Again, more rectangular shapes are made possible when increasing cd (red).

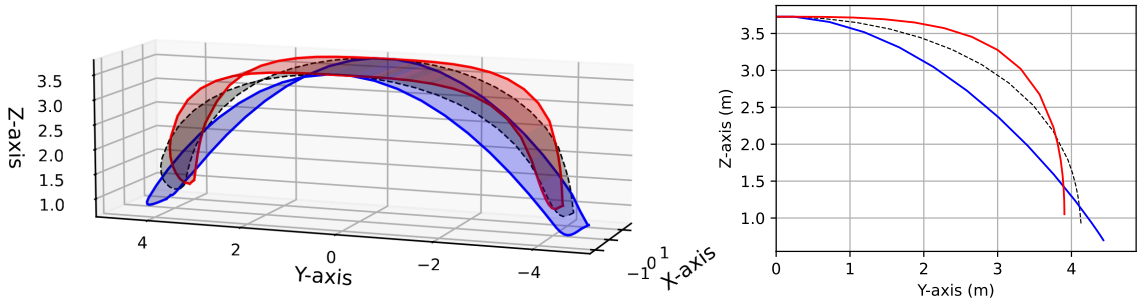

(a) Isometric geometry. **(b)** Projected arc shape.

Figure 6.3: Kite isometric geometry with $cd = 0.0$ (blue), $cd = 1.0$ (red), and $cd = 0.63$ (black); fixed parameters $AR = 5.08$, $ab = 0.57$, $\Gamma = 0.60$.

Effect of Γ

The bounds of Γ are set as seen in its extremes in Figure 6.4. With $\Gamma = 0$ a flat kite is produced. However, due to structural and turning reasons, this shape is not a physically possible design. With the outlook of structural simulations added to the toolchain, this design flexibility can serve as an important test for implementation.

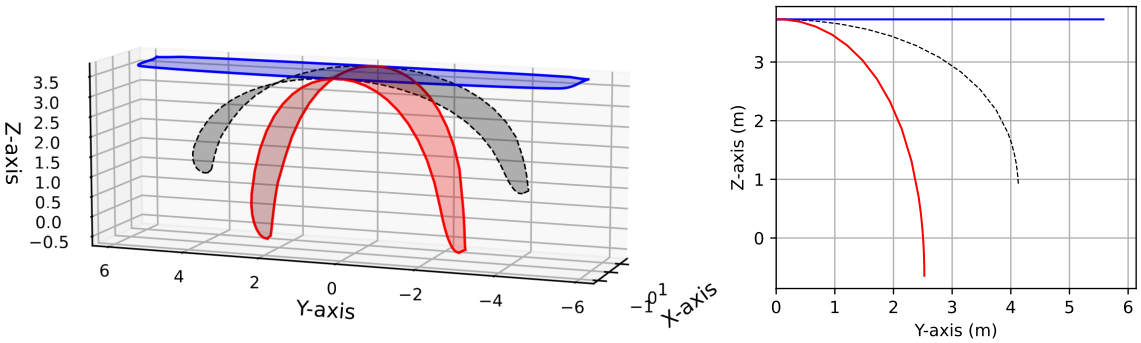

(a) Isometric geometry.

(b) Projected arc shape.

Figure 6.4: Kite isometric geometry with $\Gamma = 0.0$ (blue), $\Gamma = \frac{\pi}{3}$ (red), $\Gamma = 0.60$ (black); fixed parameters $AR = 5.08$, $ab = 0.57$, $cd = 0.63$.

Projected area

The projected area is an important factor in the performance of AWE kites, as it strongly correlates with tractional force and turning capabilities. Here, the effect of the three arc-shape parameters and the AR are given in Figure 6.5–6.8. This knowledge could be useful for explaining the dependencies between kite performance and geometry.

The AR dependency on projected areas in Figure 6.7 is very small, which is expected since area is kept constant and area distribution is not altered. When only the AR is changed, the arc, and thus all other geometrical parameters, remain untouched. Therefore, the ratio between the top projected area and the side projected area is expected to remain relatively unchanged. Only a small change in projected areas was found, as seen in Figure 6.7.

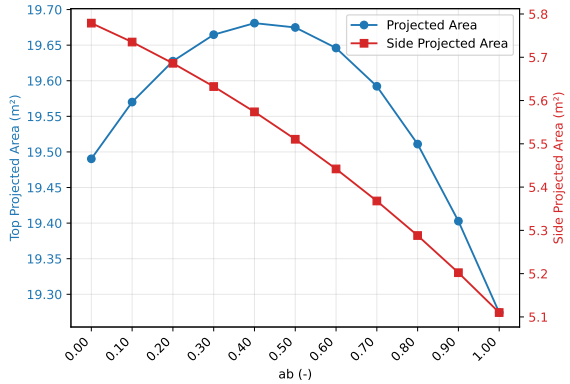

Figure 6.5: Projected area at variable ab.

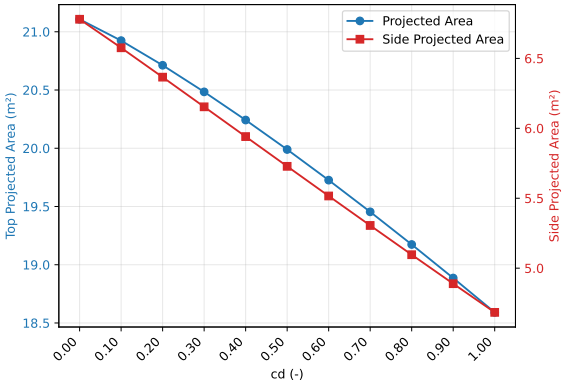

Figure 6.6: Projected area at variable cd.

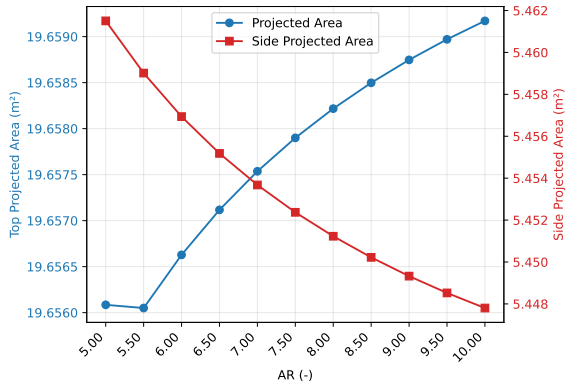

Figure 6.7: Projected area at variable AR.

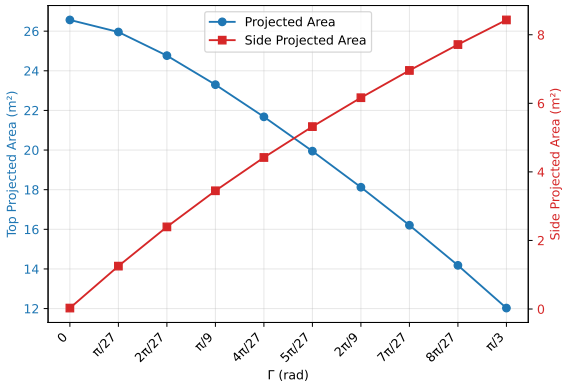

Figure 6.8: Projected area at variable Γ.

6.2. Aerodynamic analysis

The effects of scaling individual geometric parameters to the aerodynamic performance of the kite, obtained with the VSM, are given in Figure 6.9–6.12 for parameters ab, cd, AR, and Γ, respectively.

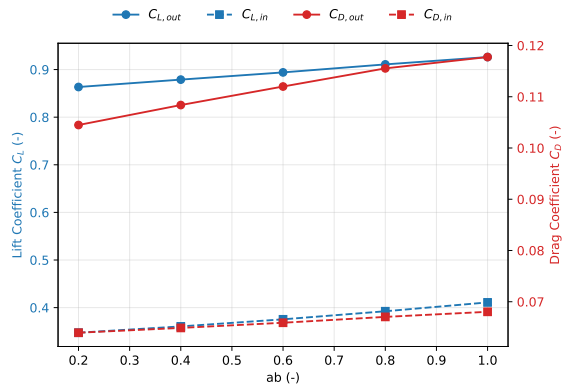

Figure 6.9: Aerodynamic coefficients at variable ab; fixed parameters $AR = 5.0$, $cd = 0.6$, $\Gamma = 0.6$, $x_\kappa = 1.0$.

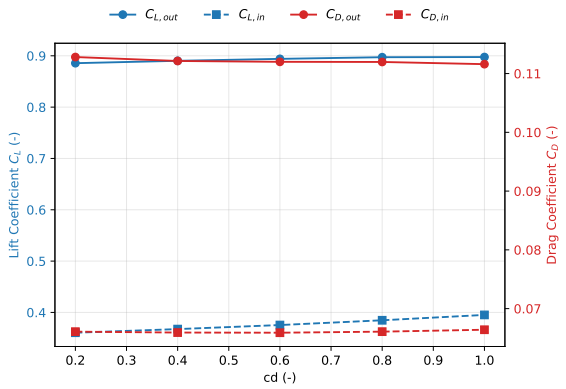

Figure 6.10: Aerodynamic coefficients at variable cd; fixed parameters $AR = 5.0$, $ab = 0.6$, $\Gamma = 0.6$, $x_\kappa = 1.0$.

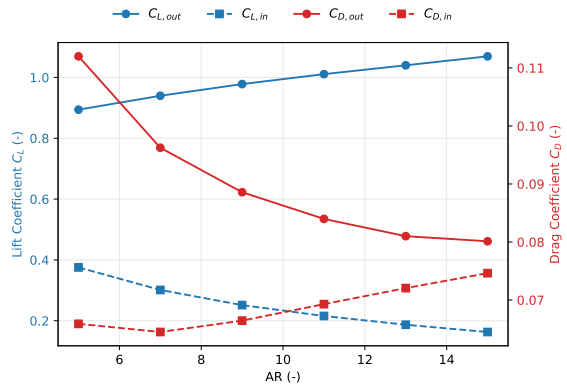

Figure 6.11: Aerodynamic coefficients at variable AR; fixed parameters $ab = 0.6$, $cd = 0.6$, $\Gamma = 0.6$, $x_\kappa = 1.0$.

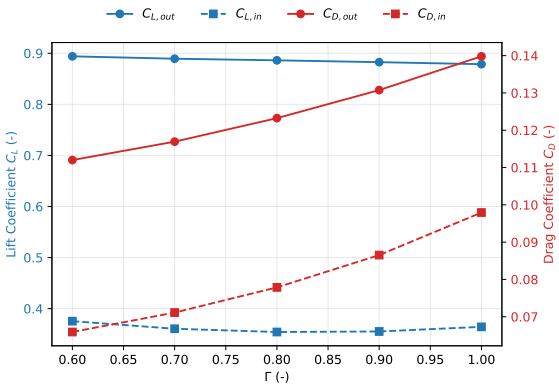

Figure 6.12: Aerodynamic coefficients at variable Γ; fixed parameters $AR = 5.0$, $ab = 0.6$, $cd = 0.6$, $x_\kappa = 1.0$.

The effect of scaling the camber height of the individual airfoils on the 3-dimensional aerodynamics is given in Figure 6.13. Larger camber geometry results in higher lift and drag coefficients as expected. Also, the drag coefficient is more influenced by the camber than the lift coefficient.

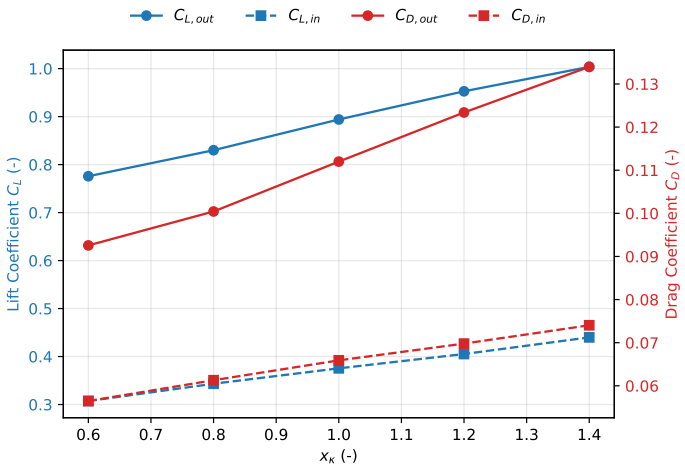

Figure 6.13: Aerodynamic coefficients at variable x_κ; fixed parameters $AR = 5.0$, $ab = 0.6$, $cd = 0.6$, $\Gamma = 0.6$.

6.3. Operational analysis

From an operational view, the effect of the geometric properties of the kite on the flying behaviour can be analysed. As explained in Section 5.3.2, the turning radius depends on the geometry and is calculated using Equation (5.20). The effect of the AR on the turning radius is plotted in Figure 6.14. Since a higher AR increases the span, increasing the moment of inertia I_{zz}, the turning radius increases accordingly. The elevation angle θ used in this section all refer to the elevation angle measured from the ground (θ_{ground}).

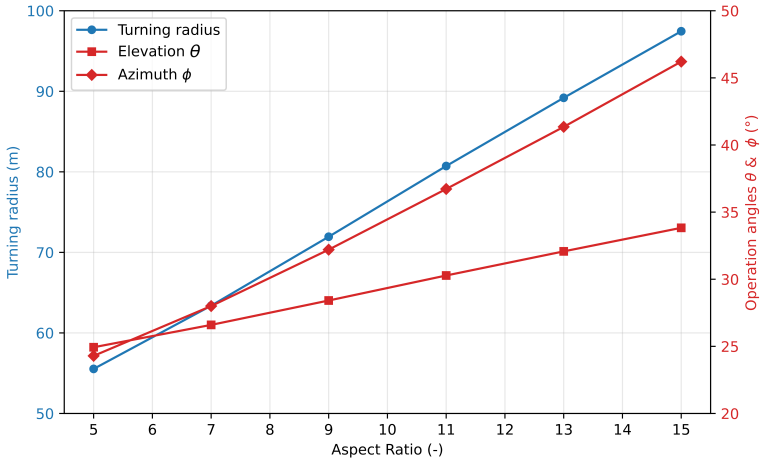

Figure 6.14: The effect of the AR on the turning radius and operation angles; fixed parameters $ab = 5.0$, $cd = 0.6$, $\Gamma = 0.6$, $x_\kappa = 1.0$.

From this turning radius, the average elevation angle and azimuth angle are determined following the method described in Section 5.3.3. The effect of the design vector parameters ab, cd, AR, and Γ are plotted in Figure 6.15-6.18 respectively. From Equation (5.20), the geometry-dependent parameters, moment of inertia around the z-axis (I_{zz}) and the side projected area S_s, compute the turning radius. The influence of this is nicely displayed in Figure 6.16. From Figure 6.6, it was found that the projected side area increases for lower values of cd. Next to that, in Figure 6.3a, it can be seen that the projected span increases for increased values of cd, which increases I_{zz}. In Figure 6.16, for low values of cd, the effect of the I_{zz} increase dominates, while for higher values of cd, the increased S_s increases the turning capabilities of the kite.

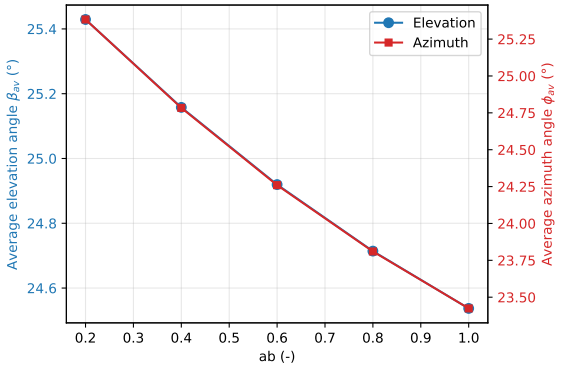

Figure 6.15: Average elevation and azimuth angle variation at variable ab; fixed parameters $AR = 5.0$, $cd = 0.6$, $\Gamma = 0.6$, $x_\kappa = 1.0$.

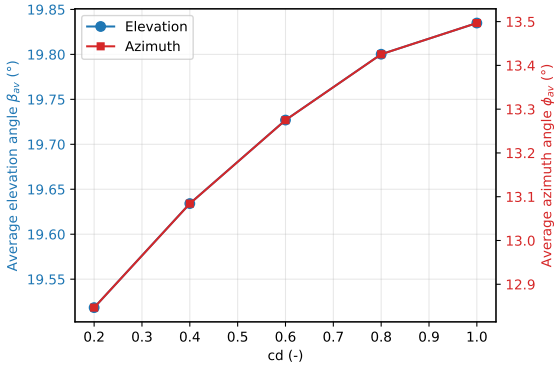

Figure 6.16: Average elevation and azimuth angle variation at variable cd; fixed parameters $AR = 5.0$, $ab = 0.6$, $\Gamma = 0.6$, $x_\kappa = 1.0$.

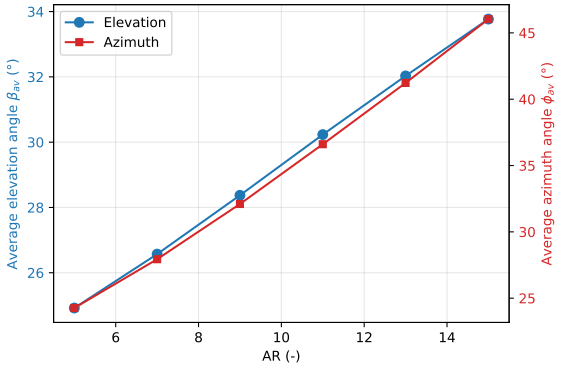

Figure 6.17: Average elevation and azimuth angle variation at variable AR; fixed parameters $ab = 0.6$, $cd = 0.6$, $\Gamma = 0.6$, $x_K = 1.0$.

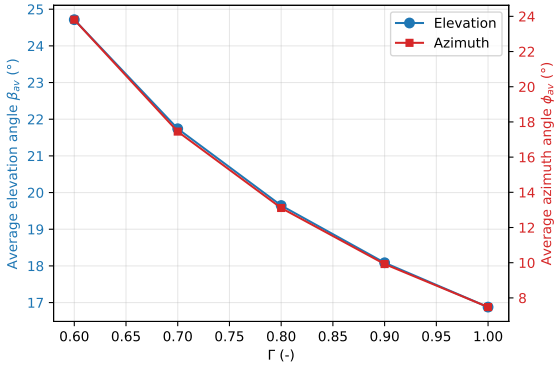

Figure 6.18: Average elevation and azimuth angle variation at variable Γ; fixed parameters $AR = 5.0$, $ab = 0.6$, $cd = 0.6$, $x_K = 1.0$.

Finally, the 8-figure flight paths for the elevation and azimuth angle limitations within the feasible design space are illustrated in Figure 6.19. From Figure 6.15-6.18, it is expected that the lowest average elevation and azimuth angles are achieved for a kite with low AR and cd, and a high ab and Γ. The red flight path, corresponding to the largest average elevation and azimuth angles, is expected to be achieved by a kite with a high AR and cd, and a low ab and Γ.

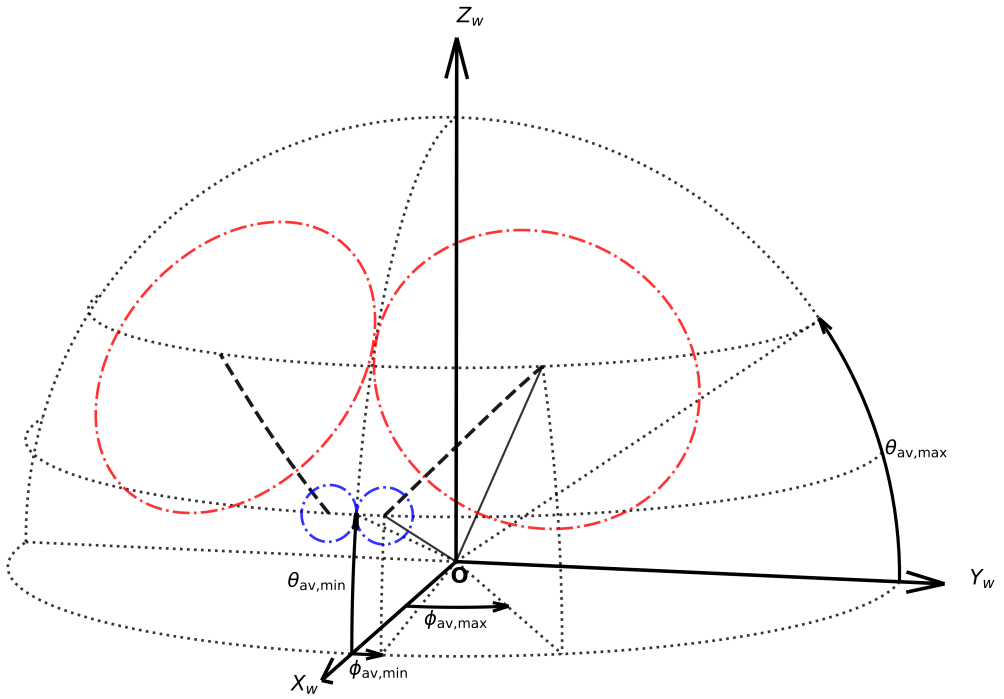

Figure 6.19: Smallest (blue) and largest (red) 8-figure flight paths within the feasible design space, at $\theta_{av,min}$ and $\phi_{av,min}$, and average $\theta_{av,max}$ and $\phi_{av,max}$ respectively.

6.4. Performance of the TU Delft V3 kite

To better understand the results obtained from the Luchsinger model, as described in Section 3.4.3, the reference TU Delft V3 kite was analysed. The power curve obtained from this model is plotted in Figure 6.20, and the operational parameters, including reeling speeds and

elevation angles, are plotted in Figure 6.21.

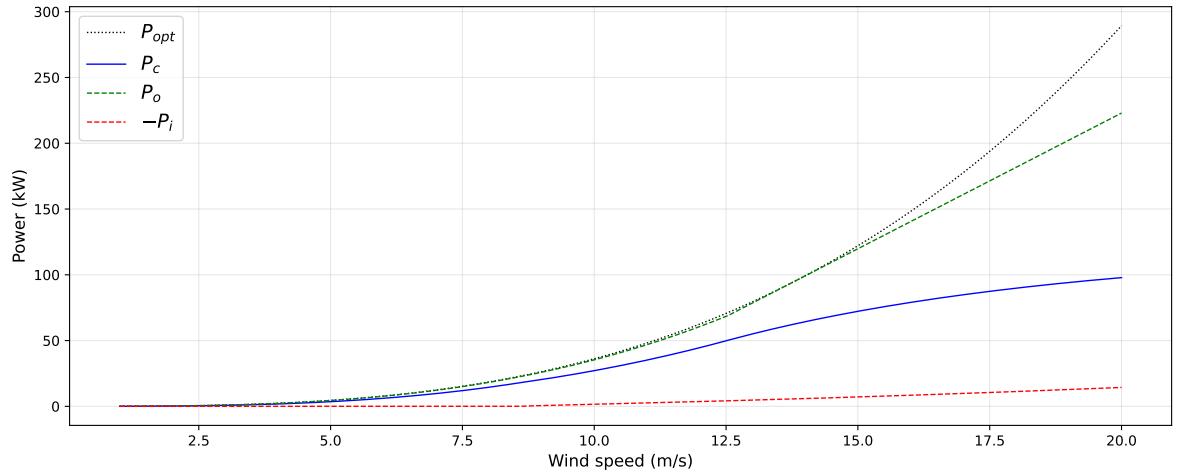

Figure 6.20: Power curve of the TU Delft V3 kite.

In the power curve, P_{opt} depicts an unconstrained optimal power of the system. In real life, various factors limit the system, such as mechanical power and reeling speed limits. Taking these constraints into account, the blue line shows the full-cycle power (P_c), which is the product of the reel-in and reel-out powers, P_i and P_o, respectively. From Figure 6.20, it is clear what the expected cycle power output of the TU Delft V3 kite is at a specific wind speed.

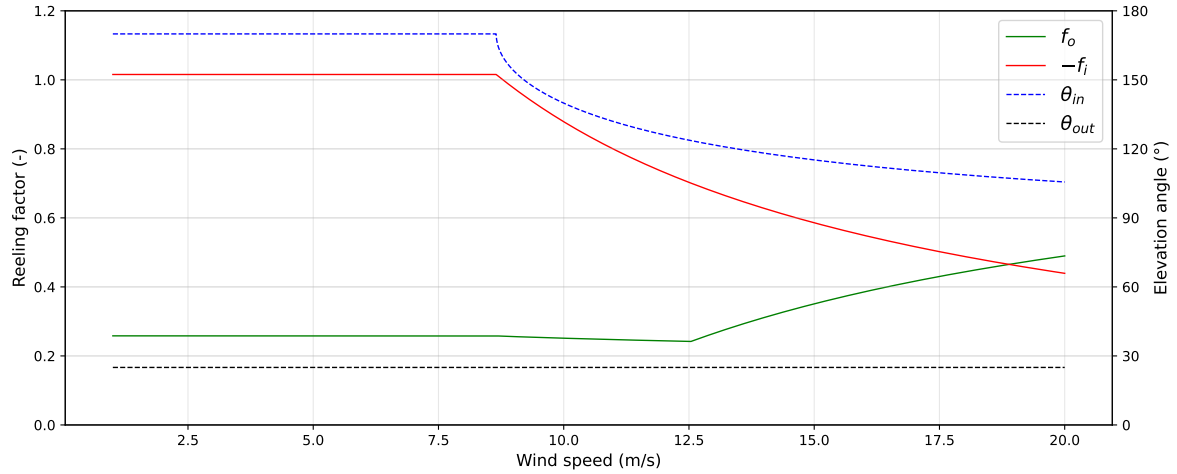

Figure 6.21: Reeling factors and elevation angles of the TU Delft V3 kite.

Also, the elevation angle and reeling speeds for the TU Delft V3 kite are given in Figure 6.21. The first wind regime is defined as the range from 0 to 8.5 m/s, during which the system operates unconstrained. From 8.5 m/s, the reeling speed and elevation angle during reel-in start dropping. This is where the system is constrained by the tether force, also referred to as the second wind regime. The third wind regime for the TU Delft V3 kite in this analysis starts at a wind speed of 12.5 m/s, at which point, in addition to the tether force, the generator power is also constrained. At higher wind speeds, these parameters must be constrained to prevent system malfunctions, such as tether snaps.

Moreover, the flight-scheduling algorithm introduced in Section 3.5 was used to determine the AEP of the TU Delft V3 kite, yielding 62,716 MWh. This can be used to compare results of the optimised kite, which will be discussed in Section 6.6.

6.5. Design space exploration

To understand the kite geometry design problem, a design space exploration was conducted. For this, the implemented toolchain, as presented in Section 5.2 without the optimisation strategy, was run for different points within the considered design space. The solution space, when mapped onto the design space, could provide important insights into optimal solutions and potential local optima. In this exploratory research, all five design vector parameters are constrained to a feasible design space, as shown in Table 6.1. Here, the results given in Section 6.1 are used to constrain the AR and arc shape parameters.

Table 6.1: Design vector bounds for design space exploration.

Arc parameter	Lower bound	Upper bound	Reference Kite
AR (−)	5.0	15.0	5.08
ab (-)	0.2	1	0.573
cd (-)	0.2	1	0.626
Γ (rad)	0.6	1.0	0.601
Γ (°)	34	57	34.4
x_κ (−)	0.8	1.2	1.0

In Figure 6.22–6.24, the solution space is visualised for three of the five design parameters: AR, the camber scaling factor x_κ, and one of the three arc-shape parameters. In all three plots, a consistent increase in AEP is observed with increasing values of the camber scaling factor x_κ, indicating that higher camber generally improves performance across the explored design space.

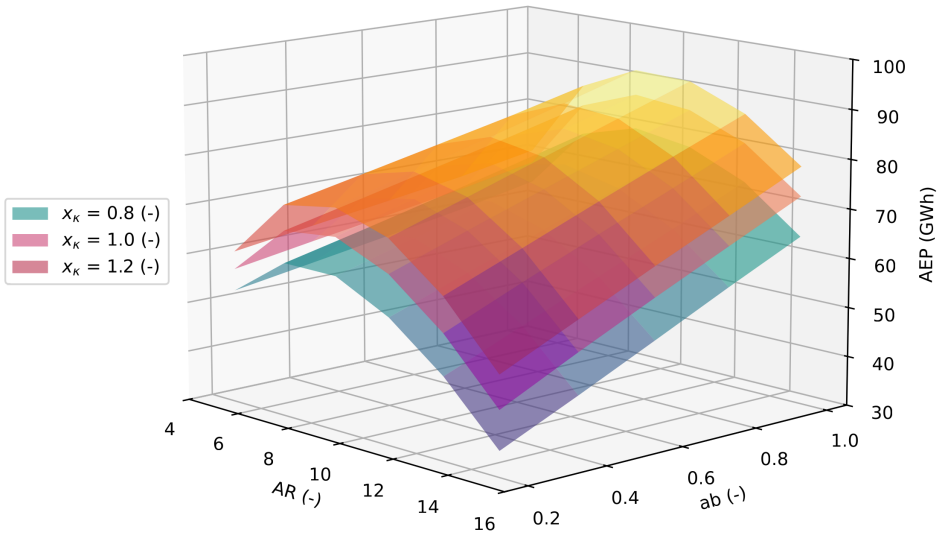

Figure 6.22: AEP for varying AR, ab, and x_κ; fixed parameters $cd = 0.6$, $\Gamma = 0.6$.

As noted from Figure 6.22 and 6.23, for the arc-shape parameters ab and cd, the highest AEP values appear at their respective upper and lower bounds. However, this observation cannot

be considered conclusive, as the visualisations represent only pairwise relationships between parameters and therefore neglect the interdependence among the remaining design variables.

This limitation is illustrated by the behaviour of the AR. In Figure 6.23, the AEP appears to peak around $AR = 10$, whereas in Figure 6.24 the highest values occur near the upper bound of $AR = 15$. These differing trends highlight the strong coupling between the design parameters. Consequently, no definitive conclusion about the AR of the global optimum kite design can be drawn from these partial projections of the solution space.

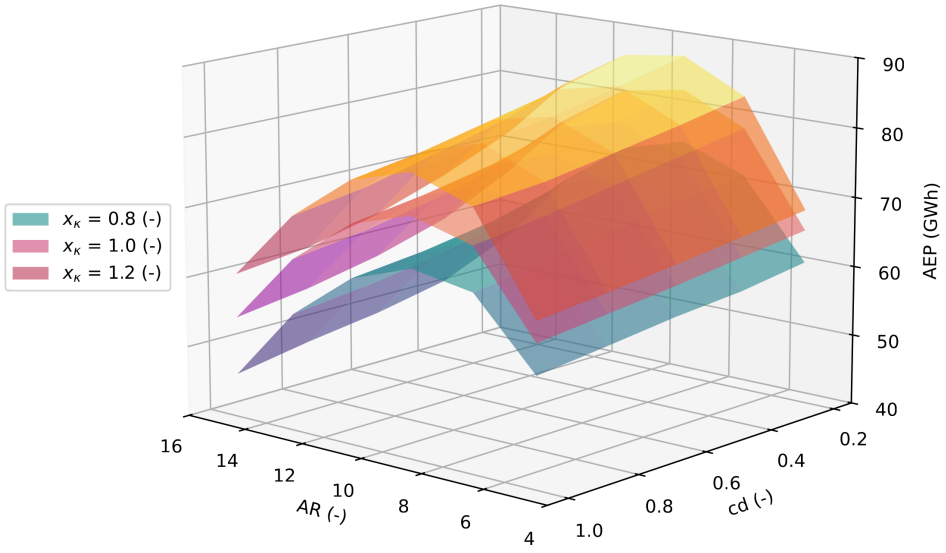

Figure 6.23: AEP for varying AR, cd, and x_κ; fixed parameters $ab = 0.6$, $\Gamma = 0.6$.

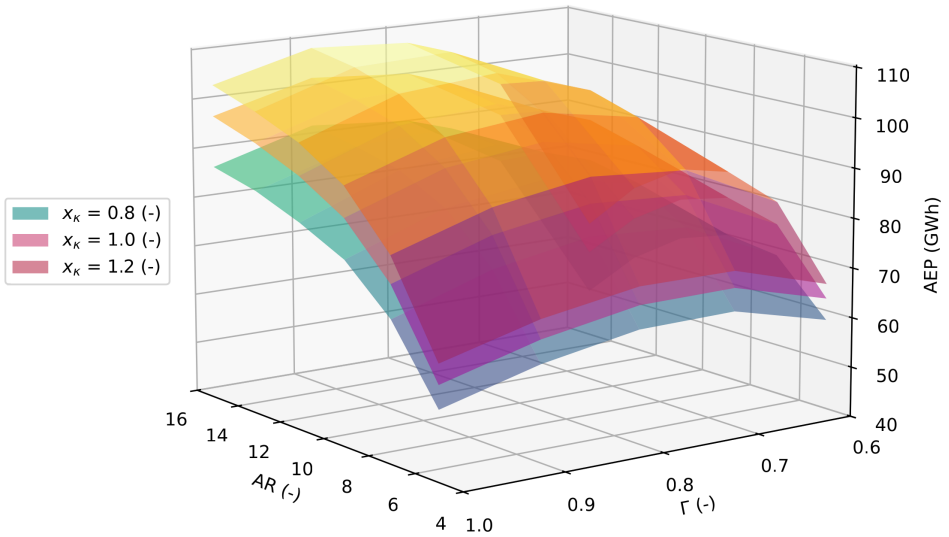

Figure 6.24: AEP for varying AR, Γ, and x_κ; fixed parameters $ab = 0.6$, $cd = 0.6$.

In Figure 6.25, the solution space corresponding to the arc-shape parameters ab, cd, and Γ is presented. Consistent with the trends observed in Figure 6.22 and Figure 6.23, AEP reaches its maximum at $ab = 1.0$ and $cd = 0.2$, both of which lie on the boundaries of the defined feasible design space. In contrast, Γ is the only parameter in the design vector that does not converge

to a boundary value. Instead, its optimum appears within the interval $0.7 \leq \Gamma \leq 0.8$. This indicates that the optimal kite geometry does not correspond to a completely flat configuration, which would negatively affect turning capability. Furthermore, the optimised design tends toward a relatively large projected area, which increases lift generation and consequently enhances the pulling force produced by the kite.

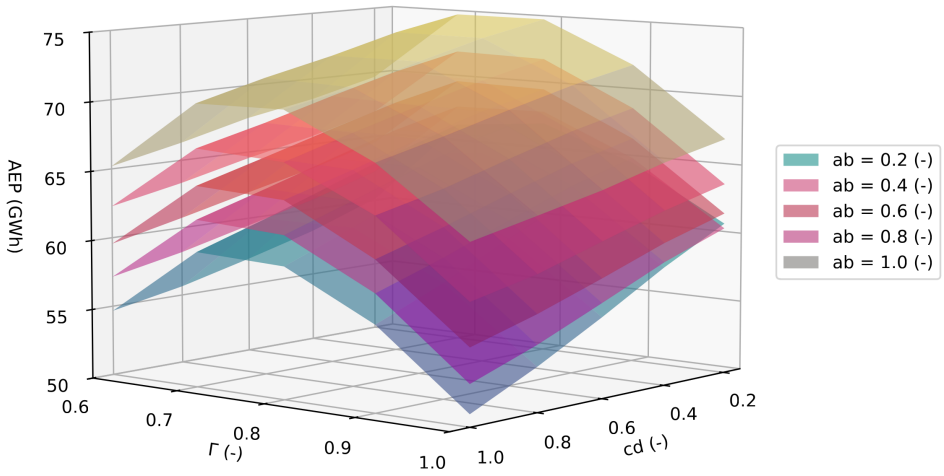

Figure 6.25: AEP for varying arc-shape parameters ab, cd, and Γ; fixed parameters $AR = 5.0$, $x_\kappa = 1.0$.

From this design space exploration, it is expected that the global optimum lies close to the parameter values presented in Table 6.2. Furthermore, no clear indications of local optima are observed within the explored region of the design space. However, their existence cannot be ruled out, as the entire design space has not been completely evaluated.

Table 6.2: Expected optimised design vector.

Parameter	Expected optimised result	Active bound
AR (-)	9-15	no/yes
ab (-)	1.0	yes
cd (-)	0.2	yes
Γ (rad)	0.8-0.9	no
x_κ (-)	1.2	yes

6.6. Optimisation of the TU Delft V3 Kite

The first optimisation case that is run with the GeKO toolchain is the TU Delft V3 for a wind profile in Delft. The design vector bounds are similar to those for design space exploration, except for the AR, allowing for a potential optimised design up to $AR = 20$. The consistency constraints introduced to the optimisation algorithm are listed in Table 6.3. On top of that, the general simulation settings required for the Hooke and Jeeves pattern search algorithm can be found in Table 6.4.

Table 6.3: Design vector bounds for GeKO optimisation.

Parameter	Lower bound	Upper bound
AR	5.0	20.0
ab	0.2	1.0
cd	0.2	1.0
Γ	0.0	$\frac{1}{3}\pi$
x_κ	0.8	1.2

Table 6.4: Simulation settings for the Hooke and Jeeves Pattern Search Algorithm.

Input	Setting
ftol	10.0
period	5
n_max_gen	100

The resulting optimised kite is plotted in Figure 6.26. The geometry of the kite changed significantly during optimisation, as quantified by comparing the optimised and reference design vectors in Table 6.5.

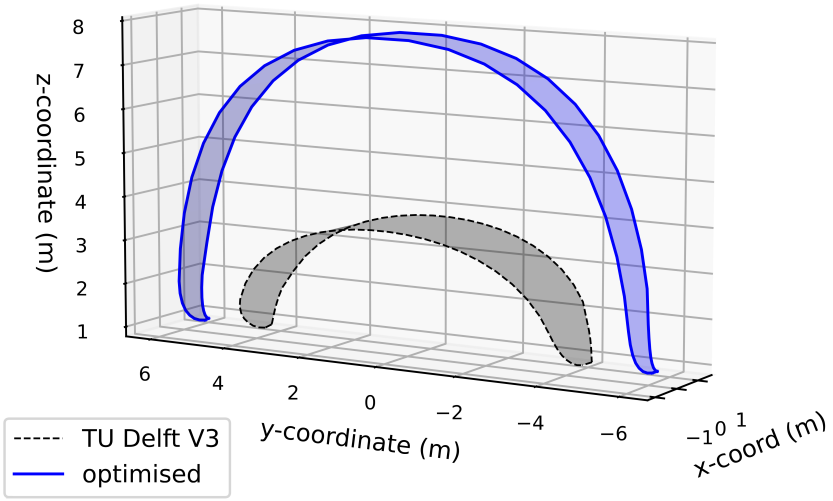

Figure 6.26: Optimised kite geometry compared to TU Delft V3; $AR_{opt} = 17.63$, $ab_{opt} = 1.0$, $cd_{opt} = 0.2$, $\Gamma_{opt} = 0.88$, $x_{\kappa,opt} = 1.2$.

Table 6.5: Optimised design vector comparison to the reference TU Delft V3 kite.

Design parameter	TU Delft V3	Optimised	% from ref
AR (-)	5.08	17.63	+247%
ab (-)	0.572898	1.0	+75%
cd (-)	0.626105	0.2	-68%
Γ (rad)	0.600660	0.877355	+46%
x_κ (-)	1.0	1.2	+20%

As given in Table 6.5, the optimised AR lies outside the initial design space bound of 15, consistent with the trend observed in the solution space exploration. Within the simplified toolchain implemented in this study, a highly slender wing emerges as the optimal kite design. It should be noted that this configuration results from the assumptions embedded in the selected models and the imposed operational conditions. Consequently, the optimisation outcome can be explained by several characteristics of the modelling framework.

The 247% increase in AR can be attributed to the strong dependence of aerodynamic performance on AR. As illustrated in Figure 6.11, an increase in AR results in a higher lift coefficient C_L

and a lower drag coefficient C_D, thereby substantially improving the lift-to-drag ratio. A high lift-to-drag ratio enables large pulling forces during the reel-out phase. Furthermore, the optimisation framework does not penalise large AR values in other disciplines, as structural modelling is not included in the implementation. In practice, however, very high AR kites are structurally challenging due to aero-structural and aeroelastic effects.

The arc shape shows an increase in height ratio, which can be attributed to the dependence of the turning radius on the side force. A taller kite geometry results in a relatively larger side-projected area (as found in Figure 6.8), enabling greater side force during sideslip and thereby improving turning capabilities. However, the method used to calculate the turning radius, introduced in Section 5.3.2, is simplified and does not account for several phenomena associated with turning flight, such as twist, roll, and other deformations associated with flexible structures like soft-wing kites. A more detailed analysis of the turning behaviour in relation to the optimisation outcome is given in Section 6.7.1.

Finally, the camber scaling factor converges to its upper bound of 1.2. This trend is similar to that observed for AR, as increasing the camber scaling factor improves aerodynamic performance. As shown in Figure 6.13, increasing x_κ leads to improved aerodynamic characteristics, therefore increasing pulling force during reel-out.

The reference kite can be compared to the optimised solution based on the AEP. The TU Delft V3 kite produces an AEP of 62.716 GWh, whereas the optimised design yields 121.664 GWh. This corresponds to a 94% performance increase within the simplified simulation framework, demonstrating that the optimised design substantially improves the AEP, which is the primary optimisation objective. The convergence history of both the design vector and the objective function is presented in Appendix D.

Each full evaluation of the implemented toolchain required approximately 30 seconds, resulting in a total optimisation time of roughly 1.5 hours. Compared to conventional design methodologies, which typically involve detailed aerodynamic and performance modelling, physical prototyping, and experimental testing, the resulting reduction in design iteration time is substantial. However, due to the limited scope of the implemented toolchain and the simplifications inherent in the chosen parametrisation, the framework should primarily be regarded as a preliminary design and exploration tool. Consequently, the comparison with current industrial design workflows should be interpreted cautiously, as the framework does not yet capture the full range of physical effects and validation steps required for detailed kite design.

6.7. Sensitivity analysis

Now that the toolchain has been designed, implemented, and analysed, the validity of the obtained results must be assessed. A modelling framework that relies on assumptions, such as the simulation tools integrated in the implemented GeKO tool, requires verification before its outcomes can be reliably used in further research. Without such validation, the optimisation procedure may unknowingly exploit modelling assumptions, potentially resulting in unphysical solutions and thereby reducing the practical applicability of the GeKO framework.

A suitable method for evaluating the influence of modelling assumptions and the characteristics of analysis tools is sensitivity analysis. In this approach, a specific property or assumption within the framework is varied while its effect on intermediate results and overall performance metrics is assessed. This procedure can help identify limitations of the modelling approach and provide insight into the robustness of the obtained results, while potentially revealing additional use cases for the tool.

Within the GeKO framework, key assumptions in the optimisation procedure have been identified and analysed through sensitivity studies. First, the assumption of a fixed sideslip angle during turning flight is investigated in Section 6.7.1. Following, the sensitivity of the optimisation results to environmental conditions is investigated in Section 6.7.2. In addition to this analysis, a partial functional validation and potential use case of the GeKO framework is explored.

6.7.1. Fixed sideslip angle β

As explained in Section 5.3.2, to find the turning radius for each kite geometry, the sideslip-induced side force is determined at a fixed angle of $\beta = 5°$. This angle was taken from previous research that found this sideslip angle for the reference TU Delft V3 kite in typical turning flight. In this sensitivity analysis, the fixed sideslip angle is changed to study its effects on the AEP. The effect of the sideslip angle on the optimised kite design and its corresponding AEP is given in Table 6.6 and Figure 6.27.

Table 6.6: Fixed sideslip angle sensitivity values to GeKO performance.

Sideslip angle	AR (-)	ab (-)	cd (-)	Γ (rad)	x_κ (-)	AEP (GWh)	AEP% from ref
3°	16.617	1.00	0.200	0.936136	1.198	112.901	-7.20%
4°	17.115	1.00	0.200	0.899	1.198	118.060	-2.96%
5°	17.630	1.00	0.200	0.877	1.198	121.664	*ref*
6°	18.332	1.00	0.200	0.874	1.200	124.238	+2.12%
7°	18.648	1.00	0.200	0.852	1.198	126.268	+3.78%
8°	18.776	1.00	0.200	0.840	1.198	127.870	+5.10%

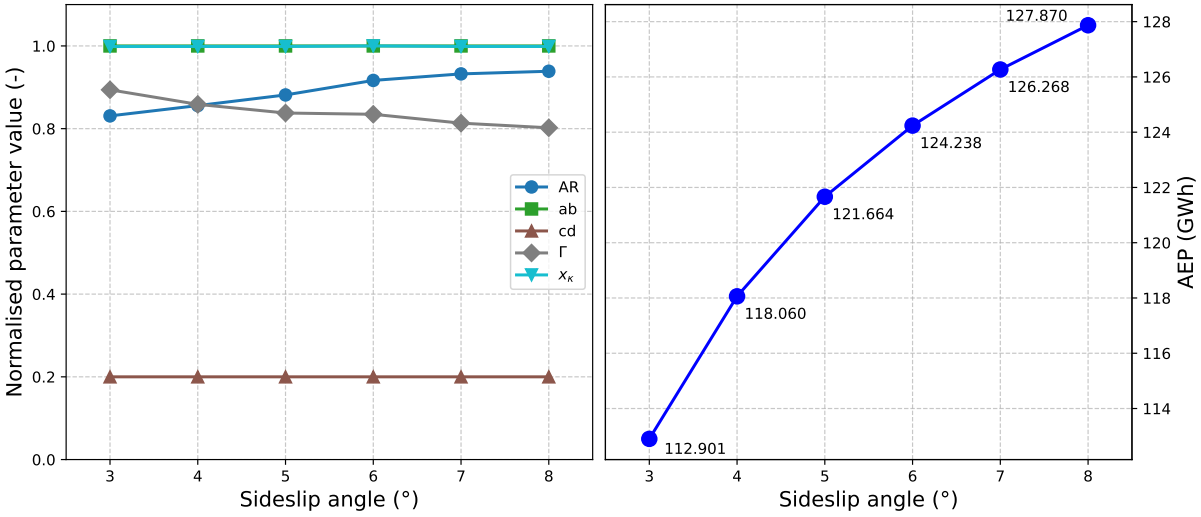

Figure 6.27: Fixed sideslip angle sensitivity trends to GeKO performance; design vector (left) and AEP (right). Normalisation was done using parameter bounds in Table 6.3.

As Figure 6.27 indicates, the prescribed sideslip angle significantly influences the optimal kite geometry and the resulting aerodynamic performance. Increasing the fixed sideslip angle yields performance improvements of several per cent. These gains are accompanied by systematic changes in the geometric parameters of the optimised configuration. In particular, the optimiser favours a higher AR and a lower arc-shape parameter Γ. Consequently, the resulting designs become more slender, wider, and flatter as the imposed sideslip angle increases. The trend

toward improved performance at higher sideslip angles during turning flight is illustrated in Figure 6.27.

This result is consistent with the expected behaviour. An increased sideslip angle leads to a higher side force during turning flight. The resulting increase in lateral force reduces the turning radius, lowering both the elevation and azimuth angles of the flight path. A reduction in these angles allows the kite to operate closer to the centre of the wind window, thereby increasing its pulling capability.

However, this observed trend should not be interpreted as a physically achievable operating condition without further consideration. In practice, the sideslip angle is not an independent control variable but rather an emergent flight state resulting from steering inputs and the coupled aeroelastic response of the kite. In the implemented model, this steering input is not explicitly included, and the sideslip angle is imposed directly. As a result, it remains uncertain whether the larger sideslip angles identified by the optimiser correspond to physically attainable flight conditions.

Furthermore, increased sideslip angles may introduce structural and aeroelastic challenges for soft-kite systems. In particular, large sideslip angles during turning manoeuvres could promote partial canopy collapse on the inner side of the turn. Such behaviour is not represented in the current modelling framework, as the aerodynamic analysis using the VSM assumes a rigid wing structure (see Section 3.4.2). Additionally, the method used to estimate the turning radius does not capture the structural deformations inherent to the operation of flexible kites.

For these reasons, a more detailed investigation of the turning dynamics, including aeroelastic deformation and steering-induced flight states, is required to properly assess the physical implications of prescribing a fixed sideslip angle in the optimisation framework.

6.7.2. Environmental conditions

The functionality of the developed toolchain was assessed by optimising the kite geometry under varying wind conditions and subsequently comparing the performance of the resulting designs under identical operating conditions. To generate different wind environments in a controlled manner, the hourly wind speeds of the statistical wind model were multiplied by a constant scaling factor c_w. This approach preserves the temporal characteristics of the wind profile while uniformly shifting the overall wind speed level. The scaled wind speed used during optimisation is defined as

$$v_{w_{new}} = c_w \, v_w, \tag{6.1}$$

where v_w denotes the original wind speed from the statistical wind model, c_w is the wind speed scaling factor, and $v_{w_{new}}$ is the resulting scaled wind speed used in the optimisation. Separate optimisations were performed for scaling factors ranging from $c_w = 0.5$ to $c_w = 1.5$, resulting in unique kite geometries. The design vectors of the resulting geometries are given in Table 6.7. The optimisation results show only minor variations in the AR and Γ. This shows that the optimal kite design depends on wind speed, though the sensitivity remains limited. The corresponding AEP obtained for the different optimised kites are presented in Table 6.8.

Table 6.7: Design vector for different wind speed scaling factors.

$c_{w_{design}}$ (-)	AR (-)	ab (-)	cd (-)	Γ (rad)	x_κ (-)
0.5	18.652347	1.0	0.2	0.874149	1.200000
0.75	18.294117	1.0	0.2	0.868805	1.198438
1.0	17.630055	1.0	0.2	0.877355	1.198438
1.25	17.497242	1.0	0.2	0.882699	1.198438
1.5	17.430836	1.0	0.2	0.885905	1.198438

After these geometries were identified, performance with the identical wind speed scaling factor ($c_w = 1.0$) was assessed. This allows direct comparison of the designs and provides a consistency check of the optimisation procedure, as the geometry optimised for a specific wind regime is expected to perform best under those same conditions. The corresponding results are shown in Figure 6.28, where the AEP of the five optimised kites under identical wind conditions is presented. As expected, the kite optimised for $c_w = 1.0$ achieves the highest AEP, confirming that the optimisation process captures the influence of the wind environment correctly. The difference between the AEP obtained under the design conditions and the common evaluation conditions is summarised in Table 6.8. The results show that, within the simplified modelling framework, environment-specific optimisation leads to only limited improvements in performance.

A notable observation is that the kite optimised for $c_{w,\text{design}} = 1.5$ produces a lower $\text{AEP}_{c_w=c_{w,\text{design}}}$ than the kite optimised for $c_{w,\text{design}} = 1.0$. At first glance, this appears counter-intuitive, since higher wind speeds generally result in higher cycle power outputs. However, this effect can be explained by operational constraints imposed by the flight scheduling algorithm. When wind speeds exceed the system's maximum allowable limit, flights are cancelled or aborted. Consequently, the annual flight time decreases with increasing wind speed, thereby reducing the total AEP. As a result, operating in slightly lower wind regimes may yield higher AEP for the AWES.

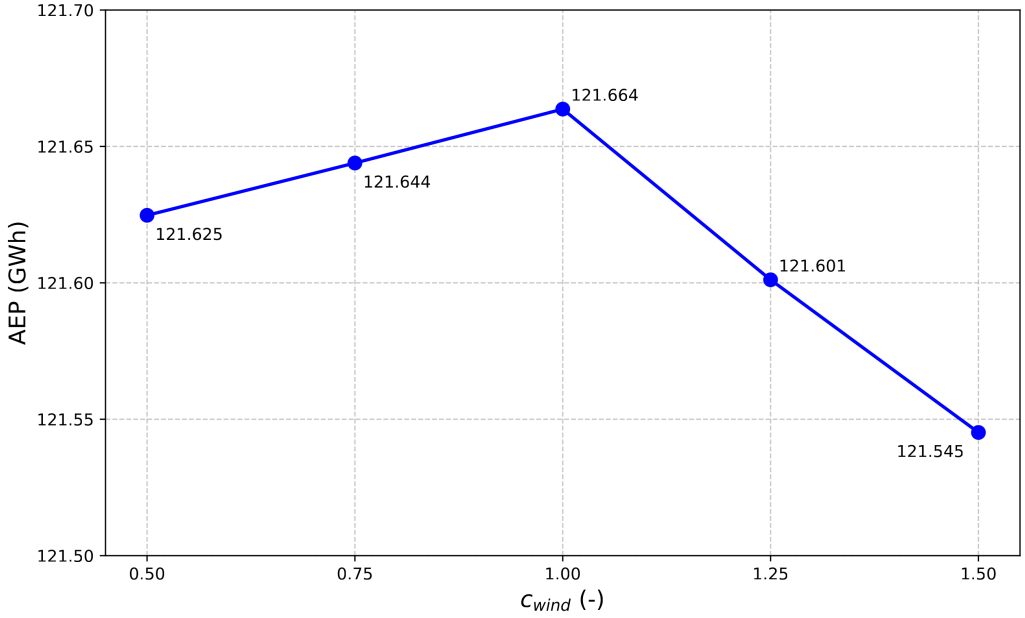

Figure 6.28: AEP comparison between kites optimised for different wind speeds.

Table 6.8: AEP for optimised kite geometries simulated at the design and 1.0 wind scaling factor.

$c_{w_{design}}$ (-)	$\text{AEP}_{c_w=c_{w_{design}}}$ (GWh)	$\text{AEP}_{v_w=v_{w_{1.0}}}$ (GWh)	% from ref
0.5	20.853	121.625	-0.032 %
0.75	76.645	121.644	-0.016 %
1.0	121.664	121.664	*ref*
1.25	124.105	121.601	-0.052 %
1.5	107.468	121.545	-0.098 %

7

Conclusion

The aim of this research was to develop and assess a MDAO framework for the geometric optimisation of a kite wing for AWE applications. For this, Research question 1-4 will be addressed, each specifying the kite-wing parametrisation, the selection of the simulation tools, the framework architecture, and the sensitivity analyses, respectively.

Simulation limitations require the kite wing to be parametrised with the fewest parameters possible. The design vector was chosen to be based on five parameters: the AR, three arc-shape parameters (ab, cd, Γ), and a camber-height scaling parameter x_κ. All other geometrical properties of the kite wing will be copied from the initial reference geometry, given as input to the simulation. These five parameters have demonstrated a high degree of geometrical design flexibility for LEI kites.

The current design strategy employed by Kitepower B.V. is partially based on simulation tools and partially based on expert-driven choices. Expert experience was included in the parameterisation selection, and a simulation tool selection was made based on current modelling approaches. A computationally inexpensive, high-fidelity regression was implemented to perform a 2-dimensional aerodynamic analysis of airfoil geometries. 3-dimensional aerodynamic analysis is performed using a VSM coupled with a particle-based structural model. Performance modelling is done in two steps: a QSM, which optimises the flight path and controls, and an FDS that accurately calculates the system's power curve. A flight-scheduling algorithm determines the AEP for specific environmental and operational conditions.

Three different gradient-free optimisation algorithms are proposed: Hooke and Jeeves pattern search, CMA-ES, and PSO. The Hooke and Jeeves algorithm was implemented in an initial framework implementation. The complexity of this framework was reduced for explorative purposes by replacing the QSM and FDS with the Luchsinger model. In this simplified framework, function evaluations took 30 seconds, and a geometrical kite optimisation takes around 1,5 hours. Comparing this to current design methods, including simulations, production, and experimental testing (which usually take multiple weeks), significant time gains were observed. However, this time gain is for a simplified framework, and computational times of the high-fidelity conceptual framework should be assessed.

The reference kite geometry (TU Delft V3 kite) was optimised to perform 94% better in AEP, with significant geometrical adaptations. Again, however, these performance gains are assessed using a simplified framework that relies heavily on assumptions. Therefore, this result should not be interpreted quantitatively. Rather, it shows potential for future implementation.

The framework can be used to validate assumptions in models, such as the fixed sideslip angle used in operational analyses for the Luchsinger model. The results show that altering this sideslip angle yields small changes in the resulting optimal geometries, most notably in the AR and Γ. These geometric differences translate into variations in the predicted AEP of several per cent between the optimised designs. Such differences are significant in the context of system optimisation and indicate that the assumed sideslip angle has a non-negligible influence on the optimisation outcome.

In a similar fashion, altering environmental conditions produced marginal geometric differences, most notably in the AR. With this change in geometry, a performance difference of <0.01% was found under identical environmental conditions. The simplified framework shows an expected trend in environmental conditions dependence, but the results show almost negligible performance gains.

In conclusion, the proposed framework captures the geometrical design of a kite with only five parameters and enables geometric optimisation in a fraction of the time required by current methods. A conceptual, higher-fidelity framework can be analysed to better understand the design problem, but its use is expected to be best suited to early design phases due to computational limitations. Compared with existing expert-driven and experimental design methods, MDAO provides a potentially faster, therefore also cost-effective, and systematic alternative for the geometrical design process of LEI kites for AWE applications.

8

Recommendations

The implemented framework showed potential to improve current geometrical kite design methods. However, the implemented models and framework include several assumptions and simplifications which could affect the results. From this, recommendations for future continuation of this work stream are derived and organised into five general concepts.

8.1. Extension of the geometric parametrisation

The current parametrisation enables controlled reshaping of the kite geometry while maintaining a constant reference area. However, in his thesis, Trevisi [52] found that, instead of fixing the area, fixing the span results in a different optimised design, potentially increasing the cycle power. For holistic optimisation of an AWES, the design vector should be reconsidered.

On top of this, the current parametrisation cannot modify spanwise-dependent geometry. These effects include spanwise distributions of chord length, camber height, wing twist, taper and sweep. Including these properties in the optimisation design vector provides greater flexibility in reshaping and could potentially improve the AEP.

8.2. Validation of operational constraints

The implemented framework assumes a fixed depower line length percentage during reel-out and reel-in. However, this approach does not guarantee that the resulting powered and depowered configurations correspond to the optimal operating states for each design. More in-depth research on this assumption is therefore recommended.

Similarly, the turning radius is determined under the assumption of a fixed sideslip angle. The sideslip angle was found to significantly influence results. Therefore, the method of determining the turning radius should be reconsidered.

8.3. Structural design integration

The conceptual framework includes an aero-structural modelling tool, but large geometric changes may require a more radical structural redesign. For example, the required number, placement, and configuration of bridle lines and wing struts may change to ensure structural integrity and controllability. Each kite geometry can then be optimised not only aerodynamically but also structurally, increasing potential performance gains.

8.4. Useful extension of the framework

The framework should accurately model environmental conditions to reflect real-world conditions. Current implementations assume a constant wind shear profile, which only partially reflects the physical reality. Incorporating higher-fidelity atmospheric modelling that accounts for turbulence and gusts may improve the operational accuracy. As required input to the QSM and FDS, the conceptual framework will not function without efforts in environmental modelling.

The current objective of the framework focuses on the AEP, a comparative method for system-level performance. A more holistic objective of an AWES is the environmental impact, which is not directly included in the AEP. Including a life-cycle assessment into the toolchain could enable assessment based on environmental impact.

In addition, any commercial system requires a full business case analysis to assess economic viability. As system resizing can impact costs, the feasibility from a business perspective may be affected. Including a cost analysis in the toolchain and penalising expensive systems could therefore enable a more thorough and diverse assessment.

8.5. Experimental validation

Although the implemented framework demonstrates promising optimisation behaviour, the reliability of the results should be assessed. Validation can be executed on two levels. First, the individual disciplines within the framework should be validated for the required design space flexibility. Second, system-level validation of the optimisation scheme should be conducted. Both validation steps can be performed by comparing the results to validated and experimental results. Once all disciplines have been validated, the optimised kite geometry should be produced and experimentally tested. These validations would increase confidence in both the simulation tools and the optimisation methodology.

References

[1] Airborne Wind Europe. *AWE systems*. 2024. URL: https://airbornewindeurope.org/awe-systems (visited on 02/11/2026).

[2] John D. Anderson. *Fundamentals of Aerodynamics*. 5th. McGraw-Hill Education, 2011.

[3] *Ansys*. en. Engineering Simulation Software. ANSYS, Inc. URL: https://www.ansys.com/ (visited on 02/06/2026).

[4] Cristina L. Archer and Ken Caldeira. "Global Assessment of High-Altitude Wind Power". In: *Energies 2009, Vol. 2, Pages 307-319* 2 (2 May 2009), pp. 307–319. ISSN: 1996-1073. DOI: 10.3390/EN20200307.

[5] Airborne Wind Energy Industry Association. *AWEIA Hall of Fame*. 2024. URL: https://aweia.org/hall-of-fame (visited on 02/11/2026).

[6] Philip Bechtle et al. "Airborne wind energy resource analysis". In: *Renewable Energy* 141 (Oct. 2019), pp. 1103–1116. ISSN: 0960-1481. DOI: 10.1016/J.RENENE.2019.03.118.

[7] Nicolas P. Bons et al. "Multimodality in Aerodynamic Wing Design Optimization". In: *AIAA Journal* 57 (3 Jan. 2019), pp. 1004–1018. ISSN: 00011452. DOI: 10.2514/1.J057294.

[8] Jeroen Breukels. "An Engineering Methodology for Kite Design". PhD thesis. Delft University of Technology, Jan. 2011. ISBN: 9789088912306.

[9] Kinga Budziak. *Aerodynamic Analysis with Athena Vortex Lattice (AVL)*. Sept. 2015. URL: http://nbn-resolving.org/urn:nbn:de:gbv:18302-aero2015-09-20.015.

[10] Oriol Cayon, Vince van Deursen, and Roland Schmehl. "Translational Dynamics of Bridled Kites: A Reduced-Order Model in the Course Reference Frame". In: *Wind Energy Science Discussions* (2025). Preprint. DOI: https://doi.org/10.5194/wes-2025-205.

[11] Oriol Cayon, Mac Gaunaa, and Roland Schmehl. "Fast Aero-Structural Model of a Leading-Edge Inflatable Kite". In: *Energies 2023, Vol. 16, Page 3061* 16 (7 Mar. 2023), p. 3061. ISSN: 1996-1073. DOI: 10.3390/EN16073061.

[12] Oriol Cayon, Simon Watson, and Roland Schmehl. "Kite as a sensor: wind and state estimation in tethered flying systems". In: *Wind Energy Science* 10 (10 Oct. 2025), pp. 2161–2188. ISSN: 23667451. DOI: 10.5194/WES-10-2161-2025.

[13] Moritz Diehl. "Airborne Wind Energy: Basic Concepts and Physical Foundations". In: *Green Energy and Technology* (2013), pp. 3–22. ISSN: 1865-3537. DOI: 10.1007/978-3-642-39965-7_1.

[14] Mark Drela. "XFOIL: An Analysis and Design System for Low Reynolds Number Airfoils". In: *Mueller, T.J. (eds) Low Reynolds Number Aerodynamics. Lecture Notes in Engineering* 54 (Berlin, Germany, Springer-Verlag, 1989 1989). DOI: 10.1007/978-3-642-84010-4_1.

[15] Mark Drela and H. Youngren. *MIT AVL User Primer*. Version 3.36. URL: https://web.mit.edu/drela/Public/web/avl/AVL_User_Primer.pdf (visited on 02/11/2026).

[16] Ember. *Electricity Data Explorer*. 2024. URL: https://ember-energy.org/data/electricity-data-explorer/ (visited on 02/11/2026).

[17] Uwe Fechner. "A Methodology for the Design of Kite-Power Control System". PhD thesis. Delft Technical University, 2016. DOI: 10.4233/uuid:85efaf4c-9dce-4111-bc91-7171b9da4b77.

[18] Evan Gaertner et al. *Definition of the IEA Wind 15-Megawatt Offshore Reference Wind Turbine. Technical Report*. National Renewable Energy Laboratory (NREL), 2020. URL: https://www.nrel.gov/docs/fy20osti/75698.pdf (visited on 02/11/2026).

[19] Mac Gaunaa et al. "Scaling Airborne Wind Energy Systems for Deployment on Mars". In: Springer, Cham, 2024, pp. 111–144. ISBN: 978-3-031-50081-7. DOI: 10.1007/978-3-031-50081-7_6.

[20] TUDelft AWE Research Group. *awesIO: Input/Output standard for airborne wind energy systems*. 2024. URL: https://github.com/awegroup/awesIO (visited on 02/11/2026).

[21] Pim J. Haanen. "In-flight experimental measurements of large-scale deformations on a leading-edge inflatable kite". MA thesis. Delft University of Technology, 2026. URL: https://repository.tudelft.nl/record/uuid:40f2626a-a436-4068-8269-3c663fc249fd.

[22] Luuk van Hagen et al. "Life-Cycle Assessment of a Multi-Megawatt Airborne Wind Energy System". In: *Energies 2023, Vol. 16, Page 1750* 16 (4 Feb. 2023), p. 1750. ISSN: 1996-1073. DOI: 10.3390/EN16041750.

[23] N. Hansen and A. Ostermeier. "Completely Derandomized Self-Adaptation in Evolution Strategies". In: *Evolutionary Computation* 9 (2 June 2001), pp. 159–195. ISSN: 1063-6560. DOI: 10.1162/106365601750190398.

[24] Maurice Hoogreef. "Advise, Formalize and Integrate MDO Architectures". PhD thesis. Delft University of Technology, 2017. ISBN: 9789402806823. DOI: 10.4233/UUID:CC2AF611-6D78-4439-9B10-7E62AE579029.

[25] Robert Hooke and T. A. Jeeves. ""Direct Search" Solution of Numerical and Statistical Problems". In: *Journal of the ACM (JACM)* 8 (2 Apr. 1961), pp. 212–229. ISSN: 1557735X. DOI: 10.1145/321062.321069.

[26] Rishikesh Joshi. "System Design and Scaling Trends in Airborne Wind Energy". PhD thesis. Delft University of Technology, 2025. DOI: 10.4233/UUID:4332D7C1-16DA-40CF-8BBE-201BAB967581.

[27] Robin H.M. Van Kappel. "Aerodynamic Analysis Tool for Dynamic Leading Edge Inflated Kite Models". MA thesis. Delft University of Technology, 2012. URL: https://repository.tudelft.nl/record/uuid:385d316b-c997-4a02-b0f3-b30c40fffc32.

[28] Th. Von Karman and W. R. Sears. "Airfoil Theory for Non-Uniform Motion". In: *Journal of the Aeronautical Sciences* 5 (10 Aug. 2012), pp. 379–390. DOI: 10.2514/8.674.

[29] J. Kennedy and R. Eberhart. "Particle swarm optimization". In: *Proceedings of ICNN'95 - International Conference on Neural Networks* 4 (1995), pp. 1942–1948. DOI: 10.1109/ICNN.1995.488968.

[30] Jun Xue Leng et al. "Multidisciplinary Design Optimization Processes for Efficiency Improvement of Aircraft: State-of-the-Art Review". In: *International Journal of Aeronautical and Space Sciences* 26 (4 July 2025), pp. 2020–2042. ISSN: 20932480. DOI: 10.1007/S42405-024-00811-8/FIGURES/15.

[31] Miles L. Loyd. "Crosswind kite power (for large-scale wind power production)". In: *Journal of Energy* 4 (3 May 2012), pp. 106–111. ISSN: 01460412. DOI: 10.2514/3.48021.

[32] Rolf H. Luchsinger. "Pumping Cycle Kite Power". In: *Green Energy and Technology* (2013), pp. 47–64. ISSN: 1865-3537. DOI: 10.1007/978-3-642-39965-7_3.

[33] Joaquim R.R.A. Martins and Andrew Ning. *Engineering Design Optimization*. Cambridge University Press, Nov. 2021. ISBN: 9781108980647. DOI: 10.1017/9781108980647.

[34] Kasper Masure. "Regression Model of Leading Edge Inflatable Kite Profile Aerodynamics". MA thesis. Delft University of Technology, 2025. URL: https://repository.tudelft.nl/record/uuid:865d59fc-ccff-462e-9bac-e81725f1c0c9.

[35] Lester James V. Miranda. "PySwarms: a research toolkit for Particle Swarm Optimization in Python". In: *Journal of Open Source Software* 3 (21 Jan. 2018), p. 433. ISSN: 2475-9066. DOI: 10.21105/JOSS.00433.

[36] Leland M. Nicolai and Grant E. Carichner. *Fundamentals of Aircraft and Airship Design*. American Institute of Aeronautics and Astronautics, Inc., Jan. 2010. DOI: 10.2514/4.867538.

[37] Wubbo J. Ockels. "Laddermill, a novel concept to exploit the energy in the airspace". In: *Aircraft Design* 4 (2-3 June 2001), pp. 81–97. ISSN: 13698869. DOI: 10.1016/S1369-8869(01)00002-7.

[38] Johannes Oehler and Roland Schmehl. "Aerodynamic characterization of a soft kite by in situ flow measurement". In: *Wind Energy Science* 4 (1 Jan. 2019), pp. 1–21. ISSN: 23667451. DOI: 10.5194/WES-4-1-2019.

[39] OpenFOAM Foundation. *OpenFOAM: The Open Source CFD Toolbox*. 2024. URL: https://www.openfoam.com/ (visited on 02/11/2026).

[40] Jelle A.W. Poland. *SurfplanAdapter*. 2024. URL: https://github.com/jellepoland/SurfplanAdapter (visited on 02/11/2026).

[41] Jelle A.W. Poland and Roland Schmehl. "A virtual wind tunnel for deforming airborne wind energy kites". In: *Journal of Physics: Conference Series* 2767 (7 June 2024), p. 072001. ISSN: 1742-6596. DOI: 10.1088/1742-6596/2767/7/072001.

[42] Jelle A.W. Poland and Roland Schmehl. "Modelling Aero-Structural Deformation of Flexible Membrane Kites". In: *Energies 2023, Vol. 16, Page 5264* 16 (14 July 2023), p. 5264. ISSN: 1996-1073. DOI: 10.3390/EN16145264.

[43] Gianfranco La Rocca. *Challenge the Future: MDO for Aerospace Applications | AE4205*. Personal course material / lecture notes (attended by the author). 2022.

[44] Mark Schelbergen et al. "Clustering wind profile shapes to estimate airborne wind energy production". In: *Wind Energy Science* 5 (3 Aug. 2020), pp. 1097–1120. ISSN: 23667451. DOI: 10.5194/WES-5-1097-2020.

[45] Roland Schmehl, Michael Noom, and Rolf van der Vlugt. "Traction Power Generation with Tethered Wings". In: *Green Energy and Technology*. Springer, Berlin, Heidelberg, 2013, pp. 23–45. ISBN: 978-3-642-39965-7. DOI: 10.1007/978-3-642-39965-7_2.

[46] Roland H. Schmehl. *Airborne Wind Energy 2025/2026*. 2025. URL: https://awecourse.github.io/slides/ (visited on 02/11/2026).

[47] Jochem De Schutter et al. "AWEbox: An Optimal Control Framework for Single- and Multi-Aircraft Airborne Wind Energy Systems". In: *Energies 2023, Vol. 16, Page 1900* 16 (4 Feb. 2023), p. 1900. ISSN: 1996-1073. DOI: 10.3390/EN16041900.

[48] Peter Sharpe. *NeuralFoil: An airfoil aerodynamics analysis tool using physics-informed machine learning*. 2023. URL: https://github.com/peterdsharpe/NeuralFoil.

[49] Peter D. Sharpe. "Accelerating Practical Engineering Design Optimization with Computational Graph Transformations". PhD thesis. Massachusetts Institute of Technology, 2024. URL: https://dspace.mit.edu/handle/1721.1/157809.

[50] Jaroslaw Sobieszczanski-Sobieski et al. *Multidisciplinary Design Optimization Supported by Knowledge Based Engineering*. Wiley, Dec. 2015, pp. 1–378. ISBN: 9781118897072. DOI: 10.1002/9781118897072.

[51] *SurfPlan*. Accessed: 2026-02-11. URL: http://www.surfplan.com.au/sp/default.aspx.

[52] Filippo Trevisi. "Configuration Optimisation of Kite-Based Wind Turbines". MA thesis. University of Padova, Oct. 2019, p. 142. DOI: 10.13140/RG.2.2.24256.28160.

[53] F. Corte Vargas et al. *Arcadian Renewable Energy System*. Tech. rep. Delft University of Technology, 2020. URL: https://repository.tudelft.nl/record/uuid:93c343e5-ee79-4320-98a3-949d3e9c407d.

[54] Rolf van der Vlugt et al. "Quasi-steady model of a pumping kite power system". In: *Renewable Energy* 131 (Feb. 2019), pp. 83–99. ISSN: 0960-1481. DOI: 10.1016/J.RENENE.2018.07.023.

[55] Henry G. Weller et al. "A Tensorial Approach to Computational Continuum Mechanics Using Object-Oriented Techniques". In: *Computational Fluid Dynamics 2004*. Springer, 2007, pp. 175–180. DOI: 10.1007/978-3-540-34486-6_25.

[56] Udo Zillmann and Philip Bechtle. "Emergence and Economic Dimension of Airborne Wind Energy". In: *Green Energy and Technology* 0 (9789811019463 2018), pp. 1–25. ISSN: 1865-3537. DOI: 10.1007/978-981-10-1947-0_1.

A

Kite Reshaping Work Flow

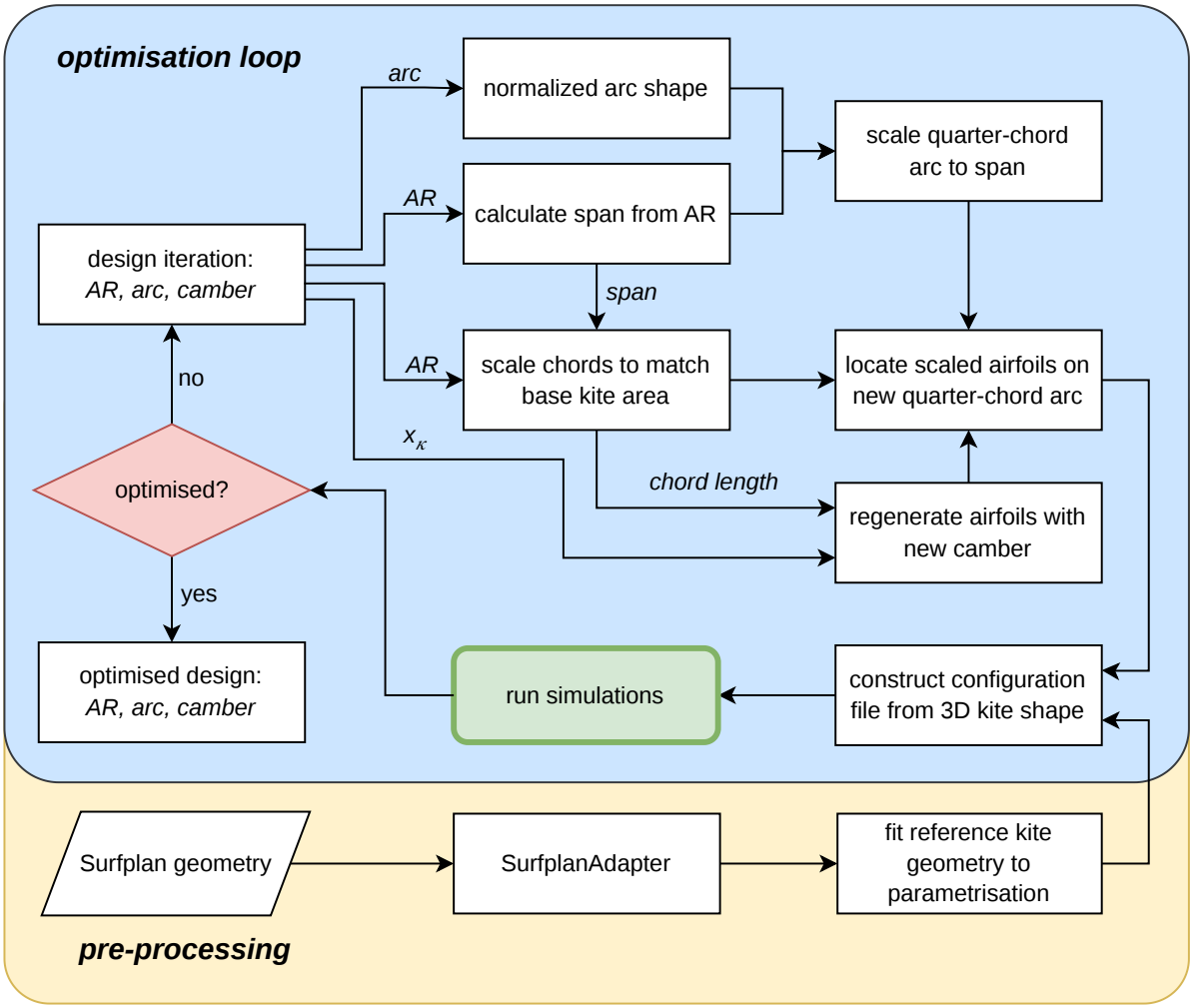

Figure A.1: Flowchart of kite parametrisation and scaling.

B

Conceptual Toolchain XDSM

The next page contains the XDSM of the conceptual toolchain, as explained in Section 5.1. This XDSM follows the principles explained in Section 2.4.2, which is recommended for review before studying the XDSM on the following page. The chosen system architecture for this XDSM is a hybrid between IDF and MDF, with consistency constraints included alongside the objective function (IDF) and execution-order dependence (MDF). Moreover, additional elements have been included in the framework, such as an aerodynamic sanity check, which reiterates designs based on aerodynamic sanity checks before computationally intensive disciplines are executed.

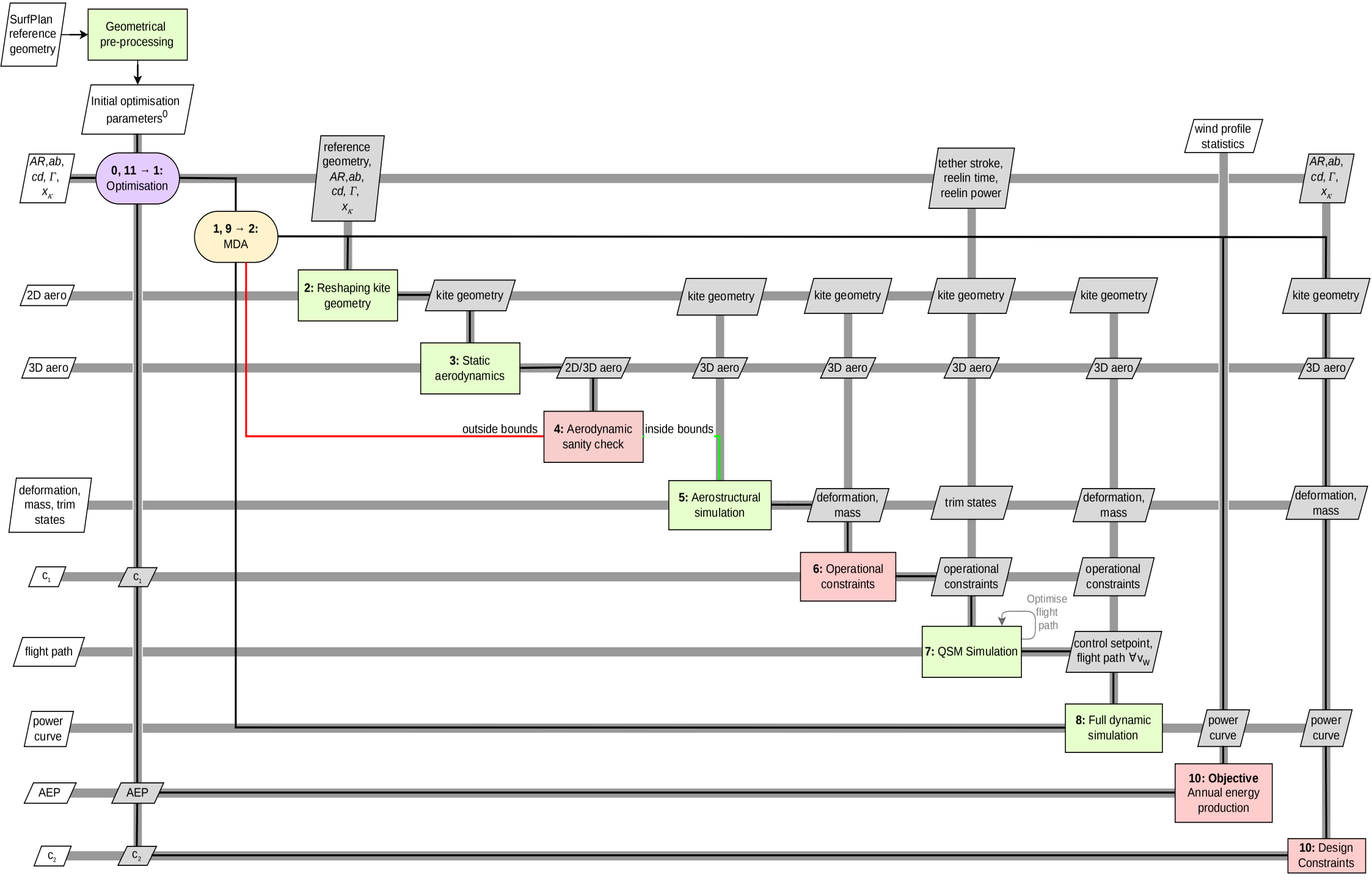
SurfPlan reference geometry
Geometrical pre-processing
Initial optimisation parameters^0
AR,ab, cd, Γ, x_{κ}
0, 11 → 1: Optimisation
1, 9 → 2: MDA
reference geometry, AR,ab, cd, Γ, x_{κ}
tether stroke, reelin time, reelin power
wind profile statistics
AR,ab, cd, Γ, x_{κ}
2D aero
2: Reshaping kite geometry
kite geometry
kite geometry
kite geometry
kite geometry
kite geometry
kite geometry
3D aero
3: Static aerodynamics
2D/3D aero
3D aero
3D aero
3D aero
3D aero
3D aero
outside bounds
4: Aerodynamic sanity check
inside bounds
deformation, mass, trim states
5: Aerostructural simulation
deformation, mass
trim states
deformation, mass
deformation, mass
c_1
c_1
6: Operational constraints
operational constraints
operational constraints
Optimise flight path
flight path
7: QSM Simulation
control setpoint, flight path $\forall v_w$
power curve
8: Full dynamic simulation
power curve
power curve
AEP
AEP
10: Objective Annual energy production
c_2
c_2
10: Design Constraints

C

Luchsinger Model Simulation Settings

The simulation settings required for the adapter Luchsinger model described in Section 3.4.3 are given in Table C.1.

Table C.1: Simulation input parameters for environment, tether, and operational variables.

	Setting variable	Value	Unit
env	atmospheric density	1.225	$\mathrm{kg\,m^{-3}}$
	wind speed min	1.0	$\mathrm{m\,s^{-1}}$
	wind speed max	20.0	$\mathrm{m\,s^{-1}}$
	wind speed delta	0.01	$\mathrm{m\,s^{-1}}$
tether	nominal tether force	25.000	N
	drag coefficient	1.1	–
	diameter	0.014	m
	maximum length	375.0	m
	minimum length	270.0	m
operational	nominal generator power	250.000	W
	elevation angle (out)	see Section 5.3.3	°
	azimuth angle (out)	see Section 5.3.3	°
	reeling speed min limit	-8.0	$\mathrm{m\,s^{-1}}$
	reeling speed max limit	8.0	$\mathrm{m\,s^{-1}}$

D

Optimisation Dashboard

The dashboard for the optimisation run performed as part of the experiment explained in Section 6.6 is given in Figure D.1. The AEP clearly improves during the simulation, and the design vector parameters converge to the optimal value.

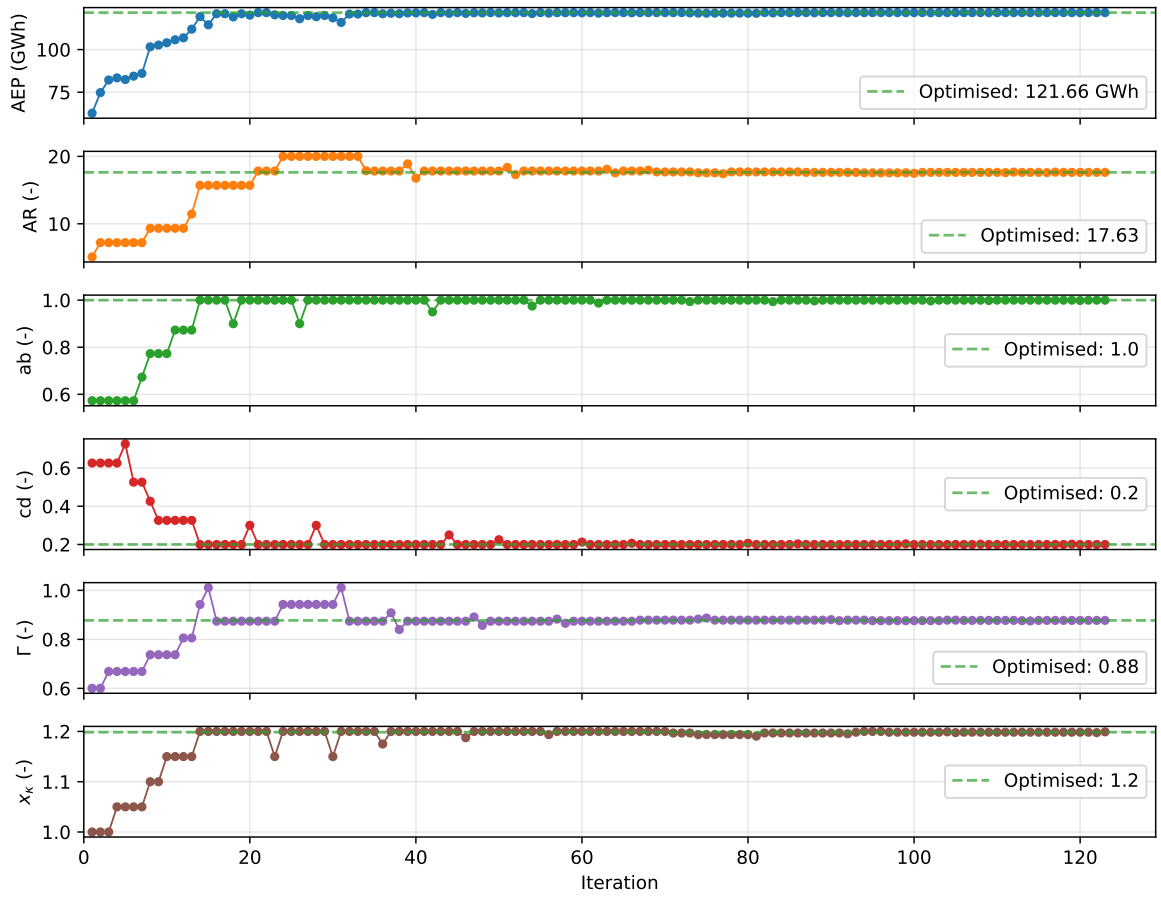

Figure D.1: Optimisation dashboard for TU Delft V3 kite.